論文 / 著書情報
Article / Book Information

題目(和文)	
Title(English)	Microscopic study of mixed cation lead halide perovskites films
著者(和文)	アガルワル アヌバ
Author(English)	AGARWAL ANUBHA
出典(和文)	学位:博士(工学), 学位授与機関:東京工業大学, 報告番号:甲第12399号, 授与年月日:2023年3月26日, 学位の種別:課程博士, 審査員:VACHA MARTIN,森 健彦,石川 謙,早水 裕平,相良 剛光
Citation(English)	Degree:Doctor (Engineering), Conferring organization: Tokyo Institute of Technology, Report number:甲第12399号, Conferred date:2023/3/26, Degree Type:Course doctor, Examiner:,,,,
学位種別(和文)	博士論文
Type(English)	Doctoral Thesis

Microscopic study of mixed cation lead halide perovskites films

Anubha Agarwal

School of Materials and Chemical Technology

Tokyo Institute of Technology

Contents

Chapter 1: General Introduction

Chapter 1

General Introduction

1.1 Photovoltaics of halide perovskites

A solar cell is an electronic device that directly converts sunlight into electricity. Light shining on the solar cell produces both a current and a voltage to generate electric power. This process requires firstly, a material in which the absorption of light raises an electron to a higher energy state, and secondly, the movement of this higher energy electron from the solar cell into an external circuit. The electron then dissipates its energy in the external circuit and returns to the solar cell. A variety of materials and processes can potentially satisfy the requirements for photovoltaic (PV) energy conversion, but in practice, most photovoltaic energy conversion uses semiconductor materials in the form of a p-n junction. As we can see the basic solar cell working structure below in Figure 1.1.

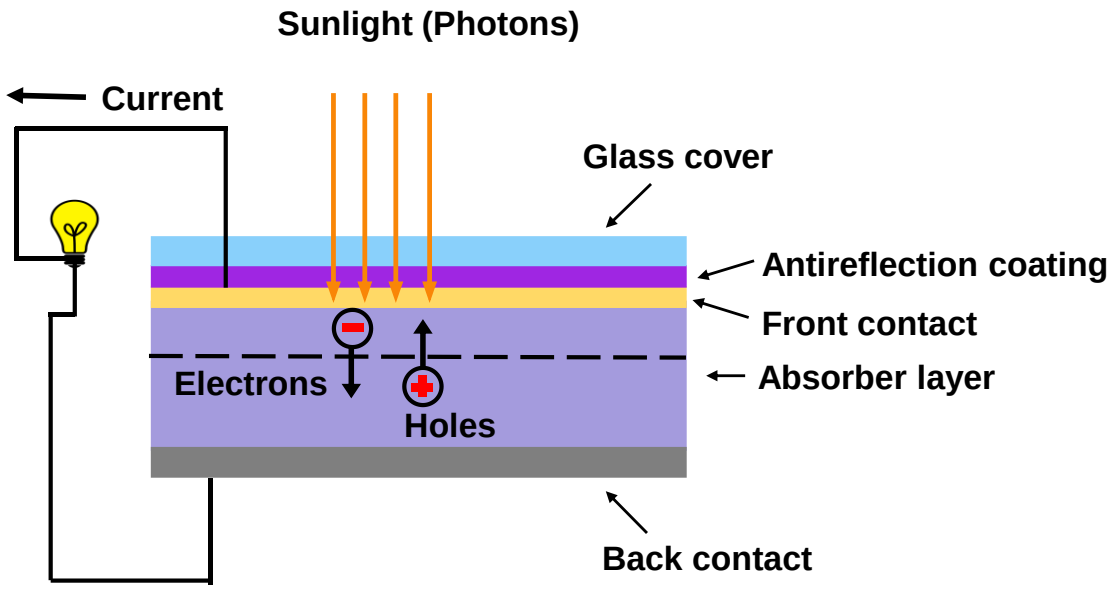

Figure 1.1. Solar cell working principle.

As an active PV absorbing material, organic–inorganic lead halide perovskites have shown the most notable progress in the field of solar energy conversion. Their advantages for solar cell applications include high dielectric constant, direct bandgap, high absorption coefficient, small exciton binding energy, and high diffusion length on the order of one micrometer. In the decade since 2009, the power conversion efficiency (PCE) of perovskite

solar cells (PSCs) has rapidly increased to reach the latest record of 25.7% (UNIST, EPFL claim 25.7% efficiency world record for perovskite solar cell).[1]

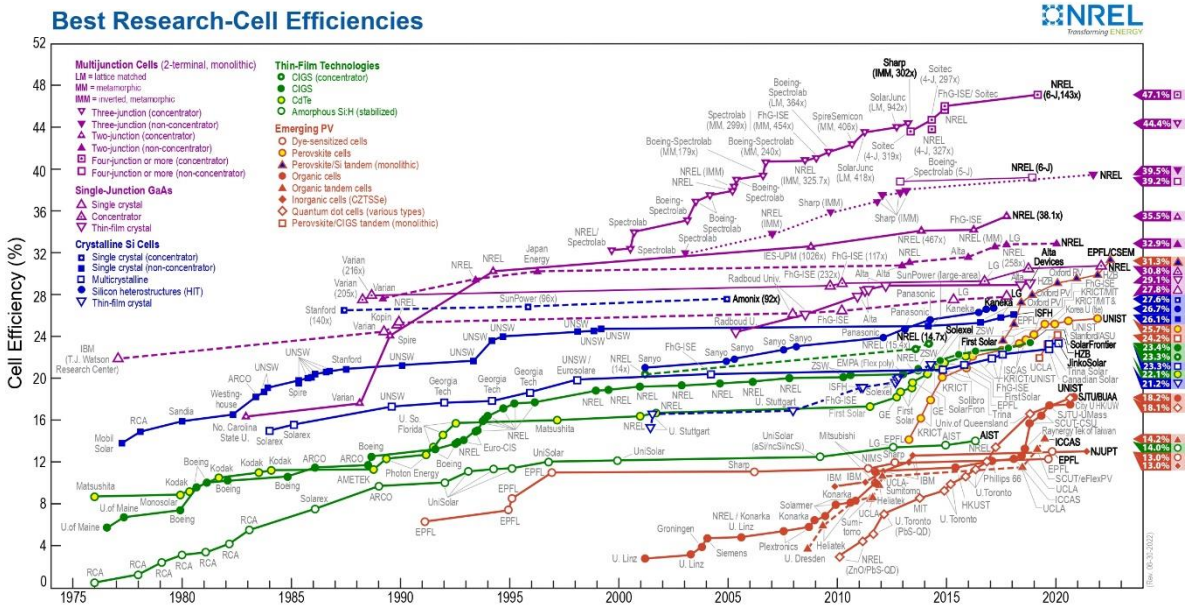

Figure 1.2. NREL chart of the highest confirmed conversion efficiencies for research cells for a range of photovoltaic technologies, plotted from 1976 to the present (reproduced with ref. 2 with permission).

Not only the high performance but also the cost-effective solution-based processes used for device fabrication shows the huge potential of PSCs as the PV technology of the future. While solution-based synthesis of perovskite materials involves a lot of chemistry, crystallization engineering, and the optical and electrical characterization of solid-state crystals (semiconductors) have their backgrounds in physics.

The versatile nature of perovskite photovoltaics requires the expertise in chemistry, physics, and optoelectronics; therefore, the research area has attracted a large community of researchers from all around the world. As a result, research progress in perovskite PV has been tremendous in the past couple of years (as we can also see in Figure 1.2).[2]

Interestingly, together with the discoveries of their rare properties, perovskites have found many applications beyond PV, expanding into the areas of light-emitting diodes, photodetectors, X-ray detectors, memory devices, and so on. Being a ‘magic box’ of many unconventional properties, perovskites have also triggered fundamental studies on ion

migration, defect tolerance, carrier dynamics, etc. However, while some of the properties of perovskite are very valuable, others are creating issues with their practical implication of the new technology. For example, while the defect-tolerant nature of perovskites contributes to high efficiency, the ion migration phenomenon stands as a potential threat to stability. Efficiency and stability are two important factors for device fabrication and industrialization. Although there are currently challenges in the commercialization of PSCs, results emerging from both research laboratories and industries show prominent potential. The tremendous success of perovskite PV was quite unexpected and now it is important to have a discussion on their performance, their stability, industrialization, present challenges, and future prospects.

1.2 History of perovskite photovoltaics

The term "perovskite solar cell" is very familiar these days, but it was unknown in 2005, when the research to explore PV applications of halide perovskites began in the Miyasaka laboratory at Toin University in Yokohama, Japan.[3] At that time, "perovskite" generally meant metal oxides having perovskite structures, most of them being classified as either ferroelectric or piezoelectric materials. Normally, perovskite represents a crystal structure with the chemical formula ABX_3, in which A and B are cations and X is an anion. In the typical cubic structure, the B cation has a 6-fold coordination, surrounded by an octahedron of anions, and the A cation has a 12-fold cuboctahedral coordination. The cubic unit cell of such compounds is composed of A cations at cube corner positions, B sitting at the body-center position, and X anion occupying the face-centered positions (see Figure 1.3).[4]

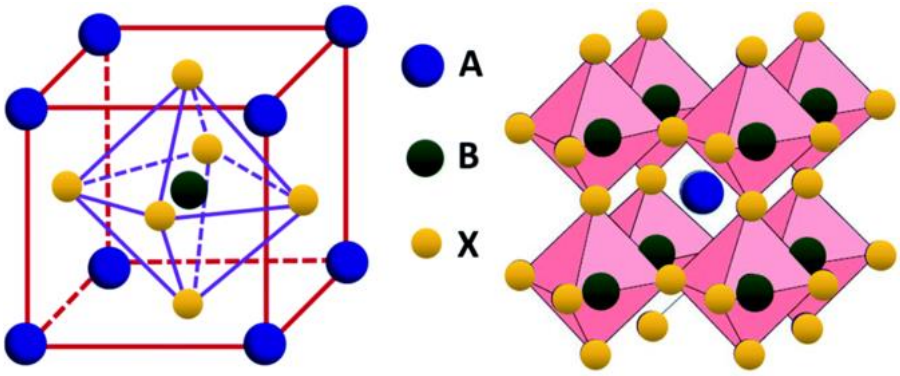

Figure 1.3. Structure of perovskites (reproduced with ref. 4 with permission).

In the history of minerals, perovskite was first discovered in a piece of chloriterich skarn by the Prussian mineralogist Gustav Rose in 1839.[5] The mineral was composed of $CaTiO_3$ and was named after Lev A. Perovskiy (1792−1856), the renowned Russian mineralogist, upon the request of a notable Russian mineral collector, August Alexander Kämmerer. Later on, many inorganic metal oxides, such as $BaTiO_3$, $PbTiO_3$, $SrTiO_3$, $BiFeO_3$, etc., were found which also have the perovskite structure, therefore, perovskite compounds are more commonly known as metal oxides, with formula ABO_3. These metal oxide perovskites do not have any good semiconducting properties that would make them suitable for PV applications or optoelectronics. However, a class of perovskites that differ from oxide perovskites known as halide perovskites with halide anions in place of oxygen anions shows semiconducting properties that are desired for PV applications.[6] The discovery of such halide perovskites was noted in the 1890s. In 1893, Wells et al. performed an impressive study on the synthesis of lead halide compounds from solutions including lead halide and cesium, $CsPbX_3$ (X = Cl, Br, I),[7] ammonium (NH_4),[8] or rubidium, $RbPbX_3$.[9] Later, in 1957, the Danish researcher C. K. Møller found that $CsPbCl_3$ and $CsPbBr_3$ have the perovskite structure,[10-11] existing as a tetragonally distorted structure which undergoes a transition to a pure cubic phase at high temperature.[11] The simple solution process for the synthesis of these cesium lead halide ionic crystals might have inspired researchers to use other cations in place of Cs. Weber[8,9] found that the organic cation methylammonium ($CH_3NH_3^+$) replaces Cs^+ to form $CH_3NH_3MX_3$ (M = Pb,[8] Sn,[9] X = I, Br) and reported the first crystallographic study on organic lead halide perovskites. In other words, we can say that this research was the birth of perovskite semiconductor materials. By the end of the 20th century, a large variety of halide perovskites were synthesized by David Mitzi using

small and large organic cations,[12–14] focusing on the physical properties of two-dimensional (2D) perovskite materials with a large organic group.[13] Based on this study, in the late 1990s, Prof. Kohei Sanui conducted a project of self-organized quantum confinement structures using the above perovskites; optical properties of 2D[15-16] and 3D crystals were investigated.[17-18] Although the research opened applications of these materials to nonlinear optics and electroluminescence (i.e., light-emitting diodes, LEDs) by utilizing sharp monochromatic optical absorption and luminescence,[19-20] there was no idea that these materials could be utilized for solar energy because 2D perovskites are not suitable for harvesting light over the wide spectral range of sunlight.

1.3 Discovery of halide perovskite solar cells

First and second-generation solar cells consisting of silicon wafer-based and thin-film solar cells, respectively, have done well in terms of efficiency and stability. For the use of solar cells, ultra-high purity metallic silicon (>99.9999%) can be obtained by the crystallization of melted Si in a furnace at more than 1400 °C. Thus, the high cost of materials and energy-demanding processing of wafers has slowed the widespread use of solar cells as alternatives to fossil-fuel-based energy sources such as thermal power generation.

Thus, a lot of research and development has been devoted to finding a cost-effective and highly efficient alternative, leading to third-generation photovoltaics, including organic solar cells and dye-sensitized solar cells (DSSCs). These cells could be processed very cheaply, but their performance remained limited to PCE of around 10%, which limited their chances for commercialization. In 2005−2006, researchers were putting their continuous efforts into the further development of DSSCs,[21–23]. They explored the use of an organic−inorganic lead halide perovskite as an absorber to replace the organic dye in DSSCs. Although nobody imagined that the material would open up a new world of PV with such immense potential, people were curious to exploit its semiconducting properties in photoelectrochemical cells. This proved an absolutely blissful encounter with the perovskites.

In addition, halide perovskites also possess materials properties of interest for optical sources: bright photoluminescence, narrow light emission line width, tunable exciton binding energy, and balanced charge carrier mobility.[24-26] In the early 1990s, researchers

applied layered structured halide perovskites (e.g., Ruddlesden−Popper phases) to create light-emitting diodes (LEDs) that operated at liquid nitrogen temperature.[27] In 2012, room-temperature halide perovskite LEDs were reported.[28] In 2015, the first efficient perovskite LEDs (EQE ~8.5%) were reported.[29] Studies of perovskite optical sources have similarly intensified in the past years.

1.4 Current state of halide perovskite for photovoltaics and optoelectronics application

In the early days of research into these materials, single-cation ('pure') perovskites such as $MAPbI_3$, $FAPbI_3$ and $CsPbI_3$ were widely studied for LED's and solar cell applications. Here, MA stands for methylammonium, FA for formamidinium. However, as some of their limitations became apparent, recently more effort went into developing mixed-ion hybrid perovskites (MIHPs), in which anions Br^- and Cl^- were mixed with I^-; the MA cations were substituted by FA, rubidium (Rb), and cesium (Cs); also, Pb was substituted by Sn,[30] in addition to a few other combinations. This is the beginning of a new era in the field of perovskite solar cells and optoelectronics devices. By mixing a systemic ratio of materials, researchers have attempted to boost the performance with high ambient stability. This allowed for the control of various properties such as the bandgap,[31] the phase stability at room temperature,[32] carrier transport,[33] device performance, and stability, etc.

MIHPs are ideal materials for applications in photovoltaics owing to their high compositional flexibility and optoelectronic properties. However, one major obstacle to industrial use is their compositional instability.[11] Some of the mixed-ion perovskites under illumination or charge-carrier injection process experience ion migration into regions with differing ion contents or non-radiative recombination processes due to grain boundary defects. Such a migration of ions or non-radiative recombination adversely affects the electronic properties of the material and severely limits the prospects of the MIHP technology.[18]

1.5 Microscopy studies on perovskites

Fluorescence microscopy[34-35] has served as a powerful tool to find internal structure−function information in perovskite nanocrystals, nanofibers, thin films, etc.,[34-36] and has provided insight into potential sources of many different optical and photophysical phenomena, e.g., band gap tuning, nonradiative recombination,[37-39] heterogeneity,[40-43] charge carrier transformation,[44-47] surface traps, ion migration, phase segregation, etc. These studies are also based on the combination of several spectroscopies techniques including photoluminescence (PL),[48-54] electron microscopy,[55] electroluminescence[56] or atomic force microscopy (AFM).[57]

Several groups have revealed the local photophysics of the perovskite materials and the heterogeneous distribution of trap states[34,58-59] in the films. Effective utilization of these fluorescence techniques can give access to local energy transport, and grain boundaries and further inform pathways to rationally control these fundamental processes to improve the efficiency of solar cells, light-emitting diodes[4,44,56-61] lasers, and transistors. However, whether carrier transport or recombination dominates the optoelectronic[62] heterogeneity is still unclear. For example, some groups reported that photoluminescence intensities and lifetimes varied between different grains in the same sample and showed that grain boundaries were generally dimmer and exhibited faster photoluminescence decays.[15-16,63] Other groups have reported similar local variations in photoluminescence intensity and have interpreted these results as variations in nonradiative recombination rates due to heterogeneous distributions of surface traps.[17,20,64] The origins of the photoluminescence heterogeneity in perovskites and the existence of structural and electronic barriers to lateral carrier diffusion in perovskite film are important topics that not only affect the performance of perovskites in solar cells and other device applications but also, in turn, affect the analysis of many other experiments and even the extraction of fundamental properties like conductivity and charge carrier density.

1.6 Methodology of fluorescence microscopy

1.6.1 Basics of fluorescence microscopy

Fluorescence microscopy[65-67] is a technique to detect photoluminescence (PL) from light-emitting entities such as organic molecules, aggerates, nanoparticles, and quantum dots, etc. A fluorescence microscope is an optical microscope that both excites and collects fluorescence signals from the sample. Different types of fluorescence microscopes have been developed. In a wide-field fluorescence microscope, a filter cube containing an excitation filter, emission filter, and dichroic mirror is placed in the light path ahead of the objective lens, as illustrated in Figure 1.4.

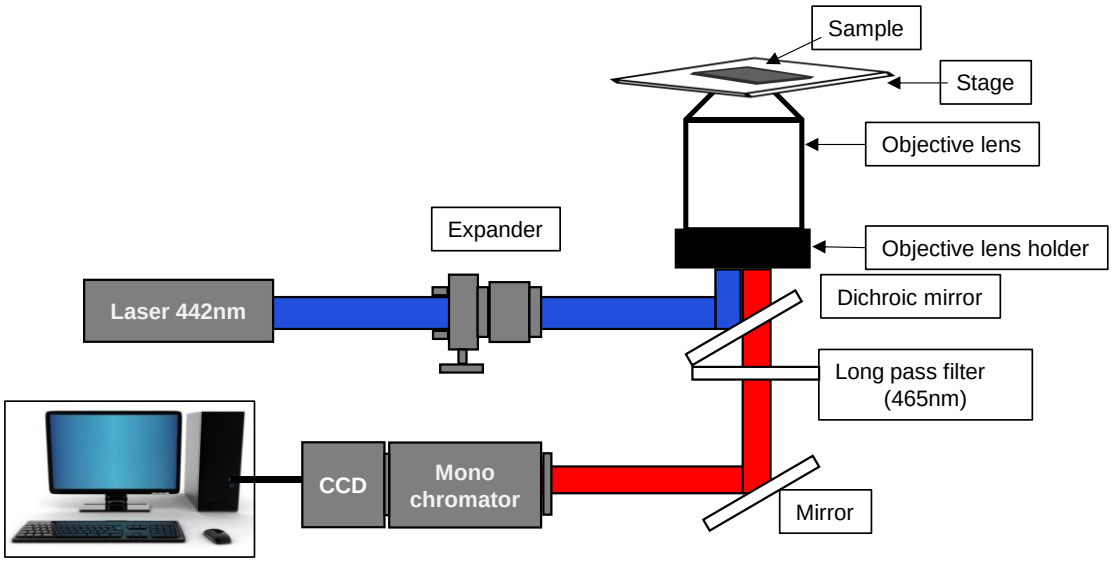

Figure 1.4. Schematic diagram of microscopy setup

In this, the excitation light is mostly provided by a laser, and the excitation wavelength is selected to be absorbed by the sample. An optional excitation filter selectively allows the desired wavelength from the light source to pass. Excitation light is reflected by a dichroic mirror and focused on the sample through an objective lens. Fluorescence from the sample is passing through the dichroic mirror and a long pass filter and is detected by a photodetector, such as CCD camera. Dichroic mirrors can reflect the excitation light (shorter

wavelength) and pass the emission (longer wavelength). A long pass filter is used for cutting the transmitted excitation light to decrease background scattering. It is well known that Rayleigh scattering intensity is proportional to excitation intensity and to the fourth power of wavelength. Shorter wavelength and higher intensity of excitation increase the background scattering and contribute to the difficulty of PL emission detection. Therefore, optical filters, excitation wavelength, and intensity should be selected and adjusted carefully. If we select the appropriate filters most of the excitation light reaching the sample will be transmitted and thus will not be collected by the objective lens. The background noise from the excitation light will be significantly reduced in this case.

Like all other optical microscopes, the spatial resolution of a fluorescence microscope is diffraction limited. The resolution at a certain excitation wavelength can be estimated by the Rayleigh criterion:

$$d \approx 0.61 \times \frac{\lambda}{NA}$$

where d is the diffraction limited resolution, λ is the wavelength of the light, and NA is the numerical aperture of the objective, which usually has a value of 1.4 to 1.6 for oil-immersion lenses.[66] According to the Rayleigh criterion, when measuring a sample emitting light at a wavelength of above 600 nm (e.g., $MAPbI_3$), the resolution of the fluorescence microscope will be around 280 nm.

The integration of a spectrometer in the optical path of the microscope to separate light of different wavelengths onto different pixels of the CCD camera enables not only the fluorescence intensity but also the emission spectrum of the samples can be recorded. The measurement of, e.g., emission spectra[68] during crystal transformations provides more compositional information than simply monitoring the intensity variation. A wide-field detector such as CCD camera can record the fluorescence intensity trajectories of hundreds of crystals simultaneously and thus facilitates the statistical analysis of heterogeneity.

1.6.2 Non-radiative recombination

One of the important parameters obtained from PL microscopic imaging is the spatial variations in non-radiative recombination. As opposed to radiative recombination processes, non-radiative recombination allows the annihilation of an exciton without the emission of photons. These processes are present in quantum dots, as well as in semiconductors in general, and are important to understand the dynamics of the system. The most important ones are:

- Auger recombination,
- exciton-phonon interaction,
- charge trapping.

We are briefly describing these effects below, starting with the most important one in the general case of semiconductors.

i) Auger recombination.

Auger recombination is a mechanism present in semiconductors analogous to the Auger effect in atoms. The Auger effect is the second ionization of an atom due to the energy transferred by an electron of the atom itself; the process is shown in Figure 1.5. The process happens in two steps:

- The atom is first ionized, i.e. by an ionizing radiation, and as a consequence of this ionization, a hole is present in one of its inner shells
- One electron relaxes from an outer level to the hole while another “collects” its energy and is emitted

In Auger recombination there is a similar effect: an exciton in a semiconductor recombines giving its energy to a carrier in the valence band. As opposed to the Auger ionization, the carrier that collects the charge stays in the conduction band at a higher-level state and no ionization happens. The carrier can then relax non-radiatively to the ground state of the conduction band. This mechanism is important in perovskites as well as it often guarantees photon emission. Indeed, if more than one exciton is created, the excitons in addition to the first one can recombine non-radiatively giving their energy to the first one. The Auger recombination is usually a very efficient mechanism: until the Auger recombination is possible, it is predominant on the radiative recombination.

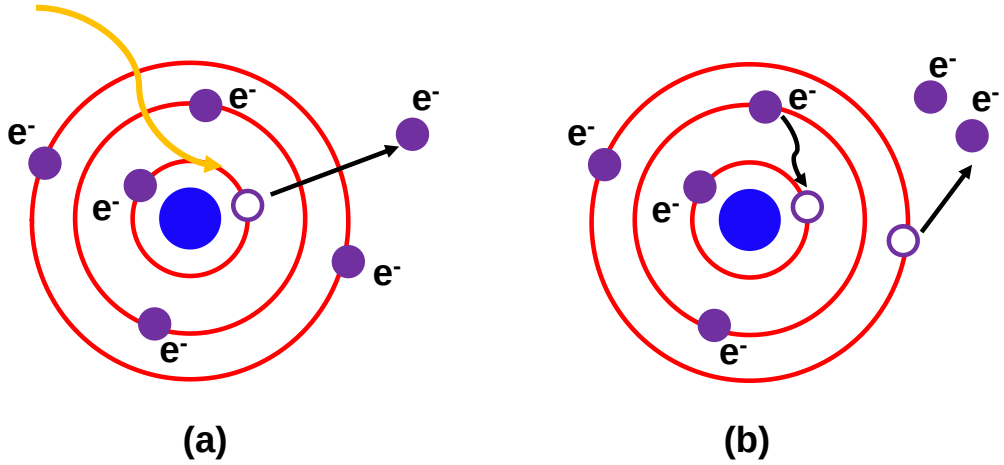

Figure 1.5. Mechanism of Auger ionization: (a) The atom is ionized by a radiation (i.e. a γ ray) and loses one of its electrons of the inner shell; (b) One outer electron relaxes to the hole left by the missing electron giving its energy to an outer electron and the atom is ionized for the second time.

When only one exciton is present, there are no more carriers in the conduction band to which the energy of the exciton can be passed on, and the Auger effect is not possible anymore; this time, the exciton relaxes radiatively with the emission of one photon. The scheme of Auger recombination is shown in Figure 1.6.

ii) Interaction of excitons with phonons

A phonon is a quasi-particle that represents the elementary vibrational excitation of a lattice. We can distinguish two different cases:

1) Intraband relaxation
2) Interband relaxation.

Intraband relaxation: the fact that electrons and holes can relax releasing energy in a semiconductor seems normal, although, with deeper thinking, it is quite surprising. Indeed, for both electrons and holes, phonon energy levels are also discrete. Therefore, except for the case of energy overlap, the transfer of energy from an exciton to a phonon should be prohibited. On the contrary, it was observed that the thermal relaxation is even accelerated by the quantum confinement.

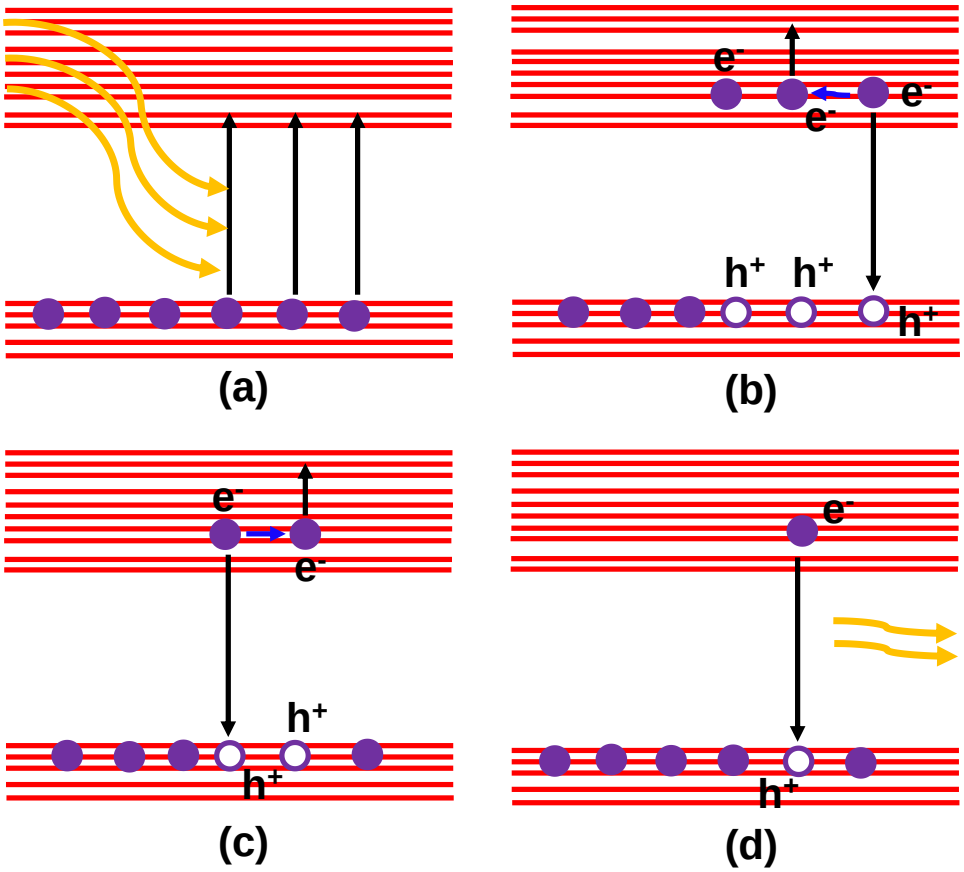

Figure 1.6. Mechanism for Auger recombination: (a) The semiconductor is excited by light and multiple excitons are created; (b) and (c) until multiple excitons are present, one exciton can relax non-radiatively passing the energy to another one; finally (c) the last exciton relaxes radiatively by emitting a single photon with the energy of the gap.

This is due to the fact that this process is mediated by the Auger energy transfer from electrons to holes. The process is usually very fast, on the order of hundreds of femtoseconds (compared to some nanoseconds for the radiative decay).

Interband relaxation: phonons have an effect also in interband relaxation, in two distinct ways. First, they affect the spectrum by broadening the emission peak and secondly, they create a non-radiative relaxation channel that is in competition with the radiative one.

iii) Charge trapping

A carrier can be trapped onto a defect of the lattice or at the surface of the nanocrystal. When this happens, it creates additional energy levels within the gap of the semiconductor providing a non-radiative decay path, and, as a consequence, no photon is emitted by the crystal. A trapped state can last from tens of picoseconds up to several seconds and its de-excitation is usually non-radiative. This is, however, a reversible process, i.e., the emitters do emit light again after the trap is depopulated.

1.6.3 PL intensity and its fluctuations (blinking)

By measuring the PL intensity of the perovskite sample, we can understand the fundamental processes in detail. Due to the charge trapping described in the above section, the emitter can become dark (or gray) for a certain time and recover its emission at a later stage. This phenomenon is known as blinking and has been largely studied. There are different types of analyses that can be performed on the blinking of nanocrystals but so far there have been only a few reports of blinking for thin films.

One of the traditional ways to study blinking is to perform time-correlated photon measurements or, in other words, to measure when and how many photons arrive at the detector. The fluctuation of the intensity induced by the blinking is analyzed to obtain a histogram reporting for each time interval how many photons arrived. Once we have the histogram, we can inspect the distribution of the intensities in each time bin. We can then analyze the distributions of the different intensity levels such as on-states or off-states.

1.6.4 Microscopic PL spectra

From the microscopic emission spectra and their spatial variations, we can extract different information on the nanoscale emitters such as the central emission wavelength and the width of their emission. The peak emission wavelength is related to the energy bandgap and consequently to the local nanoscale composition of the perovskite sample. The spectral width can reflect the heterogeneity at the location. Other than spatial distribution, the time evolution of the nanoscale PL spectra can provide information on local dynamic processes

in the sample, such as, e.g., ion migration. On the other hand, at room temperature, any fine structure of the emission with different energy levels cannot be resolved in the spectrum.

1.7 Motivation

A fundamental challenge in the development of solar photovoltaic technology is a reduction in cost enabling direct competition with fossil-fuel-based energy sources. A key driver in this cost reduction is optimized device efficiency because increased energy output leverages all photovoltaic system costs, from raw materials and module manufacturing to installation and maintenance. To continue progress toward higher conversion efficiencies, solar cells are being fabricated with increasingly complex designs, including engineered nanostructures, heterojunctions, and novel contacting and passivation schemes. Such advanced designs require a comprehensive and unified understanding of optical and electrical device physics at the microscopic scale. This thesis establishes a microscopic understanding of solar cell optoelectronic performance and its impact on cell optimization.

For solution-processed semiconductors with domain sizes below a few micrometers, halide perovskites exhibit unprecedented carrier transport properties that enable their stellar performance in photovoltaics. Quantitatively characterizing this transport, understanding the material properties that give rise to it, and developing ways to improve it are all key directions for research. The intrinsic electrical properties, such as carrier type, concentration, mobility, and diffusion lengths in halide perovskites have exhibited a large range of values often influenced by the method used to prepare the films. Additionally, the lack of smooth and uniform films on which to perform measurements can make the determination of intrinsic electrical properties challenging since conventional techniques often assume the sample exhibits a specific geometry. However, it is not surprising that the mobility depends strongly on the preparation of the film. The electron mobility of polycrystalline $CH_3NH_3PbI_3$ films compares favorably to that of films of other materials used as absorbers in solar cells. It is larger than the thin-film mobility of polymers (10^{-7} to 1 $cm^2/V.s$)[69-70] and colloidal quantum dots (10^{-3} to 1 $cm^2/V.s$)[71] and it is comparable with that of CdTe (10 $cm^2/V.s$)[72], CIGS and Cu_2ZnSnS_4 (CZTS) (10 to 100 $cm^2/V.s$)[73-74] and polycrystalline Si (40 $cm^2/V.s$)[75]. Even in polycrystalline form, hybrid perovskites's inexpensive processing and tolerance to defects offer a significant advantage over conventional semiconductors.

As is the case for other polycrystalline semiconductors, electrical properties in hybrid perovskites are likely correlated with the film morphology. For instance, the dark and light conductivities of $CH_3NH_3PbI_{3-x}$ deposited on a planar scaffold or on mesostructured aluminum oxide are quite different[76]. This difference has been attributed to an increase in the perovskite Fermi level in the mesostructured scaffold either through more surface iodide vacancies or through electrostatic gating from the aluminum oxide. Also, the role of grain boundaries in conduction through perovskite films has not been thoroughly explored, although the passivation of grain boundaries with PbI_2 has been correlated to increased radiative lifetimes[77]. Inspired by the literature on organic solar cells, solvent annealing has been applied to $CH_3NH_3PbI_3$ solar cells to increase the grain size of the films to $\sim 1\ \mu m$[78]. Such processing results in an increase in the photovoltaic performance and radiative lifetime.

Presently thin films-based silicon solar cells[79-85] are commercialized, and fluorescence microscopy[86-90] has played an important role in the success of PV industrialization. Using fluorescence microscopy researchers have investigated basic materials physics, e.g., nanophotonic light trapping which has an impact on grain boundaries, heterojunctions, surface passivation, charge carrier transport, etc. which was helpful to optimize the optical and electrical properties of thin-film silicon solar cells. As a result a commercialized silicon-based PV- solar cell technology has been achieved successfully.

Similarly, these days thin film-based perovskite solar cells are getting much attention due to their promising semiconductor properties. Much research effort is dedicated to achieving high efficiencies, which requires a thorough understanding of the materials used to compose a solar cell. Like any common battery, a solar cell requires two contacts, one at the front and the other at the back. Sunlight first enters the solar cell through a transparent conductive front contact and is subsequently absorbed and converted into electricity in the perovskite absorber layer. Perovskite absorber layers can influence the electrical performance of the solar cell and therefore require a more elaborate and nuanced understanding. To build this understanding, material properties must be determined by characterization. The main aim of this thesis is to contribute to this understanding through advanced material characterization using fluorescence microscopy.

Similar to the use of fluorescence microscopy for the characterization of semiconductor solar cell materials, we aim to relate the microscopic relative PL efficiency with the local photovoltaic functionality. The concept is schematically summarized in the

Figure 1.7. Light absorbed by the perovskite crystals can generate excitons with very low binding energy which dissociate into free charge carriers in the form of electrons and holes. In an isolated defect-free film these carriers radiatively recombine together with a PLQY of 100%. On the other hand, in the presence of a defect, the charges can be trapped and recombine non-radiatively, leading to PLQY of less than 100%. Similarly, the perovskite film incorporated into a solar cell device in the presence of light should create the free charges that can be collected by the anode and cathode in the ideal case. But when there is a defect the charges are trapped and due to that photocurrent is reduced. In this way, the PL microscopic imaging and spectroscopy of perovskite films can be used to characterize the quality of the materials with respect to the photovoltaic functionality.

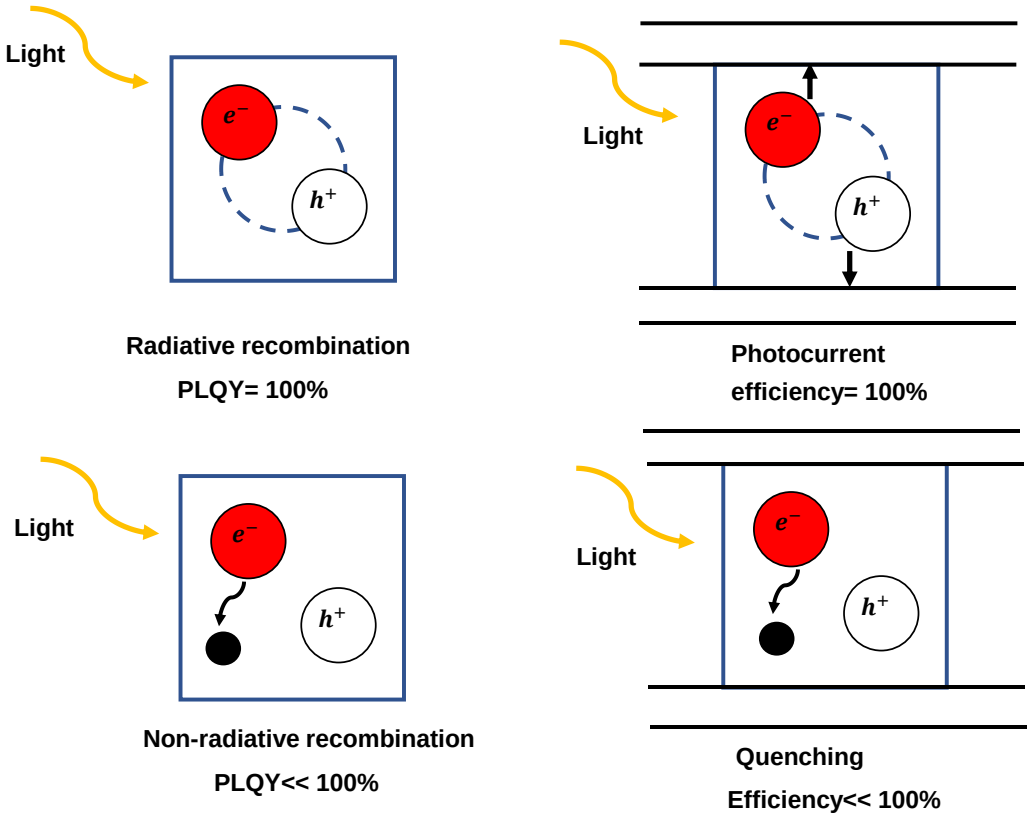

Figure 1.7. Schematic diagram of PL microscopy evaluation of photovoltaic materials

1.8 Outline of the thesis

This thesis presents a systematic study of the perovskite nanostructures and films with superior optoelectronic properties and stability for their applications in high-performance photodetectors, LEDs, and solar cells. We believe that these studies are very significant in addressing the current challenges of energy and environmental issues and multifunctional optoelectronic applications. The complete thesis work has been composed into 6 chapters, as detailed below:

Chapter 1 provides background and introduction to halide perovskites, fluorescence microscopy, and the mechanism of fluorescence intermittency. By quantifying and considering all the perovskite material's properties and thin films, the ultimate goal is directed to the study of perovskite thin films at the microscopic level.

In **Chapter 2** we have introduced basic concepts useful to understand the experimental work presented in the following. We have reviewed the effect of cation substitution in the perovskite structure, and the various factors in morphology optimization (such as stoichiometry engineering, crystallinity control, charge-carrier control, solvent engineering, etc.). The main part of the chapter describes preparation and optimization techniques to prepare the perovskite films for the microscopic study. The materials, their characterization using SEM and optical spectroscopy, and the microscopic experimental methods used in this dissertation are described in detail here.

In **Chapter 3** we provide a detailed fluorescence study of an important photovoltaic material as a series of mixed cation perovskite $MA_xFA_{1-x}PbI_3$ (where x = 0, 0.3, 0.5, 0.7, 0.9) films on the nanoscale. We have measured photoluminescence spectra on sub-micrometer scales which reveals the compositional heterogeneity of the MA/FA-based perovskite films. The compositional heterogeneity is largest for the FA 50% fraction films which contain pure MA, pure FA domains as well as mixed MA/FA domains. We have also found that the films show photoluminescence intensity fluctuations (blinking) which reflects dynamic quenching due to the non-radiative recombination. The quenching is most suppressed for the FA 50% films which contain the truly mixed MA/FA domains. Lastly, we have seen that the blinking is correlated between locations that are micrometers apart which indicates that the grain boundaries do not function as traps and are transparent toward efficient charge migration.

For halide perovskite thin films, a major challenge in understanding perovskite semiconductors is their stability under environmental condition and the gray area of their degradation process. In **Chapter 4**, we correlate the information from chapters 2 and 3 to study the effect of antisolvent on the air stability of mixed cation halide perovskite thin films over a year and reveal their degradation process. We have performed photoluminescence microscopic characterization of mixed cation perovskites films of the composition $MA_xFA_{1-x}PbI_3$ with x = 0, 0.3 and 0.5. We have seen that the perovskite films with x = 0.5 and 0.3 prepared in the air using ethyl acetate as an antisolvent in a one-step spin-coating process are compositionally stable in ambient air for more than a year as compared to the films prepared using the antisolvent of chlorobenzene. We have studied the degradation process of the films near the film edges as well as the center area of the film. The PL spectra of the degradation product are consistent with PL spectra of 2D perovskite sheets of the thickness of 5-7 layers. Morphologically, the aging of the films brings about coalescing of the film grain structure into larger crystal grains. Further, monitoring of the PL blinking from individual nanoscale locations in the films reveals that the aging of the films does not change the extent of dynamic PL quenching or affect the observed long-range charge diffusion on the order of micrometers.

In **Chapter 5**, we use our understanding of mixed-cation halide perovskite film performance in the presence of light, and attempt to study the film stability in environment that would resemble working solar cells. We applied an external electric field to the $MA_xFA_{1-x}PbI_3$ films in capacitance-like device to simulate the internal bias in working solar cells, and simultaneously monitored the PL behavior. Two completely different PL responses were observed in the same sample. Reversible PL quenching was observed under an electric field in locations characterized by changed morphology. PL intensity and spectral fluctuations due to externally applied field were found in homogeneous areas of the films. Both phenomena were attributed to migration of the iodine ions and vacancies due to the field. Filling of tne vacancies in a layer of the film close to the microscope objective lens causes appearance of new blue-shifted PL band which causes the apparent spectral fluctuations. Such results can help us to gain a deep insight into how the ionic movements in the perovskite absorber layer influence the performance of the perovskite-based optoelectronic devices under working conditions.

Finally, in **Chapter 6**, we concluded, through careful study and assessment, the work done in this thesis provides detailed knowledge about the nanoscale perspective in

perovskite thin films and their role in solar cell performance. We hope that our results will benefit the perovskite photovoltaic community and will provide more insights into improving film fabrication methodologies as well as other approaches to eliminate the formation of undesired defects in hybrid perovskite thin films.

1.9 References

1. Jeong, J.; Kim, M.; Seo, J.; Lu, H.; Ahlawat, P.; Mishra, A.; Yang, Y.; Hope, M. A.; Eickemeyer, F. T.; Kim, M.; Yoon, Y. J.; Choi, I. W.; Darwich, B. P.; Choi, S. J.; Jo, Y.; Lee, J. H.; Walker, B.; Zakeeruddin, S. M.; Emsley, L.; Rothlisberger, U.; Hagfeldt, A.; Kim, D. S.; Gratzel, M.; Kim, J. Y. Pseudo-halide anion engineering for α-$FAPbI_3$ perovskite solar cells. Nature **2021**, 592, 381−385
2. Nrel.gov/pv/cell-efficiency.html
3. Kojima, A.; Teshima, K.; Shirai, Y.; Miyasaka, T. Organometal Halide Perovskites as Visible-Light Sensitizers for Photovoltaic Cells. J. Am. Chem. Soc. **2009**, 131, 6050−6051.
4. Yi, Z.; Ladi, N. H.; Shai, X.; Li, H.; Shen, Y.; Wang, M. Will Organic−Inorganic Hybrid Halide Lead Perovskites be Eliminated from Optoelectronic Applications? Nanoscale Adv. **2019**, 1, 1276− 1289.
5. Chakhmouradian, A. R.; Woodward, P. M. Celebrating 175 Years of Perovskite Research: A Tribute to Roger H. Mitchell. Phys. Chem. Miner. **2014**, 41, 387−391.
6. Jena, A. K.; Kulkarni, A.; Miyasaka, T. Halide perovskite photovoltaics: background, status, and future prospects. Chem. Rev. **2019**, 119, 3036−3103.
7. Wells, H. L. über die Cäsium- und Kalium-Bleihalogenide. Zeitschrift für anorganische Chemie **1893**, 3, 195−210.
8. Weber, D. $CH_3NH_3PbX_3$, ein Pb(II)-System mit kubischer Perowskitstruktur/$CH_3NH_3PbX_3$, a Pb(II)-System with Cubic Perovskite Structure. Z. Naturforsch., B: J. Chem. Sci. **1978**, 33, 1443−1445.
9. Weber, D. $CH_3NH_3SnBr_xI_{3-x}$ (x = 0−3), ein Sn(II)-System mit kubischer Perowskitstruktur/$CH_3NH_3SnBr_xI_{3-x}$(x = 0−3), a Sn(II)- System with Cubic Perovskite Structure. Z. Naturforsch., B: J. Chem. Sci. **1978**, 33, 862−865.
10. Møller, C. K. A Phase Transition in Cesium Plumbochloride. Nature **1957**, 180, 981−982.
11. Møller, C. K. Crystal Structure and Photoconductivity of Cesium Plumbohalides. Nature **1958**, 182, 1436−1436.
12. Mitzi, D. B. Synthesis, Structure, and Properties of Organic- Inorganic Perovskites and Related Materials. Progress in Inorganic Chemistry; John Wiley and Sons, **1999**, 48,1−122.

13. Mitzi, D. B. Organic−Inorganic Perovskites Containing Trivalent Metal Halide Layers: The Templating Influence of the Organic Cation Layer. Inorg. Chem. **2000**, 39, 6107−6113.
14. Mitzi, D. B.; Wang, S.; Feild, C. A.; Chess, C. A.; Guloy, A. M. Conducting Layered Organic-inorganic Halides Containing < 110>- Oriented Perovskite Sheets. Science **1995**, 267, 1473.
15. Era, M.; Oka, S. PbBr-based layered perovskite film using the Langmuir−Blodgett technique. Thin Solid Films **2000**, 376, 232−235.
16. Takeoka, Y.; Asai, K.; Rikukawa, M.; Sanui, K. Incorporation of Conjugated Polydiacetylene Systems into Organic−inorganic Quantum- well Structures. Chem. Commun. **2001**, 2592−2593.
17. Kondo, T.; Iwamoto, S.; Hayase, S.; Tanaka, K.; Ishi, J.; Mizuno, M.; Ema, K.; Ito, R. Resonant Third-order Optical Nonlinearity in The Layered Perovskite-type Material $(C_6H_{13}NH_3)_2PbI_4$. Solid State Commun. **1998**, 105, 503−506.
18. Tanaka, K.; Kondo, T. Bandgap and Exciton Binding Energies in Lead-iodide-based Natural quantum-well Crystals. Sci. Technol. Adv. Mater. **2003**, 4, 599−604.
19. Ema, K.; Umeda, K.; Toda, M.; Yajima, C.; Arai, Y.; Kunugita, H.; Wolverson, D.; Davies, J. J. Huge Exchange Energy and Fine Structure of Excitons in an Organic-inorganic Quantum Well Material. Phys. Rev. B: Condens. Matter Mater. Phys. **2006**, 73, 241310.
20. Ishi, J.; Mizuno, M.; Kunugita, H.; Ema, K.; Iwamoto, S.; Hayase, S.; Kondo, T.; Ito, R. Third-Order Optical Nonlinearity Due to Excitons and Biexcitons in a Self-Organized Quantum-Well Material $(C_6H_{13}NH_3)_2PbI_4$. J. Nonlinear Opt. Phys. Mater. **1998**, 07, 153−159.
21. Miyasaka, T.; Ikegami, M.; Kijitori, Y. Photovoltaic Performance of Plastic Dye-Sensitized Electrodes Prepared by Low-Temperature Binder-Free Coating of Mesoscopic Titania. J. Electrochem. Soc. **2007**, 154, A455−A461.
22. Ikeda, N.; Teshima, K.; Miyasaka, T. Conductive polymer− carbon−imidazolium composite: a simple means for constructing solid-state dye-sensitized solar cells. Chem. Commun. **2006**, 16, 1733−1735.
23. Miyasaka, T. Toward Printable Sensitized Mesoscopic Solar Cells: Light-Harvesting Management with Thin TiO_2 Films. J. Phys. Chem. Lett. **2011**, 2, 262−269.

24. Quan, L. N.; Rand, B. P.; Friend, R. H.; Mhaisalkar, S. G.; Lee, T. W.; Sargent, E. H. Perovskites for Next-Generation Optical Sources. Chem. Rev. **2019**, 119, 7444−7477.
25. Stranks, S. D.; Eperon, G. E.; Grancini, G.; Menelaou, C.; Alcocer, M. J. P.; Leijtens, T.; Herz, L. M.; Petrozza, A.; Snaith, H. J. Electron-Hole Diffusion Lengths Exceeding 1 Micrometer in an Organometal Trihalide Perovskite Absorber. Science **2013**, 342, 341−344.
26. Sutherland, B. R.; Sargent, E. H. Perovskite Photonic Sources. Nat. Photonics **2016**, 10, 295−302.
27. Era, M.; Morimoto, S.; Tsutsui, T.; Saito, S. Organic-Inorganic Heterostructure Electroluminescent Device Using a Layered Perovskite Semiconductor $(C_6H_5C_2H_4NH_3)_2PbI_4$. Appl. Phys. Lett. **1994**, 65, 676−678.
28. Tan, Z. K.; Moghaddam, R. S.; Lai, M. L.; Docampo, P.; Higler, R.; Deschler, F.; Price, M.; Sadhanala, A.; Pazos, L. M.; Credgington, D.; et al. Bright Light-Emitting Diodes Based on Organometal Halide Perovskite. Nat. Nanotechnol. **2014**, 9, 687−692.
29. Cho, H.; Jeong, S. H.; Park, M. H.; Kim, Y. H.; Wolf, C.; Lee, C. L.; Heo, J. H.; Sadhanala, A.; Myoung, N.; Yoo, S.; et al. Overcoming the Electroluminescence Efficiency Limitations of Perovskite Light-Emitting Diodes. Science **2015**, 350, 1222−1225.
30. Wang, Z.; Shi, Z.; Li, T.; Chen, Y.; Huang, W. Stability of Perovskite Solar Cells: A Prospective on the Substitution of the A Cation and X Anion. Angew. Chem., Int. Ed. **2017**, 56, 1190−1212.
31. Knight, A. J.; Herz, L. M. Preventing Phase Segregation in Mixed-Halide Perovskites: A Perspective. Energy Environ. Sci. **2020**, 13, 2024−2046
32. Matsui, T.; Seo, J.-Y.; Saliba, M.; Zakeeruddin, S. M.; Gratzel, M. Room-Temperature Formation of Highly Crystalline Multication Perovskites for Efficient, Low-Cost Solar Cells. Adv. Mater. **2017**, 29, 1606258.
33. Kim, J.; Kim, H. P.; Teridi, M. A. M.; Yusoff, A. R. b. M.; Jang, J. Bandgap Tuning of Mixed Organic Cation Utilizing Chemical Vapor Deposition Process. Sci. Rep. **2016**, 6, 37378.
34. Wen, X. M.; Sheng, R.; Ho-Baillie, A. W. Y.; Benda, A.; Woo, S.; Ma, Q. S.; Huang, S. J.; Green, M. A. Morphology and Carrier Extraction Study of Organic-Inorganic Metal Halide Perovskite by One- and Two-Photon Fluorescence Microscopy. J. Phys. Chem. Lett. **2014**, 5, 3849−3853.

35. deQuilettes, D. W.; Vorpahl, S. M.; Stranks, S. D.; Nagaoka, H.; Eperon, G. E.; Ziffer, M. E.; Snaith, H. J.; Ginger, D. S. Impact of microstructure on local carrier lifetime in perovskite solar cells. Science **2015**, 348, 683−686.
36. Miller, O. D.; Yablonovitch, E.; Kurtz, S. R. Strong Internal and External Luminescence as Solar Cells Approach the Shockley-Queisser Limit. IEEE Photovoltaics **2012**, 2, 303−311.
37. Dey, A.; Ye, J.; De, A.; Debroye, E.; Ha, S. K.; Bladt, E.; Kshirsagar, A. S.; Wang, Z.; Yin, J.; Wang, Y.; et al. State of the Art and Prospects for Halide Perovskite Nanocrystals. ACS Nano **2021**, 15, 10775−10981.
38. Yin, B.; Cavin, J.; Wang, D.; Khan, D.; Shen, M.; Laing, C.; Mishra, R.; Sadtler, B., Fluorescence Microscopy of Single Lead Bromide Nanocrystals Reveals Sharp Transitions during Their Transformation to Methylammonium Lead Bromide. Journal of Materials Chemistry C **2019**, 7 (12), 3486-3495.
39. Yoshimura, H.; Yamauchi, M.; Masuo, S., In Situ Observation of Emission Behavior during Anion-Exchange Reaction of a Cesium Lead Halide Perovskite Nanocrystal at the SingleNanocrystal Level. The Journal of Physical Chemistry Letters **2020**, 11 (2), 530-535.
40. Liu, L.; Deng, L.; Huang, S.; Zhang, P.; Linnros, J.; Zhong, H.; Sychugov, I., Photodegradation of Organometal Hybrid Perovskite Nanocrystals: Clarifying the Role of Oxygen by Single-Dot Photoluminescence. The Journal of Physical Chemistry Letters **2019**, 10 (4), 864-869.
41. Wang, S.; Querner, C.; Dadosh, T.; Crouch, C. H.; Novikov, D. S.; Drndic, M., Collective Fluorescence Enhancement in Nanoparticle Clusters. Nature Communications **2011**, 2 (1), 364.
42. Huang, C.-H.; Wen, Y.-H.; Liu, Y.-W., Measuring the Second Order Correlation Function and the Coherence Time using Random Phase Modulation. Optics Express **2016**, 24 (4), 4278-4288.
43. Lounis, B.; Bechtel, H. A.; Gerion, D.; Alivisatos, P.; Moerner, W. E., Photon Antibunching in Single CdSe/ZnS Quantum Dot Fluorescence. Chemical Physics Letters **2000**, 329 (5), 399-404.
44. Orfield, N. J.; McBride, J. R.; Keene, J. D.; Davis, L. M.; Rosenthal, S. J., Correlation of Atomic Structure and Photoluminescence of the Same Quantum Dot: Pinpointing

Surface and Internal Defects That Inhibit Photoluminescence. ACS Nano **2015**, 9 (1), 831-839.

45. Orfield, N. J.; Majumder, S.; McBride, J. R.; Yik-Ching Koh, F.; Singh, A.; Bouquin, S. J.; Casson, J. L.; Johnson, A. D.; Sun, L.; Li, X.; Shih, C.-K.; Rosenthal, S. J.; Hollingsworth, J. A.; Htoon, H., Photophysics of Thermally Assisted Photobleaching in "Giant" Quantum Dots Revealed in Single Nanocrystals. ACS Nano **2018**, 12 (5), 4206-4217.
46. Reid, K. R.; McBride, J. R.; La Croix, A. D.; Freymeyer, N. J.; Click, S. M.; Macdonald, J. E.; Rosenthal, S. J., Role of Surface Morphology on Exciton Recombination in Single Quantum Dot-in-Rods Revealed by Optical and Atomic Structure Correlation. ACS Nano **2018**, 12 (11), 11434-11445.
47. McBride, J. R.; Mishra, N.; Click, S. M.; Orfield, N. J.; Wang, F.; Acharya, K.; Chisholm, M. F.; Htoon, H.; Rosenthal, S. J.; Hollingsworth, J. A., Role of Shell Composition and Morphology in Achieving Single-Emitter Photostability for Green-Emitting "Giant" Quantum Dots. The Journal of Chemical Physics **2020**, 152 (12), 124713.
48. Gutiérrez-Arzaluz, L.; Ahmed, G. H.; Yang, H.; Shikin, S.; Bakr, O. M.; Malko, A. V.; Mohammed, O. F., Correlation of Photoluminescence and Structural Morphologies at the Individual Nanoparticle Level. The Journal of Physical Chemistry A **2020**, 124 (23), 4855-4860.
49. Andoy, N. M.; Zhou, X.; Choudhary, E.; Shen, H.; Liu, G.; Chen, P., Single-Molecule Catalysis Mapping Quantifies Site-Specific Activity and Uncovers Radial Activity Gradient on Single 2D Nanocrystals. Journal of the American Chemical Society **2013**, 135 (5), 1845-1852.
50. Nirmal, M.; Norris, D. J.; Kuno, M.; Bawendi, M. G.; Efros, A. L.; Rosen, M., Observation of the "Dark Exciton" in CdSe Quantum Dots. Physical Review Letters **1995**, 75 (20), 3728-3731.
51. Efros, A. L.; Rosen, M.; Kuno, M.; Nirmal, M.; Norris, D. J.; Bawendi, M., Band-Edge Exciton in Quantum Dots of Semiconductors with a Degenerate Valence Band: Dark and Bright Exciton States. Physical Review B **1996**, 54 (7), 4843-4856.
52. Gan, Z.; Chen, W.; Yuan, L.; Cao, G.; Zhou, C.; Huang, S.; Wen, X.; Jia, B., External Stokes Shift of Perovskite Nanocrystals Enlarged by Photon Recycling. Applied Physics Letters **2019**, 114 (1), 011906.

53. Guo, Y.; Yaffe, O.; Hull, T. D.; Owen, J. S.; Reichman, D. R.; Brus, L. E., Dynamic Emission Stokes Shift and Liquid-Like Dielectric Solvation of Band Edge Carriers in LeadHalide Perovskites. Nature Communications **2019**, 10 (1), 1175.
54. Brennan, M. C.; Forde, A.; Zhukovskyi, M.; Baublis, A. J.; Morozov, Y. V.; Zhang, S.; Zhang, Z.; Kilin, D. S.; Kuno, M., Universal Size-Dependent Stokes Shifts in Lead Halide Perovskite Nanocrystals. The Journal of Physical Chemistry Letters **2020**, 11 (13), 4937-4944.
55. Yuan, G.; Gómez, D. E.; Kirkwood, N.; Boldt, K.; Mulvaney, P., Two Mechanisms Determine Quantum Dot Blinking. ACS Nano **2018**, 12 (4), 3397-3405.
56. Galland, C.; Ghosh, Y.; Steinbrück, A.; Sykora, M.; Hollingsworth, J. A.; Klimov, V. I.; Htoon, H., Two Types of Luminescence Blinking Revealed by Spectro electrochemistry of Single Quantum Dots. Nature **2011**, 479 (7372), 203-207.
57. Chouhan, L.; Ito, S.; Thomas, E. M.; Takano, Y.; Ghimire, S.; Miyasaka, H.; Biju, V., Real-Time Blinking Suppression of Perovskite Quantum Dots by Halide Vacancy Filling. ACS Nano **2021**, 15 (2), 2831-2838.
58. Trinh, C. T.; Minh, D. N.; Ahn, K. J.; Kang, Y.; Lee, K.-G., Verification of Type-A and Type-B-HC Blinking Mechanisms of Organic–Inorganic Formamidinium Lead Halide Perovskite Quantum Dots by FLID Measurements. Scientific Reports **2020**, 10 (1), 2172.
59. Shimizu, K. T.; Neuhauser, R. G.; Leatherdale, C. A.; Empedocles, S. A.; Woo, W. K.; Bawendi, M. G., Blinking Statistics in Single Semiconductor Nanocrystal Quantum Dots. Physical Review B **2001**, 63 (20), 205316.
60. Zhang, A.; Dong, C.; Ren, J., Tuning Blinking Behavior of Highly Luminescent Cesium Lead Halide Nanocrystals through Varying Halide Composition. The Journal of Physical Chemistry C **2017**, 121 (24), 13314-13323.
61. Efros, A. L.; Nesbitt, D. J., Origin and Control of Blinking in Quantum Dots. Nature Nanotechnology **2016**, 11 (8), 661-671.
62. Thomas, E. M.; Ghimire, S.; Kohara, R.; Anil, A. N.; Yuyama, K.-i.; Takano, Y.; Thomas, K. G.; Biju, V., Blinking Suppression in Highly Excited CdSe/ZnS Quantum Dots by Electron Transfer under Large Positive Gibbs (Free) Energy Change. ACS Nano **2018**, 12 (9), 9060-9069.
63. Roy, D.; Mandal, S.; De, C. K.; Kumar, K.; Mandal, P. K., Nearly Suppressed Photoluminescence Blinking of Small-Sized, Blue–Green–Orange–Red emitting Single CdSe based Core/Gradient Alloy Shell/Shell Quantum Dots: Correlation between

Truncation Time and Photoluminescence Quantum Yield. Physical Chemistry Chemical Physics **2018**, 20 (15), 10332- 10344.

64. Ahmed, T.; Seth, S.; Samanta, A., Mechanistic Investigation of the Defect Activity Contributing to the Photoluminescence Blinking of $CsPbBr_3$ Perovskite Nanocrystals. ACS Nano **2019**, 13 (11), 13537-13544.
65. Stewart, C.; Giannini, J., Inexpensive, Open-Source Epifluorescence Microscopes. Journal of Chemical Education 2016, 93 (7), 1310-1315. 66.
66. Zhang, Y.; Gross, H., Systematic Design of Microscope Objectives. Part I: System Review and Analysis. Advanced Optical Technologies **2019**, 8 (5), 313-347. 27
67. Routzahn, A. L.; Jain, P. K., Single-Nanocrystal Reaction Trajectories Reveal Sharp Cooperative Transitions. Nano Letters **2014**, 14 (2), 987-992.
68. Smith, M. D.; Connor, B. A.; Karunadasa, H. I. Tuning the luminescence of layered halide perovskites. Chem. Rev. **2019**, 119, 3104−3139.
69. Venkateshvaran, D.; Nikolka, M.; Sadhanala, A.; Lemaur, V.; Zelazny, M.; M. Hurhangee, M. Kepa; Kronemeijer, A. J.; Pecunia, V.; Nasrallah, I.; Romanov, I.; Broch, K.; McCulloch, I.; Emin, D.; Olivier, Y.; Cornil, J.; Beljonne, D.; and Sirringhaus, H. Approaching disorder-free transport in high-mobility conjugated polymers, Nature **2014**, 515, 384.
70. You, J.; Dou, L.; Hong, Z.; Li, G.; and Yang, Y. Recent trends in polymer tandem solar cells research, Polym. Sci. **2013**, 38, 1909.
71. Sandeep, C.; Cate, S.; Schins, J. et al. High charge-carrier mobility enables exploitation of carrier multiplication in quantum-dot films, Nature Comm. **2013,** 4, 2360.
72. Long, Q.; Dinca, S. A.; Schiff, E. A.; Yu, M.; and Theil, J. Electron and hole drift mobility measurements on thin film CdTe solar cells, Appl. Phys. Lett. **2014**, 105, 042106.
73. Shin, B.; Gunawan, O.; Zhu, Y.; Bojarczuk, N. A.; Chey, S. J.; and Guha, S. Thin film solar cell with 8.4% power conversion efficiency using an earth-abundant Cu_2ZnSnS_4 absorber, Prog. Photovolt. Res. Appl. **2013**, 21, 72.
74. Brown, G.; Faifer, V.; Pudov, A.; Anikeev, S.; Bykov, E.; Contreras, M.; Wu, J. Determination of the minority carrier diffusion length in compositionally graded Cu(In,Ga)Se2 solar cells using electron beam induced current. Appl. Phys. Lett. 2010, 96 (2), 022104

75. Kamins, T. I. Hall mobility in chemically deposited polycrystalline silicon. J. Appl. Phys. 1971, 42, 4357−4365.
76. Leijtens, T.; Stranks, S. D.; Eperon, G. E.; Lindblad, R.; Johansson, E. M. J.; McPherson, I. J.; Rensmo, H.; Ball, J. M.; Lee, M. M.; Snaith, H. J. Electronic Properties of Meso Superstructured and Planar Organometal Halide Perovskite Films: Charge Trapping, Photodoping, and Carrier Mobility. ACS Nano **2014**, 8, 7147−7155.
77. Chen, Q.; Zhou, H. P.; Song, T. B.; Luo, S.; Hong, Z. R.; Duan, H. S.; Dou, L. T.; Liu, Y. S.; Yang, Y. Controllable Self-Induced Passivation of Hybrid Lead Iodide Perovskites toward High Performance Solar Cells. Nano Lett. **2014**, 14, 4158−4163.
78. Xiao, Z.; Dong, Q.; Bi, C.; Shao, Y.; Yuan, Y.; Huang, J. Solvent annealing of perovskite-induced crystal growth for photovoltaic-device efficiency enhancement. Adv. Mater. **2014**, 26 (37), 6503−6509.
79. Deceglie, M. G.; Ferry, V. E., Alivisatos; A. P. & Atwater; H., A. Accounting for Localized Defects in the Optoelectronic Design of Thin-Film Solar Cells. IEEE Journal of Photovoltaics **2013**, 3, 599–604.
80. Grandidier, J.; Weitekamp, R. A.; Deceglie, M. G.; Callahan, D. M.; Battaglia, C.; Bukowsky, C. R.; Ballif, C.; Grubbs, R. H.; Atwater, H. A. Solar Cell Efficiency Enhancement via Light Trapping in Printable Resonant Dielectric Nanosphere Arrays. Phys. Status Solidi A **2013**, 210 (2), 255−260.
81. Grandidier, J.; Deceglie, M. G.; Callahan, D. M.; Atwater, H. A. Simulations of Solar Cell Absorption Enhancement Using Resonant Modes of a Nanosphere Array. Proc. SPIE **2012**, 2, 825603.
82. Deceglie, M. G.; Ferry, V. E.; Alivisatos, A. P.; Atwater, H. A. Design of Nanostructured Solar Cells Using Coupled Optical and Electrical Modeling. Nano Lett. **2012**, 12, 2894−2900.
83. Deceglie, M.G.; and Atwater, H.A. Effect of defect-rich epitaxy on crystalline silicon / amorphous silicon heterojunction solar cells and the use of low-mobility layers to improve performance," Proceedings of the Thirty-Seventh IEEE Photovoltaic Specialists Conference (PVSC), **2011**, 001417–001429.
84. Deceglie, M.G.; Kelzenberg, M.D.; and Atwater, H.A. Effects of bulk and grain boundary recombination on the efficiency of columnar-grained crystalline silicon film solar cells, Proceedings of the Thirty-Fifth IEEE Photovoltaic Specialists Conference (PVSC), **2010**, 1487–1490.

85. Deceglie, M.G.; Emmer, H.S.; Holman, Z.C.; Descoeudres, A.; Wolf, S. De; Ballif, C.; and Atwater, H.A., Scanning laser-beam-induced current measurements of lateral transport near junction defects in silicon heterojunction solar cells, IEEE Journal of Photovoltaics **2014**, 4 (1),154–159.
86. Pi, X. D.; Mangolini, L.; Campbell, S. A.; Kortshagen, U. RoomTemperature Atmospheric Oxidation of Si Nanocrystals after HF Etching. Phys. Rev. B: Condens. Matter Mater. Phys. **2007**, 75, 85423.
87. Dasog, M.; Yang, Z.; Regli, S.; Atkins, T. M.; Faramus, A.; Singh, M. P.; Muthuswamy, E.; Kauzlarich, S. M.; Tilley, R. D.; Veinot, J. G. C. Chemical Insight into the Origin of Red and Blue Photoluminescence Arising from Freestanding Silicon Nanocrystals. ACS Nano **2013**, 7, 2676−2685
88. Hannah, D. C.; Yang, J.; Kramer, N. J.; Schatz, G. C.; Kortshagen, U. R.; Schaller, R. D. Ultrafast Photoluminescence in Quantum-Confined Silicon Nanocrystals Arises from an Amorphous Surface Layer. ACS Photonics **2014**, 1, 960−967.
89. Dasog, M.; De los Reyes, G. B. D.; Titova, L. V.; Hegmann, F. A.; Veinot, J. G. C. Size vs Surface: Tuning the Photoluminescence of Freestanding Silicon Nanocrystals Across the Visible Spectrum via Surface Groups. ACS Nano **2014**, 8, 9636−9648.
90. Kim, S.; Lee, J.; Sung, J. H.; Seo, D.-j.; Kim, I.; Jo, M.-H.; Kwon, B.; Choi, W. K.; Choi, H.-J. Two-Dimensionally Grown SingleCrystal Silicon Nanosheets with Tunable Visible-Light Emissions. ACS Nano 2014, 8, 6556−6562.

Chapter 2

Fabrication and optimization of mixed cation (MA/FA) based perovskite thin films

2.1 Introduction

2.1.1 Key properties of halide perovskites

The most fascinating property of halide-based perovskites is that they are direct-bandgap semiconductors with very large absorption coefficients of up to ~$10^5 cm^{-1}$ in the UV-visible range.[1-4] The optical absorption coefficient of a perovskite material is closely related to its electronic structure. Due to the strong light absorption, a very thin layer of perovskite is effective for different optoelectronic applications. Interestingly, the bandgap of halide perovskites can be tuned by chemical substitution without significant changes in the fundamental electronic properties. Generally, the bandgap and transport properties of halide perovskite can be tuned by changing the A-site cation, the B-site metal cation, or the X-site halide anion. The most common way to tune the bandgap of perovskites over the entire UV-visible region is the substitution of halide content from Cl^- to Br^- to I^-. For example, the bandgaps of $CH_3NH_3PbCl_3$, $CH_3NH_3PbBr_3$, and $CH_3NH_3PbI_3$ are observed to be ~3.1 eV, 2.2 eV, and 1.6 eV, respectively.[5] For other mixed halide perovskites, the bandgap was found to lie between 1.6 eV and 3.1 eV depending upon the halide ions. But changing of A-site cation also slightly affects the bandgap. For instance, by replacing methylammonium (MA^+) with formamidinium (FA^+) cation, which is a slightly larger molecule, the bandgap[6] changes from 1.6 to ~1.47 eV. As perovskite is a direct bandgap semiconductor, it shows strong photoluminescence (PL) emission due to the band edge excitonic recombination. Typically, the photogenerated carrier generation and exciton recombination efficiency varies for different halide perovskites. For example, iodine-based perovskites ($CH_3NH_3PbI_3$ or $CsPbI_3$) exhibit very high photogenerated carrier generation with low radiative recombination, which is suitable for solar cell and photodetection applications. On the other hand, bromine-based perovskites ($CH_3NH_3PbBr_3$ or $CsPbBr_3$) show high radiative recombination with high photoluminescence quantum yield (PLQY) suitable for LED applications. However, carrier generation and recombination of perovskites not only depends on halide ions but also depends upon A-site cations.

The A-site cation (e.g., $CH_3NH_3^+$ (MA+), $CH(NH_2)_2^+$ (FA^+), Cs^+) occupies the central position of the 3D perovskite structure which is a key part of the perovskite that determines its structure and dimensionality. It has a direct influence on the stability and optoelectronic properties of the material. As shown in the below Figure 2.1 for the effective

substitution of the A-site cation with respect to a tolerance factor, the incorporation of cations with radii similar to the original cation into the 3D perovskite structure can improve the device's performance. The tolerance factor *t* was suggested to determine the stability of the perovskite phase for a given set of anions and cations. The tolerance factor and perovskite cell parameter are two important parameters related to the symmetry of perovskites that significantly affect the dielectric properties.[7] Goldschmidt[8] defined the tolerance factor to account for the limits of the size of the cations to form a perovskite structure as

$$t = \frac{r_A + r_X}{\sqrt{2}(r_B + r_X)}$$

where r_A is the radius of the A cation, r_B is the radius of the B cation and r_X is the radius of the anion.

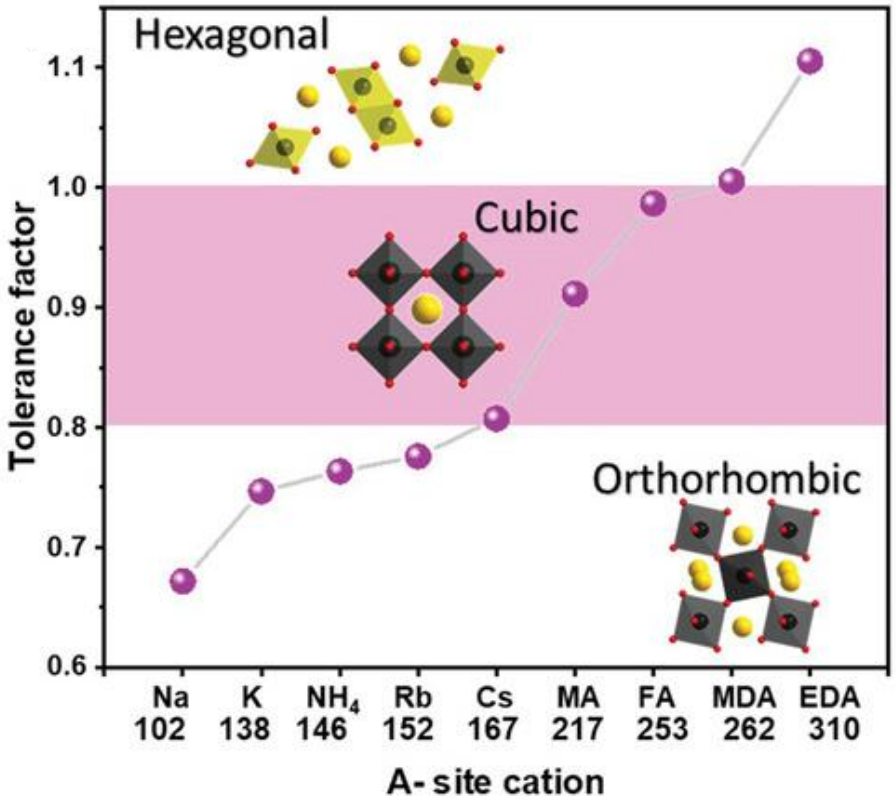

Figure 2.1. Dependency of tolerance factor of $APbI_3$ perovskites depending on A-cation radius. Colored part means region for stable cubic structure ($0.8 < t < 1$) (reproduced from ref. 1 with permission).

The aim of substituting the A-site cation is to obtain a more-stable cubic phase and the appropriate dynamic position of the conduction band of the perovskite films, which plays a major role in improving the stability.[1,9]

2.1.2 Effect of the FA Cation

The most investigated organic cation counterpart for the substitution of the MA ion has been the FA ion. $FAPbI_3$ perovskite has a similar crystal structure to $MAPbI_3$. Moreover, compared to MA, FA has a relatively large radius and was confirmed to form a 3D perovskite with a lower band gap of about 1.47 eV.[10-14] The organic cation was considered not taking part in determining the band structure but works to fulfill charge neutrality within the lattice.[15-17] However, its size is vital. The size of the organic cation can cause the entire network to enlarge or be compressed. Therefore, both stability and performance could be expected to improve simultaneously. Park et al. demonstrated that $FAPbI_3$ perovskite has good thermal stability at a temperature of 150 ºC.[18]

Using a chemical vapor deposition method to fabricate $FAPbI_3$ and $MAPbI_3$ thin films, the $FAPbI_3$ is more stable than the $MAPbI_3$ in the air with a relative humidity of 50%[19-20] The improvement of thermal stability may be attributed to the more stable cubic phase of $FAPbI_3$ compared to the tetragonal phase of $MAPbI_3$. In fact, the interaction between the A cations and the halides in the perovskite structure mainly occurs through hydrogen bonding between the acidic MA or FA hydrogen atoms and the perovskite iodides. Furthermore, regardless of the cation size, the tetragonal-to-quasi-cubic structural evolution when moving from MA to FA is due to enhanced hydrogen bonding to the inorganic matrix which alters the covalent/ionic character of Pb-I bonds.[21] Therefore, the greater thermal stability of $FAPbI_3$ in nitrogen and oxygen may originate from the enhanced hydrogen bonding between FA and I since FA has a higher propensity to form hydrogen bonds.[22-24] This propensity may be due to the statistically enhanced probability of forming hydrogen bonds because of the increased number of protons in FA than in MA. The light stability in humidity of $FAPbI_3$ is also improved compared to $MAPbI_3$.[25-26] The main mechanism of the poor light stability of $MAPbI_3$ is that MA will release protons under light illumination, which makes the protons and the I ions combine to generate HI.[27-28] For $FAPbI_3$, the main reason for the stability under light illumination is that it is difficult for FA to release protons.

This is mainly because the FA is stabilized by the resonance characteristics of the C-N bonds.[29-33]

As shown in the below Figure 2.2, $MAPbI_3$ and $FAPbI_3$ perovskite both showed very poor thermal stability in hole-conductor-free perovskite solar cells. A $MAPbI_3$ perovskite thin film with the best surface coverage is formed when the annealing temperature is 100 ^oC. However, at a high temperature, it becomes yellow, which suggests $MAPbI_3$ gradually decomposes into PbI_2, indicating serious thermal instability. However, phase instability is a major challenge for $FAPbI_3$ because their black perovskite phases undergo a transition to a non-photoactive yellow phase at room temperature. $FAPbI_3$ has four types of crystal polymorphs phases (Figure 2.2): cubic (α-), trigonal (β-), tetragonal (γ-), and hexagonal non-perovskite phase (δ-), all leading to different optoelectronic properties.[4]

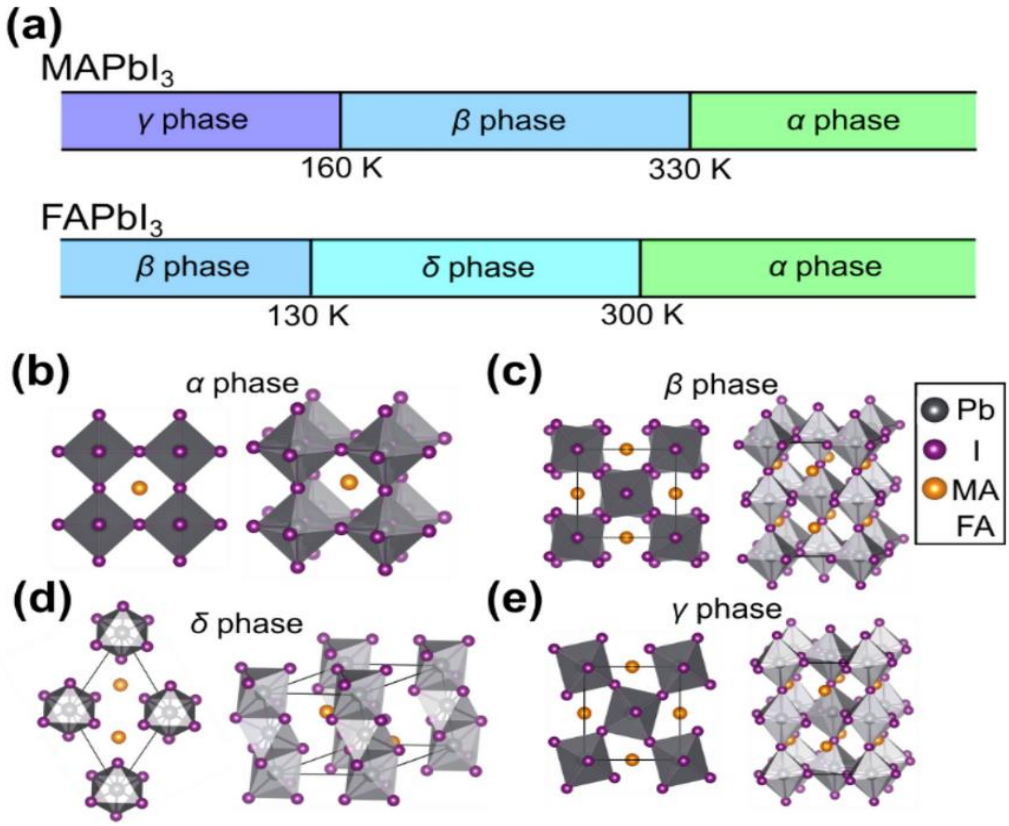

Figure 2.2. (a) The phase variations of $MAPbI_3$ and $FAPbI_3$ at various temperatures. There are four different phases: (b) the cubic alpha (α) phase, (c) the tetragonal beta (β) phase, (d) the trigonal delta (δ) phase, and (e) the orthorhombic gamma (γ) phase. (b)–(e) Gray and purple spheres indicate lead and iodine atoms, respectively. The methylammonium (MA) or formamidinium (FA) molecular units are represented by orange spheres (reproduced from ref. 4 with permission).

2.1.3 Possibility of A-site cation alteration

As we have discussed the several pros and cons of different A-site cations it is important to look at the alteration of A-site cations more carefully. In this section, we will discuss the state-of-the-art possibilities of mixed-cation perovskites based on multiple substitutions on the A-site of the perovskite and their effect on the efficiency and long-term stability of perovskites in solar cells.

Mixing cations has become a hot topic to simultaneously improve both the structural stability and efficiency of perovskite solar cells. The partial substitution of the A-site cation in $MAPbI_3$ and $FAPbI_3$, thin films have been exploited to control the phase, humidity, and thermal stability, as well as tune the optical properties.[20–26,34] Although both pure MA- and FA-based perovskite compositions are sensitive to ambient conditions, the double A-site cation perovskites, that is, a mixture A site cation of MA and FA, have shown a great potential to stabilize the crystal lattice.[4,9,18,35]The mixed perovskite with partial substitution of MA by FA showed no significant change in surface coverage under annealing temperatures of 100 °C, 175 °C, and 230 °C, indicating that the partial substitution of MA is a way to improve perovskite thermal stability.

The recent advances in the substitution of A-cations are related to their effect on the long-term stability of perovskites with regards to moisture, heat, light, and oxygen. The structural stability over thousands of hours under various conditions must be demonstrated, or else, the devices will probably not be attractive for commercial applications. Having elucidated the mechanisms of instability, it has been concluded that chemical modification has provided promising results with significantly enhanced stability. Partial substitution of FA by MA can give the stable phase under low temperatures and is beneficial to perovskite stability. Moreover, stability against moisture and light illumination can be remarkably enhanced by partly substituting FA. The preparation of 2D perovskite by the insertion of larger cations, into the 3D $MAPbI_3$ lattice, can also improve stability compared to that of the 3D $MAPbI_3$ analogs, making them more attractive for large-scale industrial implementation.

As discussed so far, the double cations system helps to stabilize the pure single cation perovskites, that is, $MAPbI_3$, $FAPbI_3$, and $CsPbI_3$. The MA cation plays an important role in FA/MA perovskites as a crystallizer and black phase stabilizer. Despite high perovskite cell efficiency(PSCs) of FA/MA perovskites, obtaining a FA/MA perovskite

without any trace of the yellow phase is always challenging, and this negatively affects the long-term device stability.[2,4,16,36-45] Therefore, developing a new composition engineering approach to achieve pure black phase in double cations system without affecting the other parameters is very important for further developments of PSCs. To address this challenge, researchers introduced triple cations FA/MA/Cs to improve further the properties of the double cation system[46-48]. Introducing small amounts of Cs (5–15%) to the FA/MA perovskite leads to the disappearance of the photoinactive hexagonal δ-phase and the cubic PbI_2. This effect is due to a reduction of the effective cation radius in the new triple Cs/MA/FA system, pushing the tolerance factor towards the stable cubic α-phase perovskite. The triple cations perovskite films showed higher thermal stability and reproducibility regarding PEC compared to the double cations counterpart, which is very crucial for the further development of cost-efficient manufacturing PSCs.[11,49] As a result, the triple cations-based PSCs delivered a high stabilized PCE of 21.1% and ≈18% after 250 h under operational conditions. Many groups also confirmed the robustness of the Cs/MA/FA triple cation perovskite composition in terms of reproducibility, efficiency, and stability.[1,13,50-52] The Cs/MA/FA triple cation perovskite became a very reproducible and favorable composition in the perovskite community. Yet, the presence of the highly volatile MA cation in this composition is considered a long-term risk for universalizing this composition.

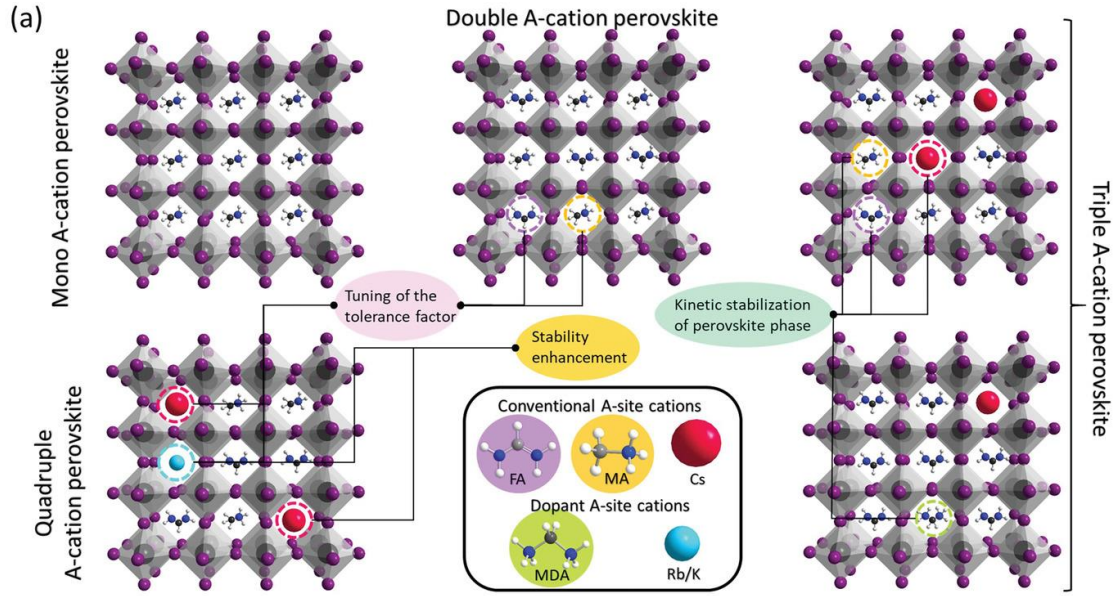

Figure 2.3. Schematic illustration of ABX_3 perovskite structure, as well as the full illustration of all possible multication combinations including single, double, triple, and quadruple components (reproduced from ref. 1 with permission).

In brief, introducing multication compositions with different ionic radii to occupy different positions in the perovskite crystals could modify the perovskite properties, leading to high-performance PSCs with record efficiency and stability. The increased stability is often attributed to the favorable tolerance factor for the perovskite phase upon A-site alloying (see Figure 2.3). It is well established that the A-site alloying improves the stability as well as reproducibility of PSCs. However, the relationship of chemical composition crystal structure-property-performance-phase stability is yet to be established[1,2,53-55].

2.1.4 Key parameters for perovskite film optimization.

Stoichiometry engineering

The dynamic stoichiometry of the A-site cation in the perovskite structure can improve the perovskite crystallinity and reduce the trap state density within the perovskite. Changing the A-site cation does not directly influence the electronic energy states at the band edge but has an indirect impact on the bandgap energy by changing the degree of octahedral distortions or inducing other structural changes.[4,13]

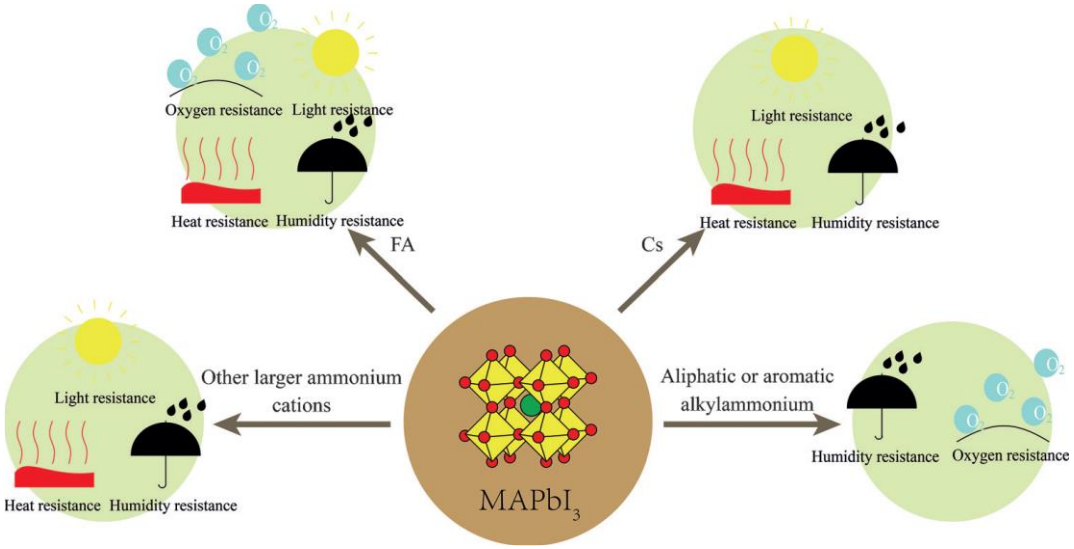

Figure 2.4. Effect of cations and their substitutions on the stability of perovskite materials (reproduced from ref. 2 with permission).

Engineering the composition of the A-site cation in the mixed-perovskite crystal is also one the most promising method to completely prevent, or at least slow the progression of, degradation as well as phase segregation in working perovskite solar cells and LEDs.[2,9,29,56] One explanation proposed is that the composition of the A-site cation is strongly linked to the crystallinity and quality of the resulting perovskite film, and therefore, as shown in the Figure 2.4, the choice of A-site cation has a large influence on a number of factors that could possibly be integral to perovskite crystallite size, trap state density, grain boundaries, halide vacancies, etc.

Crystallinity control

Metal halide perovskite films with higher crystallinity (i.e., films with a larger average crystal grain size) are more stable.[12,22-23] Analysis of comparable perovskite films, which are fabricated with a slight change in processing techniques has revealed a clear effect of crystalline quality on the tendency of the material quality (indicated by the width of X-ray diffraction peaks and the charge-carrier mobilities and lifetimes), leading to upgraded photostability in the perovskite absorber layer.[2,3,57]

Several pieces of evidence are reported in the literature that either directly or indirectly affecting factors of perovskite film crystallinity are being crucial in controlling optical stability. The exact reason why a larger grain size is related to the greater photostability of mixed perovskites remains a matter of discussion. Films with bigger crystal grains essentially have a lower grain boundary density, and several groups have reported low-bandgap domains forming around grain boundaries in perovskite films. The PL spectra measured from the grain centers were quite stable, showing that grain surfaces are integral to the charge transport process.[58] These discoveries propose that enhancement in the crystallinity of a perovskite film can reduce the density of the grain boundaries, which in turn may offer fewer nucleation points for the formation of non-radiative recombination regions or reduce the efficacy of the Auger charge recombination process.[59-61]

There are many factors why grain boundaries might induce photo instablity in mixed perovskites. The ionic motion has been reported to be specifically fast along grain boundaries in single-halide and multi-halide perovskites[2,4,25,62] which might be due to the fact that phase segregation is particularly effective at grain boundaries. Secondly, trap state density has also been related to instability.[63-66] Therefore, while the precise nature of trap states situated at grain boundaries remains debated, grain boundaries in the perovskite film may go along with ion migration by simply being locations that contain a high density of traps. However, it is important to notice that single crystals have surfaces that have been reported to be highly defective[27,67] and are usually extremely surface-sensitive. It is not surprising that there are few reports in the literature on the optical investigation in perovskite microplates and macro-sized crystals.

Charge-carrier extraction and injection and trap state passivation

There is now sufficient literature that suggests that excited charge carriers generated either from photo absorption or current injection are the operating elements responsible for

optical stability.[1,2,68] Perovskite photo instability can be reduced by influencing the charge-carrier density in the perovskite, e.g., by changing charge-carrier extraction or injection, or the recombination dynamics. Perovskite solar cells perhaps can be more efficient under working conditions when significant current extraction takes place than would be expected from simple photoluminescence measurements on corresponding perovskite films in the absence of charge-extraction layers. However, the incorporation of a trap passivation agent into a perovskite film usually alters other material properties too, like the nature of grain boundaries and also the ion migration channels, which is linked to photostability. In general, passivating agents represent an important methodology to manage photostability in perovskite materials, capable of reducing segregation on one side, e.g., by passivating trap states and potentially changing the ion migration pathways and mobilities. The drawback of using such passivating agents mostly stems from the challenges in finding appropriate agents and incorporating the agent into the perovskite film via an acceptable process methodology. And also, several additives produce side effects that can destroy the perovskite material properties – like charge-carrier transport across grain boundaries – leading to a spot in the concentration of the additive that has to be determined so as to optimize the optoelectronic performance of the perovskite.[2,8,69-72] The invention and fine-tuning of effective additives for the reduction of traps is therefore a direct, but complicated, target for the production of stable mixed perovskite solar cells and LEDs.

Many reports have recommended that the connection between trap passivation and optical instability stems from the charge carriers caught in localized trap states or at grain boundaries pushing the charge transportation.[2,4-6,73] To clarify these effects, it is proposed that electric fields produced by excited charge carriers caught in localized trap states or at grain boundaries in the perovskite are also the reason for the discovered charge movement and subsequent nonradiative recombination.[26], During this process, the electric field generated between holes funneled into the nascent low-bandgap area of the perovskite and the electrons trapped in the localized defect states then provide the driving force for ion transport. Similar concerns demonstrate the practicability to boost the phase stability of a mixed halide perovskite by simply changing the recombination dynamics into the radiative recombination regime, therefore reducing the fraction of charge carriers that are captured in trap states. In conclusion, photostability in mixed-ion perovskites can be changed through the tuning of charge-carrier recombination, extraction, and injection rates. Charge-carrier trapping is related to the non-radiative recombination process[2,3,74-77] possibly through the

electric fields these stationary charges generate. Therefore, a reduction in trap-mediated recombination through either extraction of charge carriers via an electrical circuit,[78] or trap passivation,[2,8] or by utilizing pulsed charge-carrier injection[2,9] is effective in decreasing the extent of optical instability.

Atmospheric effects

Atmospheric conditions are also expected to play an important role in stability mechanisms in mixed-ion perovskites. Varying atmospheric conditions such as changes in humidity or immersion of the perovskite into different gases are expected to affect the optical and structural properties. Environmental conditions alter the nature and distribution of trap states in metal halide perovskites. There is indeed enough confirmation in the literature for environmental effects on perovskite stability, and most of them are reliable but could be derived from variations in material morphology, composition, or experimental conditions between studies. Studies have not yet unanimously concluded on the impact of O_2 on optical stability, only covering minor changes in the speed of charge recombination in perovskite samples held under ambient air. Therefore, the impact of O_2 on photostability is continuously debated. The consequences of the environment in the photoluminescence properties of perovskite can be changed or delayed by coating the perovskite film with a thick encapsulant layer, like polymethyl methacrylate (PMMA). These encapsulant layers may in turn affect the comparability of measurements based on films in free space with those embedded in device structures.

Regulating illumination

The illumination falling upon a photovoltaic cell might vary noticeably depending on the placement of the solar cell in the world, the solar cell design, and other factors like implementation in a solar concentrator design[32] or tracking arrangements. Therefore, it is necessary to consider how the illumination will influence the optical stability of perovskite. An increase in the illumination intensity leads to faster charge carrier recombination in mixed perovskites.[9] In the condition that excited charge carriers are liable for photostability,[12,30,78] an increased illumination intensity photogenerates further excited charge carriers in the perovskite material per second, resulting in spontaneous recombination of charges. However, changes might not essentially be linear in the light

intensity, on condition that the efficiency with which absorbed photons induce trap may additionally modify with illumination intensity.

Solvent engineering

Solvent engineering using antisolvents plays an important role to improve perovskite film quality-related issues, such as rough surfaces, and pinholes (which result in poor device performance). Antisolvents, also known as non-solvents (to a particular solute), are fluids (liquid, vapor, or supercritical gas) that do not dissolve the solute but are homogenous with the solvent of the solution. When an antisolvent is added to a solution, it immediately reduces the solubility and creates local supersaturation conditions. As a result, precipitation, or crystallization occurs. This crystallization method is rapid and efficient. Additionally, being a room-temperature method, it is suitable for heat-sensitive materials. Therefore, it has extensive application in the production of micro- and nanoparticles,[79-81] inorganic materials,[56] polymers,[82-85] and recently in perovskite materials.[2,5,86-90] Using the diagram in Figure 2.5, we can understand the role of antisolvent in perovskite film formation.

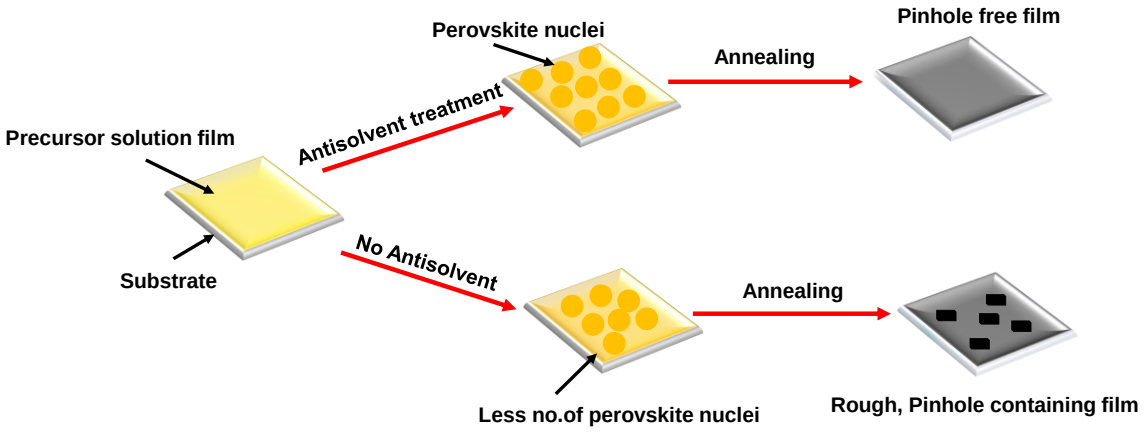

Figure 2.5. The antisolvent-assisted crystallization mechanism

According to literature, dripping toluene, chlorobenzene, diethyl ether, ethyl acetate, and isopropanol, etc. (as antisolvents) resulted in less pinholes and a smoother surface of perovskite film to improve the optoelectronic properties and reduced hysteresis.[1-6,9,91] It was speculated that the surface ions (halide and methylammonium) formed a complex with the solvent and had been removed during dripping antisolvent and this process had promoted a

net positive charge on the Pb atoms, which facilitated the formation of good quality perovskite film.[1-4,92-100] Antisolvent treatment increases the nucleus density during film formation to produce uniform and pinhole-free perovskite film, which facilitates improved solar cell efficiency, low hysteresis, and stability. Interestingly, many of the best-efficiency perovskite solar cells till date have been produced by the antisolvent treatment. Therefore, it is important to understand the fundamentals of antisolvent treatment, and various aspects of antisolvent application on perovskite film, for perovskite film quality improvement.

2.1.5 Structure of Perovskite Solar Cells

Although perovskites come from a seemingly different world of crystallography, they can be incorporated very easily into standard thin-film architecture. While the best perovskite structures have been vacuum deposited to give better, more uniform film qualities, this process requires the co-evaporation of the organic (methyl ammonium) component at the same time as the inorganic (lead/tin halide) components. The accurate co-evaporation of these materials to form the perovskite, therefore, requires specialist evaporation chambers that are not available to many researchers. This may also cause the practical issues of calibration and cross-contamination between organic and non-organic sources which would be difficult to clean.

The structure in Figure 2.6 represents a standard (non-inverted) perovskite solar cell based upon a standard glass/ITO substrate with metal back contact. All that is required to form a working device from the perovskite are two charge-selective interface layers for the electrons and holes respectively.

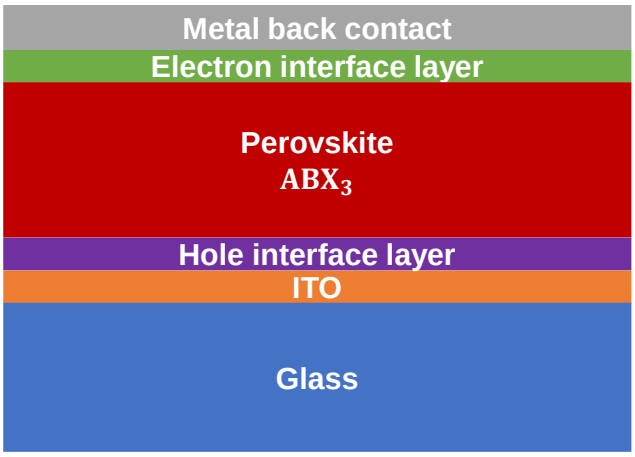

Figure 2.6. Generic device structure of a standard (non-inverted) perovskite solar cell.

Many of the standard interface layers from the world of organic photovoltaics work relatively well. For example PEDOT:PSS and the PTAA-class of polymers work well as hole interface layers while PCBM, C_{60}, ZnO and TiO_2 makes an effective electron interface. However, the field is so new that there is a vast archive of possible interface materials to be explored. Understanding and optimizing the energy levels and interactions of different materials at these interfaces offer a very exciting area of research[101-105].

The main issue for practical device fabrication of perovskite solar cells is that of film quality and thickness. The light-harvesting (active) perovskite layer needs to be several hundred nanometers thick for standard organic photovoltaics. Unless the deposition conditions and annealing temperature are optimized, rough surfaces with incomplete coverage are formed. Even with good optimization, there is still a significant surface roughness remaining, and therefore thicker interface layers than might normally be used are also required. However, the fact that spin coating can be used is highly encouraging because it has distinct advantages including significantly lower cost, and fewer problems involving scalability[1,2,8,106].

2.1.6 Introduction to Spin Coating

Spin coating is one of the most common techniques for applying thin films to substrates and is used in a wide variety of industries and technology sectors. The advantage of spin coating is its ability to produce very uniform films quickly and easily from a few nanometers to a few microns in thickness. The use of spin coating in organic electronics and nanotechnology is widespread and has built upon many of the techniques used in other semiconductor industries but also has some differences due to the relatively thin films, and high uniformity that are required for effective device preparation, as well as the need for self-assembly and organization to occur during the casting process.

The spin coating generally involves the fabrication of a thin film (a few nm to a few μm) evenly across the surface of a substrate by coating a solution of the desired material in a solvent (a "precursor") while it is rotating.

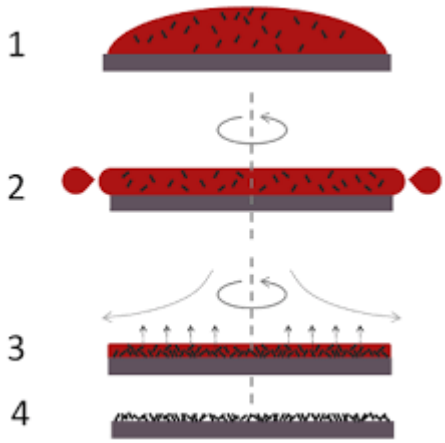

Figure 2.7. Example of spin coating a small molecule in solution using a static dispense (reproduced from ref. 96 with permission).

As shown in the Figure 2.7, the spin-coating process involves several steps:

- First the substrate is coated in the precursor containing the molecules dissolved in a solvent (1).
- Then the substrate is rotated at high speed and the excess precursor take off the side (2).
- Then airflow dries most of the solvent leaving a wet surface (3)
- before the film fully dries to just leave the molecules on the surface (4).

The rotation of the substrate at high speed (usually >10 rotations per second = 600 rpm) means that the centripetal force combined with the surface tension of the solution pulls the liquid coating into an even covering. During this time the solvent evaporates to leave the desired material on the substrate in an even covering. There are several important parameters for the spin coating which need optimization for the thin film fabrication, such as angular velocity (*w*), speed, time or concentration of solution.

In general, the thickness T of a spin-coated film is proportional to the inverse of the root of spin speed, as shown in the expression below, where *w* is the angular velocity:

$$T \propto \frac{1}{\sqrt{w}}$$

Another important factor is the speed of the spin coater. In general, the spin coating can produce uniform films relatively easily from about 1000 rpm, but with careful optimization of speed above 1000 rpm, a good film quality film can be achieved. Control of spin speed has both advantages and disadvantages. The disadvantage is that the range of thicknesses that can be achieved from a given solution is relatively narrow. On the other hand, the advantage is that it allows precise control of film thickness within this range. The thickness that can be produced from a given material/solvent combination further depends upon the concentration of the material in the precursor solution.

For most standard spin coating techniques, the objective is to keep the substrate spinning until the film is fully dry. As such this will mainly depend upon the boiling point and vapor pressure of the solvent that is used but also on the ambient conditions (temperature and humidity) that the spin coating performed in. For most alcoholic solvents a spin coating duration of 30 seconds is usually more than adequate and is therefore recommended as a starting point for most processes.[97,98]

2.2 Perovskite film preparation

2.2.1 Overview of the standard preparation process

The MA/FA based perovskite sample preparation process for the PL microscopic studies is summarized in the illustrative scheme below in Figure 2.8. There are several important parameters for the optimization of this basic process which we are discussing further in detail.

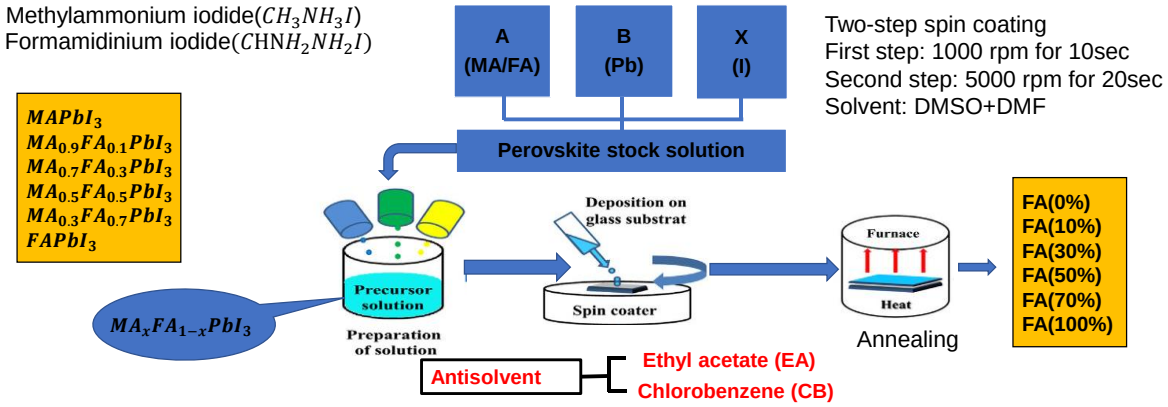

Figure 2.8. Sample preparation of MA-FA based halide perovskite

2.2.2 Perovskite precursor solution

The perovskite precursor solution preparation is simple. The stoichiometry[6,7] and the formation of coordination complexes[2,8,9] within perovskite precursors in solution largely impact the device performances and stability. Therefore, the preparation and the conditions of the perovskite precursor solution are very important steps that can affect the reproducibility of devices. In general, controlled preparation environment, such as using a nitrogen-filled glovebox (water and oxygen content below 1 ppm), anhydrous and high-purity solvents, and a calibrated balance and pipet, are recommended.

Here, on the other hand, we chose to prepare the sample under ambient environmental conditions because the ideal solar cell thin film should be stable in the environment. We prepare a precursor stock solution of 1.4 mol of $MA_xFA_{1-x}PbI_3$ per liter of

mixed solvent of 4:1 V/V dimethylformamide (DMF)/dimethyl sulfoxide (DMSO). For a 1.4 M $MAPbI_3$ stock solution we used 0.64 g of ground powder of PbI_2 and 0.22 g of MAI in 1 ml (800 µl + 200 µl) of the mixed solution of DMF and DMSO in a glass vial. The stock solution is then placed on a hot-plate magnetic starrier at room temperature and heated to 60°C for about 1 hour. Even then the solution was not clear and there were insoluble particles left in the bottom of the vial. We next changed the ratio of DMF and DMSO to 7:3 (instead of 4:1) and used (700 µl + 300 µl) of the mixed solvent to obtain a clear solution, as shown in Figure 2.9. The solution is then left to cool to room temperature and filtered using a pore size 0.45 µm syringe filter into another glass vial. The stock solutions prepared in this way can be stored for a long time; however, reheating to 60 °C is required each time.

Figure 2.9. precursor solution of $MA_xFA_{1-x}PbI_3$

2.2.3 Standard fabrication process of the perovskite films

$MA_xFA_{1-x}PbI_3$ perovskite films have been synthesized by the method reported before[1,4,98] with some modifications. A glass substrate has been cleaned with acetone, isopropanol, and deionized water. In the initial stage, we used the glass substrate directly to coat the perovskite layer. We were unable to obtain homogeneous films due to the hydrophobic nature of the glass surface which repelled the perovskite solution.

We next decided to use a layer of PEDOT:PSS because its surface is hydrophilic, and it is also easy to spin coat. PEDOT:PSS is also used in actual perovskite solar cells as the hole transporting layer (HTL). We fabricated a 40 nm thick layer of PEDOT:PSS (Clevios P AI4083, H. C. Starck) by spin-coating a water solution (at 4000 rpm for 40 s) on the glass substrates and annealing at 150 °C for 15 min. On top of that $MAPbI_3$ perovskite layer had been deposited. For that, 150 μL of 1.4 M precursor solution of $MAPbI_3$ (in 7:3 DMF:DMSO) was spin-coated on the substrates in two steps: at 1000 rpm for 10 s, followed by either 2000, 3000, 4000, or 5000 rpm for 30 s. In the last 10 s of the either 2000, 3000, 4000, or 5000 rpm spinning, 100 μL of chlorobenzene (CB) were dropped on the films as an antisolvent, followed by annealing.

2.3 Optimization of the sample preparation parameters

For the nanoscale scale study of the perovskite films, the standard film preparation procedure described above was further optimized with respect to annealing temperature, antisolvent deposition speed, concentration of precursor solution, choice of antisolvent, etc., to fabricate a stable, homogeneous and pinhole-free sample. All the optimization has been performed first on the $MAPbI_3$ sample.

2.3.1 Annealing temperature

The annealing temperature of perovskite films was varied from 90 °C to 120 °C with increment of 10 °C. Depending on the temperature the crystal growth was either very slow or very fast; low temperature leads to very small crystal size, on the other hand high annealing temperature causes the film to crack. At the temperature was at 100 °C the crystal

growth and film formation were improved considerably. In the following, the optimized annealing conditions of the annealing temperature of 100 °C and annealing time of 40 min were used for the perovskite film preparation.

2.3.2 Spin-coating speed and antisolvent deposition

After the first attempt at fabrication of all $MAPbI_3$ samples with optimized precursor solution and annealing temperature we realized that the crystal formation and film quality were better for higher rpm speed of the second spin-coating step. The results for the 2000, 3000, 4000, and 5000 rpm spin-coating speeds are shown in the SEM images in the Figure 2.10. The best quality film was obtained with 5000 rpm and this value was used as optimized spin-coating speed further on.

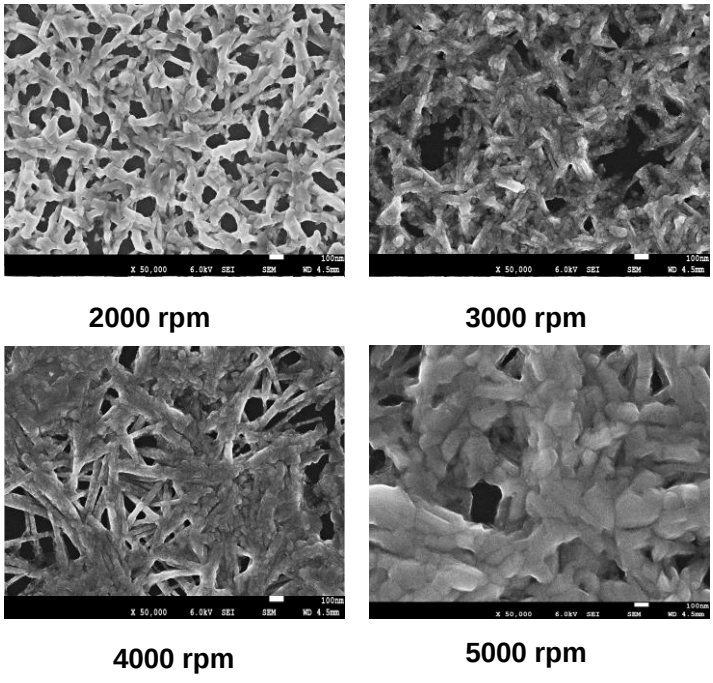

Figure 2.10. $MAPbI_3$ sample prepared on different spin coating speed.

As we can also see in the SEM images in Figure 2.10, the surface area coverage is still not uniform, which might be because the technique of dropping the antisolvent was not correct. In the next step, we optimized the deposition time of antisolvent by choosing different pipette tips and adjusting their diameters. As shown in Figure 2.11, we used four different tips as well as an injection syringe. The deposition times of the antisolvent for tip 1, tip 2, the injection syringe, tip 3 and tip 4 range between 0.6 s and << 0.1 s. After comparing the resulting SEM images (Figure 2.12), the optimal deposition time of 0.1 s (tip 4) was selected and used in the film preparation further on.

Figure 2.11. Different tips for optimization of antisolvent time

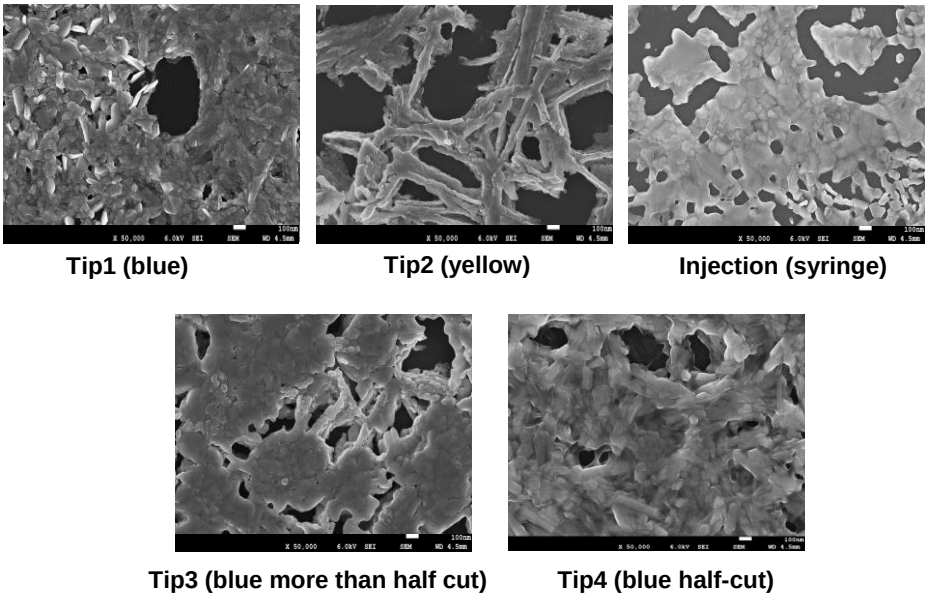

Figure 2.12. SEM images corresponding to different tips.

In addition to the SEM images, the use of tip 1, tip 2, tip 3 and the injection syringe also leads to wet films that were not transparent, showing unwanted cloud-like structures in the middle.

2.3.3 Concentration of the precursor solution

While optimizing the spin-coating conditions lead to improved film quality, there are still many big pinholes visible in the SEM images. The following optimization was carried out on the whole series of $MA_xFA_{1-x}PbI_3$ perovskite films. The 1.4 M $MA_xFA_{1-x}PbI_3$ perovskite precursor solutions were prepared by mixing PbI_2 with MAI and FAI (formamidinium iodide) with molar ratios of 1:1:0, 1:0.9:0.1, 1:0.7:0.3, 1:0.5:0.5, 1:0.3:0.7 and 1:0:1, respectively, in 1 ml of the mixed solvent mix of DMSO (30%) and DMF (70%) by vigorous stirring at 60 °C. The precursor solutions were spin-coated on the substrates and annealed as described above. The SEM images of all the composition films are shown in Figure 2.13. As the images show, the precursor concentration of 1.4 M (used originally in ref. 43) leads to larger grain size, large numbers of pinholes, more roughness, and overall larger morphological nonuniformity.

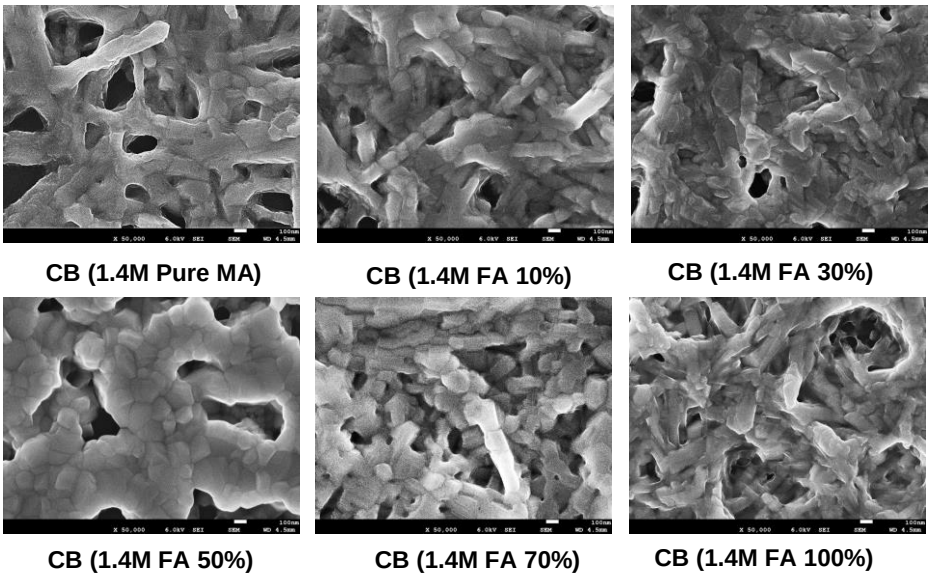

Figure 2.13. SEM images of $MA_xFA_{1-x}PbI_3$ for 1.4M precursor solution

In the next step, we have decreased the precursor concentration to 1.0 M from the original 1.4 M. The 1.0 M $MA_xFA_{1-x}PbI_3$ perovskite precursor solutions were prepared accordingly by measuring the accurate weight of MAI, FAI and PbI_2 given in Table 2.1.

$MA_xFA_{1-x}PbI_3$	MAI (g)	FAI (g)	PbI_2 (g)
$MAPbI_3$ (Pure MA)	0.16	0	0.46
$MA_{0.9}FA_{0.1}PbI_3$ (FA 10%)	0.144	0.0172	0.46
$MA_{0.7}FA_{0.3}PbI_3$ (FA 30%)	0.112	0.0516	0.46
$MA_{0.5}FA_{0.5}PbI_3$ (FA 50%)	0.08	0.086	0.46
$MA_{0.3}FA_{0.7}PbI_3$ (FA 70%)	0.048	0.1204	0.46
$FAPbI_3$ (FA 100%)	0	0.172	0.46

Table 2.1. Solute quantity for $MA_xFA_{1-x}PbI_3$ for 1.0 M perovskite precursor solutions

The SEM images of all the composition films prepared with the 1.0 M precursor concentration are shown in Figure 2.14. Compared to the 1.4 M concentration the films look overall better. Even though the crystal grains are smaller the films are more homogeneous with far less pinholes.

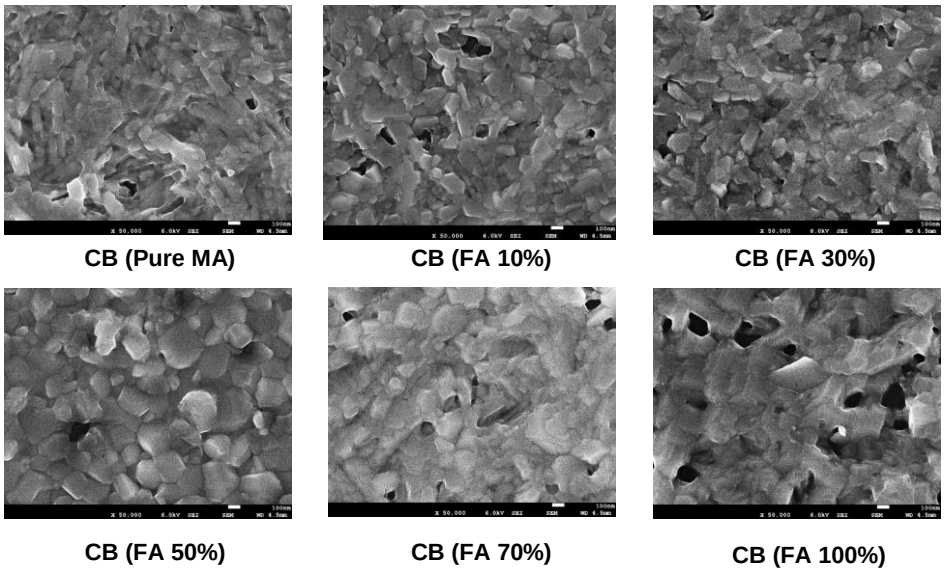

Figure 2.14. SEM images of $MA_xFA_{1-x}PbI_3$ for 1.0 M precursor solution

2.3.4 Choice of antisolvent

In an attempt to further improve the film quality, we used several different antisolvents, such as isopropyl alcohol (IPA), toluene, diethyl ether, and ethyl acetate, and compared their effect on the films structure with that of chlorobenzene. The basic parameters of the antisolvents, such as polarity and boiling points, are shown in Table 2.2

Antisolvent	Boiling point (ºC)	Dipole moment (D)
Isopropyl alcohol (IPA)	82.6	1.58
Toluene	111	0.38
Diethyl ether	34.6	1.15
Chlorobenzene	131	1.69
Ethyl acetate	77.1	1.78

Table 2.2. Boiling point and dipole moment of commonly used antisolvent in perovskite

The films were prepared by the optimized procedure described above. The SEM images of the $MA_{0.5}FA_{0.5}PbI_3$ (FA 50%) films prepared with IPA, toluene and diethyl ether are shown in Figure 2.15. The SEM images for the whole series of the film compositions prepared using the ethyl acetate antisolvent are shown in Figure 2.16.

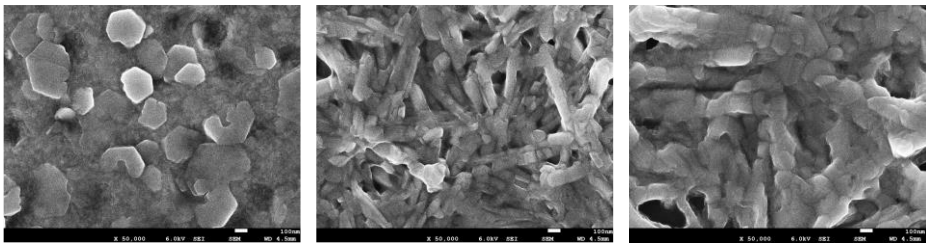

IPA (FA 50% 1M) **Toluene (FA 50% 1M)** **Ether (FA 50% 1M)**

Figure 2.15. SEM images of $MA_{0.5}FA_{0.5}PbI_3$ (FA 50%) films prepared with IPA, toluene and diethyl ether

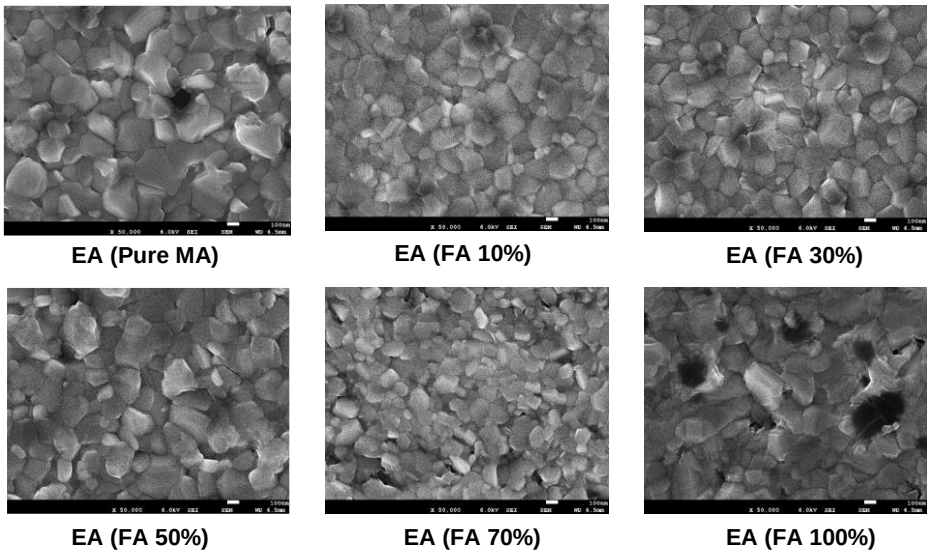

Figure 2.16. SEM images for the whole series of the film compositions prepared using the ethyl acetate antisolvent

As we can see in the above SEM images, ethyl acetate is the most promising antisolvent of all the solvents used. The crystal formation is very uniform, the grain size distribution is smallest and the surface area is fully covered. Also, we can clearly see that there are very few pinholes in each sample. As ethyl acetate dissolves a considerably higher amount of water than other studied antisolvents, it could dissolve the moisture in the air more efficiently during spin coating to preclude any reaction between moisture and perovskite materials even at relatively humid conditions. Also, the low dipole moment of the antisolvent (such as toluene) leads to intermediate phase formation (with DMSO) that produces larger grains. But moderate dipole moment of the antisolvent (such as chlorobenzene) leads to direct crystallization that produces smaller grains. Larger grains sometimes can have gaps in between them and smaller grains have more grain boundaries. From that point of view, ethyl acetate is one of the promising antisolvents for perovskite film fabrication.

2.4 Conclusions

In this Chapter, we have given the point of view toward the morphology optimization of the perovskite absorber layer and compositional development of halide perovskites towards homogeneous and long-term stable organic–inorganic hybrid perovskite films. We discussed the impact of annealing temperature, precursor solution engineering, spin coating parameters, the addition of antisolvent, compositional engineering, and solvent engineering on the optimization of morphology and material properties of perovskites towards the highly efficient and stable thin film. The effect of all these optimization treatments directly impacts the grain sizes. Hybrid perovskites with larger grain sizes and fewer pinholes have been produced, potentially reducing charge non-radiative recombination.[107]

2.5 References

1. Byranvand, M. M.; Otero-Martínez, C.; Ye, J.; Zuo, W.; Manna, L.; Saliba, M.; Hoye, R. L. Z.; Polavarapu, L. Recent Progress in Mixed A-Site Cation Halide Perovskite Thin-Films and Nanocrystals for Solar Cells and Light-Emitting Diodes. Adv. Optical Mater. **2022**, 10, 2200423.
2. Wang, Z.; Shi, Z.; Li, T.; Chen, Y.; Huang, W. Stability of Perovskite Solar Cells: A Prospective on the Substitution of the A Cation and X Anion. Angew. Chem., Int. Ed. **2017**, 56, 1190−1212
3. Ghosh, S.; Mishra, S.; Singh, T. Antisolvents in Perovskite Solar Cells: Importance, Issues, and Alternatives. Adv. Mater. Interfaces **2020**, 7, 2000950.
4. Kim, B.; Kim, J.; Park, N. First-principles identification of the charge-shifting mechanism and ferroelectricity in hybrid halide perovskites. Sci Rep **2020** 10, 19635.
5. Li, G.; Wang, Y.; Huang, L.; Sun, W. Research Progress of High Sensitivity Perovskite Photodetectors: A Review of Photodetectors: Noise, Structure, and Materials. ACS Appl. Electron. Mater. **2022**, 4, 1485−1505.
6. Li, Y.-T.; Han, L.; Liu, H.; Sun, K.; Luo, D.; Guo, X.-L.; Yu, D.- L.; Ren, T.-L. Review on organic−inorganic two-dimensional perovskite-based optoelectronic devices. ACS Appl. Electron. Mater. **2022**, 4, 547.
7. Dey, A.; Ye, J.; De, A.; Debroye, E.; Ha, S. K.; Bladt, E.; Kshirsagar, A. S.; Wang, Z.; Yin, J.; Wang, Y.; et al. State of the Art and Prospects for Halide Perovskite Nanocrystals. ACS Nano **2021**, 15, 10775−10981.
8. Cohen, B. El; Aharon, S.; Dymshits, A.; Etgar, L. Impact of Antisolvent Treatment on Carrier Density in Efficient Hole-Conductor-Free Perovskite-Based Solar Cells. J. Phys. Chem. C **2016**,120,142.
9. Brenner, T. M.; Egger, D. A.; Kronik, L.; Hodes, G.; Cahen, D. Hybrid Organic−Inorganic Perovskites: Low-Cost Semiconductors with Intriguing Charge-Transport Properties. Nat. Rev. Mater. **2016**, 1, 15007.
10. Mozur, E.M.; A. E. Maughan, Y. Cheng, A. Huq, N. Jalarvo, L. L. Daemen, J. R. Neilson. Orientational Glass Formation in Substituted Hybrid Perovskites. Chem. Mater. **2017**, 29, 10168.
11. Goldschmidt, V. M. Die Gesetze Der Krystallochemie (The Laws of Cristallochemistry). Naturwissenschaften **1926**, 14, 477−485.

12. Kieslich, G.; Sun, S.; Cheetham, A. K. Solid-State Principles Applied to Organic-Inorganic Perovskites: New Tricks for an Old Dog. Chem. Sci. **2014**, 5, 4712−4715.
13. Pavlovetc, I. M.; Brennan, M. C.; Draguta, S.; Ruth, A.; Moot, T.; Christians, J. A.; Aleshire, K.; Harvey, S. P.; Toso, S.; Nanayakkara, S. U.; et al. Suppressing cation migration in triplecation lead halide perovskites. ACS Energy Letters **2020**, 5, 2802−2810.
14. Domanski, K.; Roose, B.; Matsui, T.; Saliba, M.; Turren-Cruz, S.-H.; Correa-Baena, J.-P.; Carmona, C. R.; Richardson, G.; Foster, J. M.; De Angelis, F.; Ball, J. M.; Petrozza, A.; Mine, N.; Nazeeruddin, M. K.; Tress, W.; Grätzel, M.; Steiner, U.; Hagfeldt, A.; Abate, A. Migration of Cations Induces Reversible Performance Losses over Day/night Cycling in Perovskite Solar Cells. Energy Environ. Sci. **2017**, 10, 604−613.
15. Kwon, K. C.; Hong, K.; Van Le, Q.; Lee, S. Y.; Choi, J.; Kim, K.-B.; Kim, S. Y.; Jang, H. W. Inhibition of Ion Migration for Reliable Operation of Organolead Halide Perovskite-Based Metal/Semiconductor/Metal Broadband Photodetectors. Adv. Funct. Mater. **2016**, 26, 4213−4222.
16. Khenkin, M. V.; Katz, E. A.; Abate, A.; Bardizza, G.; Berry, J. J.; Brabec, C.; Brunetti, F.; Bulovic,́ V.; Burlingame, Q.; Di Carlo, A.; Cheacharoen, R.; Cheng, Y.-B.; Colsmann, A.; Cros, S.; Domanski, K.; Dusza, M.; Fell, C. J.; Forrest, S. R.; Galagan, Y.; Di Girolamo, D.; Grätzel, M.; Hagfeldt, A.; von Hauff, E.; Hoppe, H.; Kettle, J.; Köbler, H.; Leite, M. S.; Liu, S.; Loo, Y.-L.; Luther, J. M.; Ma, C.-Q.; Madsen, M.; Manceau, M.; Matheron, M.; McGehee, M.; Meitzner, R.; Nazeeruddin, M. K.; Nogueira, A. F.; Odabası̧, Ç.; Osherov, A.; Park, N.-G.; Reese, M. O.; De Rossi, F.; Saliba, M.; Schubert, U. S.; Snaith, H. J.; Stranks, S. D.; Tress, W.; Troshin, P. A.; Turkovic, V.; Veenstra, S.; Visoly-Fisher, I.; Walsh, A.; Watson, T.; Xie, H.; Yıldırım, R.; Zakeeruddin, S. M.; Zhu, K.; Lira-Cantu, M. Consensus statement for stability assessment and reporting for perovskite photovoltaics based on ISOS procedures. Nat. Energy **2020**, 5, 35−49.
17. Chen, J.; Messing, M. E.; Zheng, K.; Pullerits, T. Cation Dependent Hot Carrier Cooling in Halide Perovskite Nanocrystals. J. Am. Chem. Soc. **2019**, 141 (8), 3532−3540.
18. Lee, M. M.; Teuscher, J.; Miyasaka, T.; Murakami, T. N.; Snaith, H. J. Efficient Hybrid Solar Cells Based on Meso-Superstructured Organometal Halide Perovskites. Science **2012**, 338 (6107), 643−647.

19. Stranks, S. D.; Eperon, G. E.; Grancini, G.; Menelaou, C.; Alcocer, M. J.; Leijtens, T.; Herz, L. M.; Petrozza, A.; Snaith, H. J. Electron-hole diffusion lengths exceeding 1 micrometer in an organometal trihalide perovskite absorber. Science **2013**, 342, 341−344.
20. Xing, G.; Mathews, N.; Sun, S.; Lim, S.; Lam, Y.; Grätzel, M.; Mhaisalkar, S.; Sum, T. Long-Range Balanced Electron- and Hole Transport Lengths in Organic-Inorganic $CH_3NH_3PbI_3$. Science **2013**, 342, 344−347.
21. D'Innocenzo, V.; Grancini, G., Alcocer; M. et al. Excitons versus free charges in organo-lead tri-halide perovskites. Nat Commun **2014**, 5, 3586.
22. Yoo, J.J.; Seo, G.; Chua, M.R. et al. Efficient perovskite solar cells via improved carrier management. Nature **2021**, 590, 587–593.
23. Jacobsson, T. J.; Correa-Baena, J.-P.; Pazoki, M.; Saliba, M.; Schenk, K.; Gratzel, M.; Hagfeldt, A. Exploration of the Compositional Space for Mixed Lead Halogen Perovskites for High Efficiency Solar cells. Energy Environ. Sci. **2016**, 9, 1706−1724.
24. Saliba, M.; Matsui, T.; Domanski, K.; Seo, J. Y.; Ummadisingu, A.; Zakeeruddin, S. M.; Correa-Baena, J. P.; Tress, W. R.; Abate, A.; Hagfeldt, A.; Grätzel, M. Incorporation of Rubidium Cations into Perovskite Solar Cells Improves Photovoltaic Performance. Science **2016**, 354, 206−209.
25. Saliba, M.; Matsui, T.; Seo, J.-Y.; Domanski, K.; Correa-Baena, J.- P.; Nazeeruddin, M. K.; Zakeeruddin, S. M.; Tress, W.; Abate, A.; Hagfeldt, A.; Grätzel, M. Cesium-containing triple cation perovskite solar cells: improved stability, reproducibility and high efficiency. Energy Environ. Sci. **2016**, 9 (6), 1989−1997.
26. Johnsson, M.; Lemmens, P. Crystallography and Chemistry of Perovskites J. Phys.: Condens. Matter **2008**, 20, 264001.
27. Ü nlü, F.; Jung, E.; Haddad, J.; Kulkarni, A.; Ö z, S.; Choi, H.; Fischer, T.; Chakraborty, S.; Kirchartz, T.; Mathur, S. Understanding the Interplay of Stability and Efficiency in A-Site Engineered Lead Halide Perovskites. APL Mater. **2020**, 8, No. 070901.
28. Satapathi, S. Halide Perovskites in India. ACS Energy Lett. **2022**, 7, 906−907.
29. Li, Z.; Yang, M.; Park, J.-S.; Wei, S.-H.; Berry, J. J.; Zhu, K. Stabilizing Perovskite Structures by Tuning Tolerance Factor: Formation of Formamidinium and Cesium Lead Iodide Solid-State Alloys. Chem. Mater. **2016**, 28, 284−292.
30. Green, M.; Ho-Baillie, A.; Snaith, H. The emergence of perovskite solar cells. Nature Photon **2014**, 8, 506–514.

31. Umebayashi, T.; Asai, K.; Kondo, T.; Nakao, A. Electronic Structures of Lead Iodide Based Low-Dimensional Crystals. Phys. Rev. B: Condens. Matter Mater. Phys. **2003**, 67, 155405.
32. Lee, J.-W.; Tan, S.; Seok, S. I.; Yang, Y.; Park, N.-G. Rethinking the A cation in halide perovskites. Science **2022**, 375, No. eabj1186.
33. Ono, L. K.; Juarez-Perez, E. J.; Qi, Y. B. Progress on Perovskite Materials and Solar Cells with Mixed Cations and Halide Anions. ACS Appl. Mater. Interfaces **2017**, 9 (36), 30197−30246.
34. Jeon, N.; Noh, J.; Yang, W. et al. Compositional engineering of perovskite materials for high-performance solar cells. Nature **2015**, 517, 476–480.
35. Saliba, M. Polyelemental, Multicomponent Perovskite Semiconductor Libraries through Combinatorial Screening. Adv. Energy Mater. **2019**, 9, No. 1803754.
36. Ghosh, D.; Acharya, D.; Zhou, L.; Nie, W.; Prezhdo, O. V.; Tretiak, S.; Neukirch, A. J. Lattice Expansion in Hybrid Perovskites: Effect on Optoelectronic Properties and Charge Carrier Dynamics. J. Phys. Chem. Lett. **2019**, 10 (17), 5000−5007.
37. Lee, J. W.; Seol, D. J.; Cho, A. N.; Park, N. High-efficiency perovskite solar cells based on the black polymorph of HC- $(NH_2)_2PbI_3$. Adv. Mater. **2014**, 26, 4991−4998.
38. Leyden, M. R.; Lee, M. V.; Raga, S. R.; Qi, Y. Large Formamidinium Lead Trihalide Perovskite Solar Cells Using Chemical Vapor Deposition with High Reproducibility and Tunable Chlorine Concentrations. J. Mater. Chem. A **2015**, 3, 16097−16103.
39. Bi, D.; Gao, P.; Scopelliti, R.; Oveisi, E.; Luo, J.; Grätzel, M.; Hagfeldt, A.; Nazeeruddin, M. K. High-Performance Perovskite Solar Cells with Enhanced Environmental Stability Based on Amphiphile Modified $CH_3NH_3PbI_3$. Adv. Mater. **2016**, 28, 2910−2915.
40. Zhao, Y.; Zhu, K. Organic−Inorganic Hybrid Lead Halide Perovskites for Optoelectronic and Electronic Applications. Chem. Soc. Rev. **2016**, 45, 655−689.
41. Pellet, N.; Gao, P.; Gregori, G.; Yang, T. Y.; Nazeeruddin, M. K.; Maier, J.; Gratzel, M. Mixed-Organic-Cation Perovskite Photovoltaics for Enhanced Solar-Light Harvesting. Angew. Chem., Int. Ed. **2014**, 53, 3151−3157.
42. Assadi, M. K.; Hanaei, H.; Mohamed, N. M.; Saidur, R.; Bakhoda, S.; Bashiri, R.; Moayedfar, M. Enhancing the efficiency of luminescent solar concentrators (LSCs). Appl. Phys. A: Mater. Sci. Process. **2016**, 122 (9), 821.
43. Saliba, M.; Orlandi, S.; Matsui, T. et al. A molecularly engineered hole-transporting material for efficient perovskite solar cells. Nat Energy **2016**, 1, 15017.

44. Saliba, M.; Correa-Baena, J. P.; Wolff, C. M.; Stolterfoht, M.; Phung, N.; Albrecht, S.; Neher, D.; Abate, A. How to Make over 20% Efficient Perovskite Solar Cells in Regular (n-i-p) and Inverted (p-i-n) Architectures. Chem. Mater. **2018**, 30 (13), 4193−4201.
45. Ye, J.; Byranvand, M. M.; Martínez, C. O.; Hoye, R. L. Z.; Saliba, M.; Polavarapu, L. Defect Passivation in Lead-Halide Perovskite Nanocrystals and Thin Films: Toward Efficient LEDs and Solar Cells. Angew. Chem., Int. Ed. **2021**, 60, 21636.
46. Hazarika, A.; Zhao, Q.; Gaulding, E. A.; Christians, J. A.; Dou, B.; Marshall, A. R.; Moot, T.; Berry, J. J.; Johnson, J. C.; Luther, J. M. Perovskite Quantum Dot Photovoltaic Materials beyond the Reach of Thin Films: Full-Range Tuning of A-Site Cation Composition. ACS Nano **2018**, 12, 10327−10337.
47. Protesescu, L.; Yakunin, S.; Kumar, S.; Bär, J.; Bertolotti, F.; Masciocchi, N.; Guagliardi, A.; Grotevent, M.; Shorubalko, I.; Bodnarchuk, M. I.; Shih, C.-J.; Kovalenko, M. V. Dismantling the "Red Wall" of Colloidal Perovskites: Highly Luminescent Formamidinium and Formamidinium−Cesium Lead Iodide Nanocrystals. ACS Nano **2017**, 11, 3119−3134.
48. Vigil, J. A.; Hazarika, A.; Luther, J. M.; Toney, M. F. $FA_xCs_{1-x}PbI_3$ Nanocrystals: Tuning Crystal Symmetry by A-Site Cation Composition. ACS Energy Lett. **2020**, 5, 2475.
49. Hao, M.; Bai, Y.; Zeiske, S. et al. Ligand-assisted cation-exchange engineering for high-efficiency colloidal $Cs_{1-x}FA_xPbI_3$ quantum dot solar cells with reduced phase segregation. Nat. Energy **2020**, 5, 79.
50. Tian, J.; Wang, J.; Xue, Q.; Niu, T.; Yan, L.; Zhu, Z.; Li, N.; Brabec, C. J.; Yip, H.-L.; Cao, Y. Composition Engineering of All Inorganic Perovskite Film for Efficient and Operationally Stable Solar Cells. Adv. Funct. Mater. **2020**, 30, 2001764.
51. Quintana, M. A.; King, D. L.; Hosking, F. M.; Kratochvil, J. A.; Johnson, R. W.; Hansen, B. R.; Dhere, N. G.; Pandit, M. B. Diagnostic Analysis of Silicon Photovoltaic Modules after 20-Year Field Exposure. Presented at the 28th IEEE Photovoltaic Specialists Conference; Anchorage, Alaska, September 15−22, **2000**; pp 1420− 1423.
52. Grancini, G.; Roldán-Carmona, C.; Zimmermann, I.; Mosconi, E.; Lee, X.; Martineau, D.; Narbey, S.; Oswald, F.; De Angelis, F.; Graetzel, M.; Nazeeruddin, M. K. One-Year stable perovskite solar cells by 2D/3D interface engineering. Nat. Commun. **2017**, 8, 15684.

53. Bakulin, A. A.; Selig, O.; Bakker, H. J.; Rezus, Y. L. A.; M uller, C.; Glaser, T.; Lovrincic, R.; Sun, Z.; Chen, Z.; Walsh, A.; Frost, J. M.; Jansen, T. L. C. Real-Time Observation of Organic Cation Reorientation in Methylammonium Lead Iodide Perovskites. J. Phys. Chem. Lett. **2015**, 6, 3663−3669.
54. Miyasaka, T. Perovskite Photovoltaics: Rare Functions of Organo Lead Halide in Solar Cells and Optoelectronic Devices. Chem. Lett. **2015**, 44, 720−729.
55. Singh, T.; Kulkarni, A.; Ikegami, M.; Miyasaka, T. Effect of Electron Transporting Layer on Bismuth-Based Lead-Free Perovskite $(CH_3NH_3)_3Bi_2I_9$ for Photovoltaic Applications. ACS Appl. Mater. Interfaces **2016**, 8, 14542−14547.
56. Jena, A. K.; Kulkarni, A.; Miyasaka, T. Halide Perovskite Photovoltaics: Background, Status, and Future Prospects. Chem. Rev. **2019**, 119, 3036−3103.
57. Champion Photovoltaic Module Efficiency Chart | Photovoltaic Research | NREL. https://www.nrel.gov/pv/module-efficiency.html (accessed September 15, **2022**).
58. Yen, H. J.; Liang, P. W.; Chueh, C. C.; Yang, Z.; Jen, A. K. Y.; Wang, H. L. Large Grained Perovskite Solar Cells Derived from Single Crystal Perovskite Powders with Enhanced Ambient Stability. ACS Appl. Mater. Interfaces **2016**, 8 (23), 14513−14520.
59. Turren-Cruz, S.-H.; Hagfeldt, A.; Saliba, M. Methyl ammonium Free, High-Performance, and Stable Perovskite Solar Cells on a Planar Architecture. Science. **2018**, 362 (6413), 449−453.
60. Schmidt-Mende, L.; Dyakonov, V.; Olthof, S.; Unlu, F.; Le, K. M. T.; Mathur, S.; Karabanov, A. D.; Lupascu, D. C.; Herz, L. M.; Hinderhofer, A.; Schreiber, F.; Chernikov, A.; Egger, D. A.; Shargaieva, O.; Cocchi, C.; Unger, E.; Saliba, M.; Byranvand, M. M.; Kroll, M.; Nehm, F.; Leo, K.; Redinger, A.; Hocker, J.; Kirchartz, T.; Warby, J.; Gutierrez-Partida, E.; Neher, D.; Stolterfoht, M.; Wurfel, U.; Unmussig, M.; Herterich, J.; Baretzky, C.; Mohanraj, J.; Thelakkat, M.; Maheu, C.; Jaegermann, W.; Mayer, T.; Rieger, J.; Fauster, T.; Niesner, D.; Yang, F.; Albrecht, S.; Riedl, T.; Fakharuddin, A.; Vasilopoulou, M.; Vaynzof, Y.; Moia, D.; Maier, J.; Franckevicius, M.; Gulbinas, V.; Kerner, R. A.; Zhao, L.; Rand, B. P.; Gluck, N.; Bein, T.; Matteocci, F.; Castriotta, L. A.; Di Carlo, A.; Scheffler, M.; Draxl, C. Roadmap on Organic − Inorganic Hybrid Perovskite Semiconductors and Devices. APL Mater. **2021**, 9, 109202.
61. Ma, S.; Yuan, G.; Zhang, Y.; Yang, N.; Li, Y.; Chen, Q. Development of encapsulation strategies towards the commercialization of perovskite solar cells. Energy Environ. Sci. **2022**, 15, 13−55.

62. Technology Readiness Level. https://www.nasa.gov/ directorates/heo/scan/engineering/technology/technology_ readiness_level (accessed September 15, **2022**)
63. Byranvand, M. M.; Saliba, M. Defect Passivation of Perovskite Films for Highly Efficient and Stable Solar Cells. Sol. RRL **2021**, 5, 2100295.
64. Liu, S.; Guo, R.; Xie, F. The effects of organic cation rotation in hybrid Organic-Inorganic Perovskites: A critical review. Mater. Des. **2022**, 221, 110951.
65. Akkerman, Q. A.; D'Innocenzo, V.; Accornero, S.; Scarpellini, A.; Petrozza, A.; Prato, M.; Manna, L. Tuning the Optical Properties of Cesium Lead Halide Perovskite Nanocrystals by Anion Exchange Reactions. J. Am. Chem. Soc. **2015**, 137, 10276−10281.
66. Zhizhchenko, A. Y.; Tonkaev, P.; Gets, D.; Larin, A.; Zuev, D.; Starikov, S.; Pustovalov, E. V.; Zakharenko, A. M.; Kulinich, S. A.; Juodkazis, S.; Kuchmizhak, A. A.; Makarov, S. V. Light-Emitting Nanophotonic Designs Enabled by Ultrafast Laser Processing of Halide Perovskites. Small **2020**, 16 (19), 2000410.
67. Kim, G.; Min, H.; Lee, K. S.; Lee, D. Y.; Yoon, S. M.; Seok, S. I. Impact of Strain Relaxation on Performance of α-Formamidinium Lead Iodide Perovskite Solar Cells. Science **2020**, 370 (6512), 108− 112.
68. Kubicki, D. J.; Prochowicz, D.; Hofstetter, A.; Zakeeruddin, S. M.; Grätzel, M.; Emsley, L. Phase Segregation in Cs-, Rb- and K Doped Mixed-Cation $(MA)_x(FA)_{1-x}PbI_3$ Hybrid Perovskites from Solid-State NMR. J. Am. Chem. Soc. **2017**, 139, 14173−14180.
69. Knight, A. J.; Borchert, J.; Oliver, R. D. J.; Patel, J. B.; Radaelli, P. G.; Snaith, H. J.; Johnston, M. B.; Herz, L. M. Halide Segregation in Mixed-Halide Perovskites: Influence of a-Site Cations. ACS Energy Lett. **2021**, 6, 799−808.
70. Dedecker, K.; Grancini, G. Dealing with Lead in Hybrid Perovskite: A Challenge to Tackle for a Bright Future of This Technology? Adv. Energy Mater. **2020**, 10, 2001471.
71. Lee, J. W.; Kim, S. G.; Yang, J. M.; Yang, Y.; Park, N. G. Verification and Mitigation of Ion Migration in Perovskite Solar Cells. APL Mater. **2019**, 7, No. 041111.
72. Zhang, S.; Tang, M.-C.; Fan, Y.; Li, R.; Nguyen, N. V.; Zhao, K.; Anthopoulos, T. D.; Hacker, C. A. Role of Alkali-Metal Cations in Electronic Structure and Halide Segregation of Hybrid Perovskites. ACS Appl. Mater. Interfaces **2020**, 12, 34402−34412.

73. Future of Photovoltaic; International Renewable Energy Agency, **2019**. https://www.irena.org/-/media/Files/IRENA/Agency/ Publication/2019/Nov/IRENA_Future_of_Solar_PV_**2019**.pdf.
74. Best Research-Cell Efficiency Chart | Photovoltaic Research | NREL. https://www.nrel.gov/pv/cell-efficiency.html (accessed September 15, **2022**).
75. Lin, Y.; Chen, B.; Fang, Y. et al. Excess charge-carrier induced instability of hybrid perovskites. Nat. Commun. **2018**, 9, 4981.
76. Cao, J.; Tao, S. X.; Bobbert, P. A.; Wong, C.-P.; Zhao, N. Interstitial Occupancy by Extrinsic Alkali Cations in Perovskites and Its Impact on Ion Migration. Adv. Mater. **2018**, 30, 1707350.
77. Nakanishi, E.; Nishikubo, R.; Wakamiya, A.; Saeki, A. How the Mixed Cations (Guanidium, Formamidinium, and Phenylethylamine) in Tin Iodide Perovskites Affect Their Charge Carrier Dynamics and Solar Cell Characteristics. J. Phys. Chem. Lett. **2020**, 11, 4043−4051.
78. Skoczek, A.; Sample, T.; Dunlop, E. D. The results of performance measurements of field-aged crystalline silicon photovoltaic modules. Prog. Photovoltaics Res. Appl. **2009**, 17, 227−240.
79. Feldmann, S.; Macpherson, S.; Senanayak, S.P. et al. Photodoping through local charge carrier accumulation in alloyed hybrid perovskites for highly efficient luminescence. Nat. Photonics **2020**, 14, 123.
80. Ravi, V. K.; Mondal, B.; Nawale, V. V.; Nag, A. Don't Let the Lead Out: New Material Chemistry Approaches for Sustainable Lead Halide Perovskite Solar Cells. ACS Omega **2020**, 5, 29631−29641.
81. Lim, J. W. M.; Giovanni, D.; Righetto, M.; Feng, M.; Mhaisalkar, S. G.; Mathews, N.; Sum, T. C. Hot Carriers in Halide Perovskites: How Hot Truly? J. Phys. Chem. Lett. **2020**, 11, 2743− 2750.
82. Saidaminov, M. I.; Williams, K.; Wei, M.; Johnston, A.; Quintero-Bermudez, R.; Vafaie, M.; Pina, J. M.; Proppe, A. H.; Hou, Y.; Walters, G.; Kelley, S. O.; Tisdale, W. A.; Sargent, E. H. Multication perovskites prevent carrier reflection from grain surfaces. Nat. Mater. **2020**, 19, 412−418.
83. Solar Futures Study; Solar Energy Technologies Office, U.S. Department of Energy, Sept 8, **2021**. https://www.energy.gov/eere/ solar/solar-futures-study.

84. Dunlop, E. D.; Halton, D.; Ossenbrink, H. A. 20 years of life and more: where is the end of life of a PV module? Conference Record of the Thirty-first IEEE Photovoltaic Specialists Conference **2005**, 1593− 1596.
85. Siegler, T. D.; Dawson, A.; Lobaccaro, P.; Ung, D.; Beck, M. E.; Nilsen, G.; Tinker, L. L. The Path to Perovskite Commercialization: A Perspective from the United States Solar Energy Technologies Office. ACS Energy Lett. **2022**, 7, 1728−1734.
86. Zhang, X.; Liu, H.; Wang, W.; Zhang, J.; Xu, B.; Karen, K. L.; Zheng, Y.; Liu, S.; Chen, S.; Wang, K.; Sun, X. W. Hybrid Perovskite Light-Emitting Diodes Based on Perovskite Nanocrystals with Organic-Inorganic Mixed Cations. Adv. Mater. **2017**, 29 (18).1606405.
87. Tian, W.; Zhou, H.; Li, L. Hybrid organic−inorganic perovskite photodetectors. Small **2017**, 13, No. 1702107.
88. Guo, X.; Asuo, I. M.; Pignolet, A.; Nechache, R.; Cloutier, S. G. Ambient Fabrication of Efficient Triple Cation Perovskite-Based nearInfrared Light-Emitting Diodes. Opt. Mater. Express **2022**, 12, 153− 165.
89. Sa, R.; Liu, D.; Chen, Y.; Ying, S. Mixed-Cation Mixed-Metal Halide Perovskites for Photovoltaic Applications: A Theoretical Study. ACS Omega **2020**, 5, 4347−4351.
90. Cho, H.; Kim, J. S.; Wolf, C.; Kim, Y. H.; Yun, H. J.; Jeong, S. H.; Sadhanala, A.; Venugopalan, V.; Choi, J. W.; Lee, C. L.; Friend, R. H.; Lee, T. W. High-Efficiency Polycrystalline Perovskite Light Emitting Diodes Based on Mixed Cations. ACS Nano **2018**, 12 (3), 2883−2892.
91. Ren, M.; Cao, S.; Zhao, J. et al. Advances and Challenges in Two-Dimensional Organic–Inorganic Hybrid Perovskites Toward High-Performance Light-Emitting Diodes. Nano-Micro Lett. **2021**, 13, 163.
92. Babbe, F.; Sutter-Fella, C. M. Optical Absorption-Based In Situ Characterization of Halide Perovskites. Adv. Energy Mater. **2020**, 10 (26), 1903587.
93. Del Cueto, J. A.; Rummel, S.; Kroposki, B.; Osterwald, C.; Anderberg, A. Stability of CIS/CIGS modules at the outdoor test facility over two decades. Presented at the 33rd IEEE Photovoltaic Specialists Conference; San Diego, California, May 11−16, **2008**; pp 1− 6..
94. Poorkazem, K.; Kelly, T. L. Compositional Engineering to Improve the Stability of Lead Halide Perovskites: A Comparative Study of Cationic and Anionic Dopants. ACS Appl. Energy Mater. **2018**, 1, 181−190.

95. Aharon, S.; Dymshits, A.; Rotem, A.; Etgar, L. Temperature Dependence of Hole Conductor Free Formamidinium Lead Iodide Perovskite Based Solar Cells. J. Mater. Chem. A. **2015**, 3, 9171−9178.
96. https://www.ossila.com/en-jp/pages/spin-coating#spin-coating-thickness-equation
97. Zhang, Y.; Chen, M.; Zhou, Y. Y.; Li, W. H.; Lee, Y. H.; Kanda, H.; Gao, X. X.; Hu, R. Y.; Brooks, K. G.; Zia, R.; Kinge, S.; Padture, N. P.; Nazeeruddin, M. K. The Synergism of DMSO and Diethyl Ether for Highly Reproducible and Efficient $MA_{0.5}FA_{0.5}PbI_3$Perovskite Solar Cells. Adv. Energy Mater. **2020**, 10 (29), 2001300.
98. Wang, L. Y.; Deng, L. L.; Wang, X.; Wang, T.; Liu, H. R.; Dai, S. M.; Xing, Z.; Xie, S. Y.; Huang, R. B.; Zheng, L. S. Di-isopropyl Ether assisted Crystallization of Organic-inorganic Perovskites for Efficient and Reproducible Perovskite Solar Cells. Nanoscale **2017**, 9, 17893−17901.
99. Paek, S.; Schouwink, P.; Athanasopoulou, E. N.; Cho, K. T.; Grancini, G.; Lee, Y.; Zhang, Y.; Stellacci, F.; Nazeeruddin, M. K.; Gao, P. From Nano- to Micrometer Scale: The Role of Antisolvent Treatment on High Performance Perovskite Solar Cells. Chem. Mater. **2017**, 29, 3490−3498.
100. Xiao, M. D.; Huang, F. Z.; Huang, W. C.; Dkhissi, Y.; Zhu, Y.; Etheridge, J.; Gray-Weale, A.; Bach, U.; Cheng, Y. B.; Spiccia, L. A Fast Deposition-Crystallization Procedure for Highly Efficient Lead Iodide Perovskite Thin-Film Solar Cells. Angew. Chem., Int. Ed. **2014**, 53, 9898−9903.
101. Lee, K.-M.; Lin, C.-J.; Liou, B.-Y.; Yu, S.-M.; Hsu, C.-C.; Suryanarayanan, V.; Wu, M.-C. Selection of anti-solvent and optimization of dropping volume for the preparation of large area sub-module perovskite solar cells. Sol. Energy Mater. Sol. Cells **2017**, 172, 368−375.
102. Singh, T.; Ikegami, M.; Miyasaka, T. Ambient Fabrication of 126 μm Thick Complete Perovskite Photovoltaic Device for High Flexibility and Performance. ACS Appl. Energy Mater. **2018**, 1 (12), 6741−6747.
103. Yang, W. S.; Noh, J. H.; Jeon, N. J.; Kim, Y. C.; Ryu, S.; Seo, J.; Seok, S. Il. High-Performance Photovoltaic Perovskite Layers Fabricated through Intramolecular Exchange. Science **2015**, 348, 1234−1237.
104. Li, H.; Cui, C.; Xu, X.; Bian, S.; Ngaojampa, C.; Ruankham, P.; Jaroenjittchai, A. P. A Review of Characterization of Perovskite Film in Solar Cells by Spectroscopic Ellipsometry. Sol. Energy **2020**, 212 (June), 48−61.

105. Extance, A. Perovskites on trial. Nature **2019**, 570, 429−432.
106. Agarwal, A.; Omagari, S.; Vacha, M. Nanoscale Structural Heterogeneity and Efficient Intergrain Charge Diffusion in a Series of Mixed MA/FA Halide Perovskite Films. ACS Energy Lett. **2022**, 7, 2443−2449.

Chapter 3

Nanoscale structural heterogeneity and photoluminescence dynamics in a series of mixed MA/FA halide perovskite

3.1 Introduction

Perovskite solar cells are improving very rapidly, reaching over 25% power conversion efficiency[1,2] in the last few years. Initially, methylammonium lead halides ($CH_3NH_3PbX_3$; hereafter denoted as $MAPbX_3$, where $MA = CH_3NH_3^+$ and $X = Cl^-$, Br^-, or I^-), have attracted attention for photovoltaic applications and have generated an extensive body of work in the literature on the unique properties of these rediscovered materials.[3] Recently, mixed ion hybrid perovskites have been introduced in which the anion I^- is mixed with Br^- and Cl^-, or the cation MA^+ is mixed with formamidinium (FA^+), Rb^+ or Cs^+. In addition, Pb^+ can be substituted with Sn^+ and more combinations have been attempted as well.[4] These developments represent a new phase in the perovskite solar cells research. Currently, the promising material appears to be triple cation (containing Cs^+, MA^+ and FA^+, with high FA ratio) perovskite with mixed anions (I^- and Br^-).[2,3] The goal of systematically mixing the ratios[5,6] of these materials is to improve both the performance and ambient stability, but there are still several major drawbacks[7-22] to their practical use. These materials are largely limited by the grain boundaries[13,14] and by the presence of defects[8,9,15,22] that can trap photo-generated charge carriers[10,11,16] and lead to their non-radiative recombination[12,17-20] and structural heterogeneity.[15,16,21]

Fluorescence microscopy in combination with other techniques has served as a powerful tool to find nanoscale structure−function relationship in a variety of materials[23] including perovskite thin films[24,25] and has provided insight into potential sources of nonradiative loss[20,21] and heterogeneity in perovskites.[14,15] Further studies using photoluminescence (PL) and electroluminescence (EL) imaging and spectroscopy have revealed the local photophysics of a variety of other perovskite materials such as micro- and nanocrystals or quantum dots.[26-38] Effective utilization of these fluorescence techniques can give access to local energy transport, grain boundaries and charge pathways to help rationally control these fundamental processes and improve the efficiency of solar cells, light-emitting diodes or lasers.[39-41]

However, whether carrier transport or recombination dominates the optoelectronic heterogeneity is still unclear.[40] For example, there have been reports that PL intensities and lifetimes varied between different grains in the same sample and that grain boundaries were generally dimmer and exhibited faster photoluminescence decays.[13,14,42] On the other hand, other groups interpreted similar local variations in PL intensity as variations in nonradiative

recombination rates due to heterogeneous distributions of surface traps.[15,16,21] The origins of the PL heterogeneity in perovskites and the existence of structural and electronic barriers to lateral carrier diffusion in perovskite film are important topics that affect the performance of perovskite solar cells and other perovskite optoelectronic devices, and in addition, affect the analysis of many other experiments including the extraction of fundamental properties such as conductivity and charge carrier density.

To address these important questions, we used wide-field fluorescence microscopy to better understand the interplay between local nonradiative recombination and structural heterogeneity in explaining the PL properties of mixed cation hybrid perovskites. While in situ microscopic observation has brought valuable insight into the anion exchange mechanism in mixed anion perovskites[35,36] there have been no attempts so far to characterize on nanoscale level the mixed cation materials. We investigated the PL fluctuations and local PL spectra in a series of $MA_{1-x}FA_xPbI_3$ polycrystalline films of ~ 450 nm thickness with changing FA ratio from 0% (x = 0) to 100% (x = 1) using two different antisolvents, chlorobenzene (CB) and ethyl acetate (EA).[43,44] The films unexpectedly show PL blinking which is correlated over micrometer scale distances, as well as distributions of local PL spectra in the mixed films reflecting the local compositional heterogeneities.

3.2 Experimental methods

3.2.1 Sample preparation

The perovskite films are prepared on a layer of PEDOT-PSS deposited on microscope cover glass. Films prepared using both CB and EA generally show good crystallinity. The film preparation procedure was optimized by adjusting the concentration of the precursor and by selection of the antisolvents, as detailed below.

Synthesis of mixed MA/FA perovskite films: $MA_xFA_{1-x}PbI_3$ perovskite films have been synthesized by the method reported before[43] with some modifications. In brief, a microscope cover glass freshly cleaned with acetone, isopropanol and deionized water has been used as a substrate. A 40 nm thick layer of PEDOT: PSS (Clevios P AI4083, H. C. Starck) was spin-coated (at 4000 rpm for 40 s) on the glass substrate and annealed at 150 °C for 15 min. On top of that the perovskite layer was deposited. For that, a series of 1M perovskite precursor solutions were prepared by mixing PbI_2, MAI (methylammonium

iodide) and FAI (formamidinium iodide) with molar ratios of 1:1:0, 1:0.9:0.1, 1:0.7:0.3, 1:0.5:0.5, 1:0.3:0.7 and 1:0:1, respectively, in 1 ml solvent mix of DMSO (20%) and DMF (80%) by vigorous stirring at 60 °C. The precursor solutions were spin-coated on the substrates at 1000 rpm for 10 s followed by 5000 rpm for 30 s. In the last 10 s of the 5000 rpm spinning, 100 μL of chlorobenzene (CB) or 100 μL of ethyl acetate (EL) were dropped on the films as antisolvents. The perovskite films were annealed at 100 °C for 40 min. The film thickness was around 450 nm. The above preparation conditions are a result of optimization of the original method of the ref. 43. The precursor concentration of 1.4 M used in ref. 43 lead to larger grain size, but the films showed large numbers of pinholes as shown in Figure 2.13, more roughness and overall larger morphological heterogeneity.

3.2.2 SEM Characterization

Scanning electron microscopy (SEM) was performed using JSM-7500F (JEOL Ltd.) on all the samples. The SEM images of the MA/FA series (0% - 100%) of the films prepared with the CB and EA antisolvents were described in Chapter 2 and shown in Figures 2.14 and 2.16.

3.2.3 UV-Vis absorption and bulk PL spectra

The UV–Vis absorption spectra were measured using V760 (Jasco) absorption spectrometer. The absorption spectra for the series of MA/FA series (0% - 100%) of the films prepared with the CB and EA antisolvent are shown in Figure 3.1. Bulk sample PL spectra were measured using Quantaurus-QY (Hamamatsu Photonics) system. The system is equipped with a xenon lamp as the excitation source, a monochromator, an integrating sphere, and a multichannel detector.

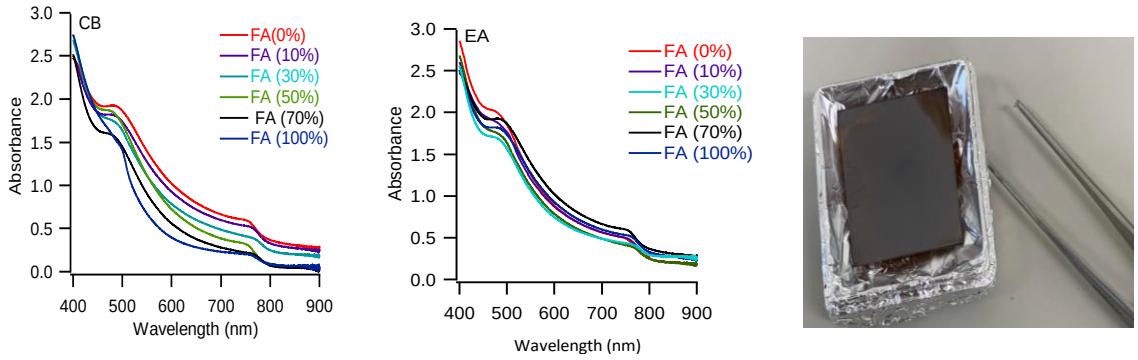

Figure 3.1. Absorption spectra of the perovskite films

3.2.4 Outline for microscopy characterization

We use fluorescence microscopy as shown schematically in Figure 3.2 to study the nanoscale PL properties (local nanoscale intensity and spectra) of a series of mixed cation perovskite $MA_{1-x}FA_xPbI_3$ films.

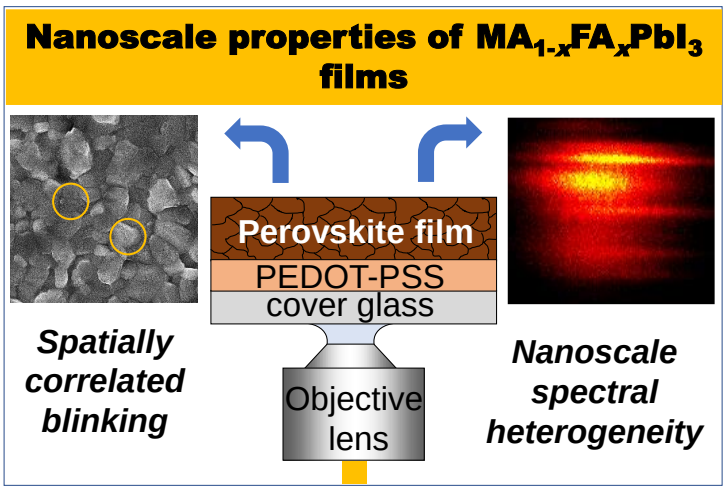

Figure 3.2. Schematic diagram of microscopic study on perovskite films.

Fluorescence microscopy and spectroscopy:

Fluorescence from the perovskite films was measured using an inverted microscope (IX 71, Olympus). The excitation light was the 442 nm line of a continuous wave He-Cd laser (Kimmon). The excitation power measured at the microscope stage was on the order of 26 W/cm^2. Fluorescence was collected by an oil immersion objective lens (UplanFLN 100×, N.A. 1.3, Olympus) and passed through a set of a dichroic mirror and a long-pass filter. For the spectral measurements the signal was further dispersed using an imaging spectrograph (CLP-50LD, Bunkou Keiki). The spectrograph uses a flipping mirror (in front of the grating) which, when used, relays the microscopic image to the CCD camera. In this imaging mode an emitting spot in the film is brought into the center of the image, the spectrograph slit is closed and the mirror is removed. The fluorescence signal falling into the vertical slit is spectrally dispersed, and at the vertical position of the film provides the local fluorescence spectrum. Fluorescence was detected with an electron-multiplying (EM) CCD camera (iXon,

Andor Technology) with an exposure time of 30 ms for blinking and of 50 ms for spectral measurements.

Data analyses:

Single-particle imaging and spectroscopy data were analyzed using ImageJ2 (NIH) and Igor Pro 5.05A. PL intensity traces were obtained from each marked spot. Here, we integrated the intensity over the whole spot and subtract the averaged background. The background was obtained from the area around the respective spots. Resultant traces were used for further analysis. The intensity time trajectories from a well-separated emission spot (5 × 5 pixels) were obtained using 'Z-profile' in ImageJ and data were exported in TIFF format for further analysis. Only those emissive spots showed characteristic emission of $MA_X/FA_{1-X}PbI_3$ thin films and microcrystal emission signature. PL spectral profiles from spectrally resolved images were obtained by integrating 5 pixels along with vertical (position) direction and an average background of the same dimension was subtracted to obtain the PL spectrum. The spectrograph was calibrated using several laser lines. The spectral information such as peak positions and full width at half maximum (FWHM) for each spot was obtained by fitting with a Gaussian function.

3.3 Results and discussion

3.3.1 Perovskite film characterization

For the CB antisolvent, the films occasionally contain pinholes and the grains are smaller and have more elongated shapes (as shown in the examples in Figure 3.3a, b for FA 30% SEM images. The average grain sizes evaluated from the SEM images (Figure 3.3c) are on the order of few hundreds of nm and are larger for the EA antisolvent for all compositions, with maximum values for the FA 30% to FA 50% range. We note, however, that the SEM data presented are measured only from the film surfaces and do not provide any information on the grain structure and grain interfaces inside the bulk of the films. The film absorption spectra (Figure 3.3d) show features typical for this type of perovskite material.[5]

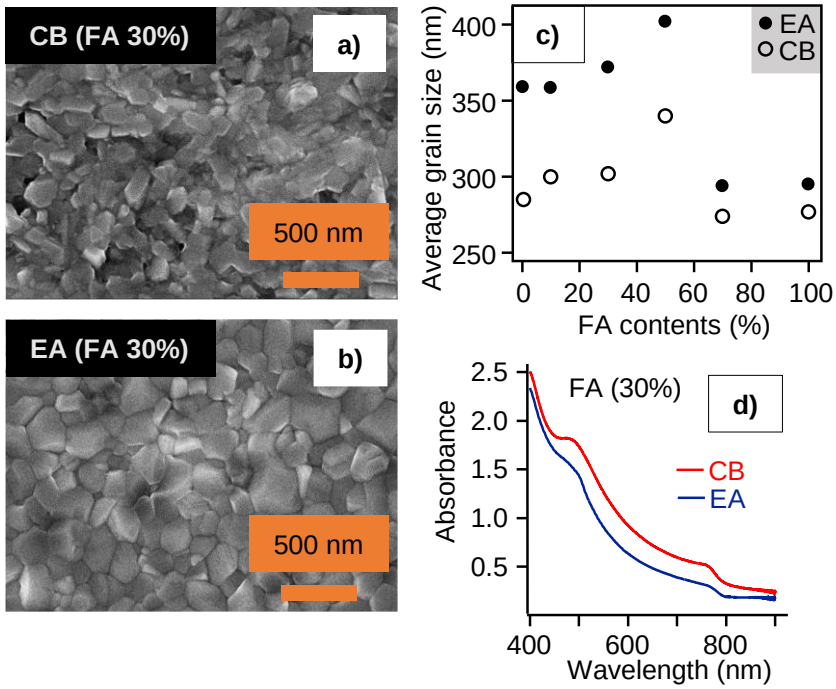

Figure 3.3. (a), (b) SEM images of FA 30% films prepared using chlorobenzene (a) and ethyl acetate (b) antisolvents. (c) Average crystal grain size as a function of FA content evaluated from the SEM images. (d) Absorption spectra of the FA 30% films.

The bulk PL spectra of the films show continuous red shift with increasing FA content for both antisolvents (Figure 3.4 a-f for EA, Figure 3.5 a-f for CB), similar to previous reports.[5] The PL peaks for the FA 0%, FA 10%, FA 30%, FA 50%, FA 70% and FA 100% are at 785 nm, 792 nm, 801 nm, 809 nm, 819 nm and 824 nm for CB, and similarly at 784 nm, 793 nm, 802 nm, 810 nm, 817 nm and 823 nm for EA, respectively. The peak positions and full-width-at-half-maxima (FWHM) are plotted in Figure 3.4g and Figure 3.5g.

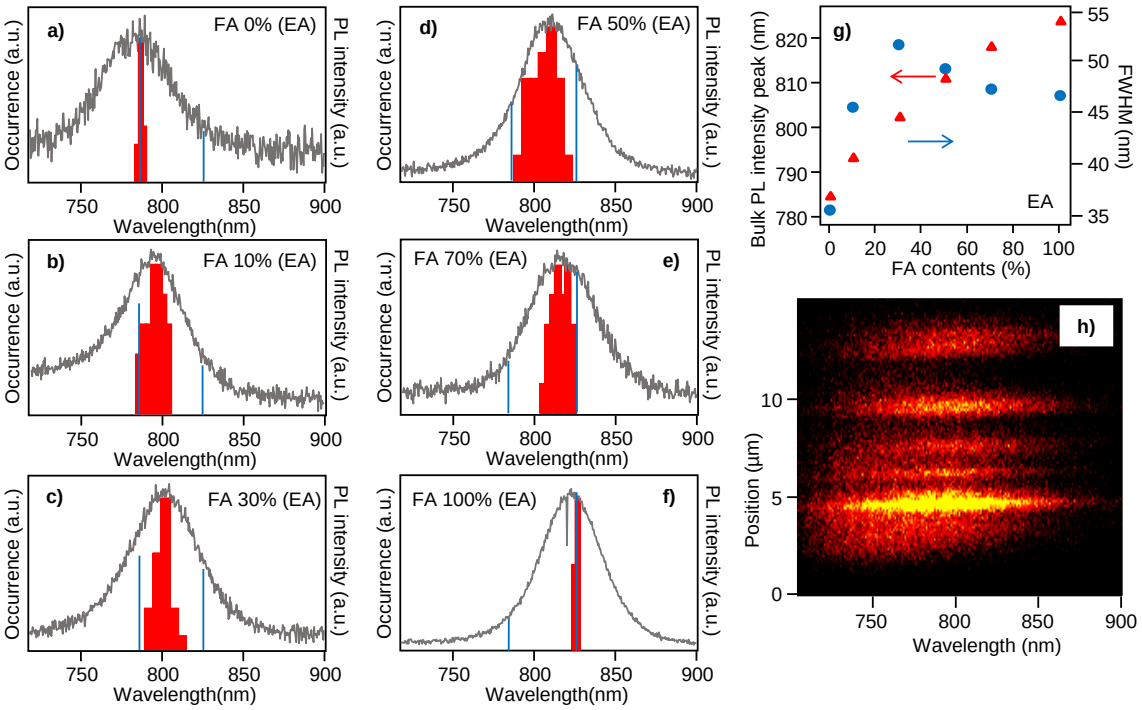

Figure 3.4. (a)-(f) Bulk PL spectra (solid grey lines) and histograms of local PL spectral maxima (red bars) for different compositions of films prepared using the EA antisolvent. The blue lines indicate the positions of the distribution peaks for FA 0% and FA 100% samples. (g) PL spectral maxima (red symbols) and FWHM (blue symbols) obtained from the bulk film PL spectra in (a)-(f) for the different compositions. (h) Example of 2D spectral plot (position vs. wavelength) for a selected location in the FA 30% film.

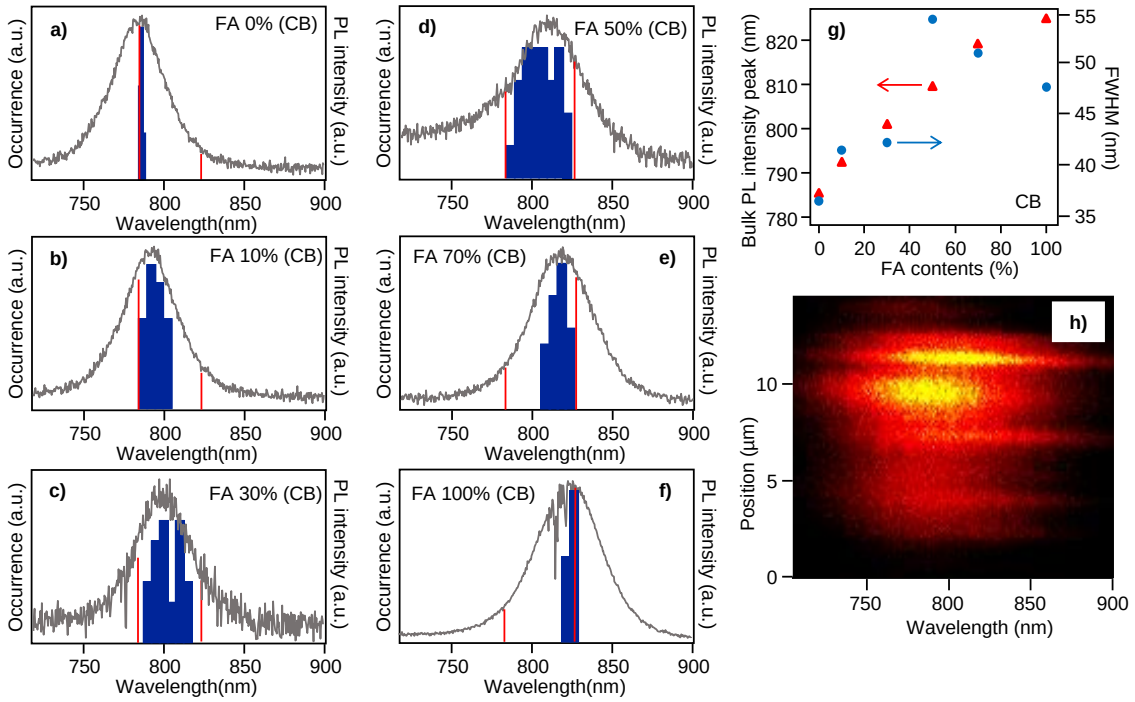

Figure 3.5. (a)-(f) Bulk PL spectra (solid grey lines) and histograms of local PL spectral maxima (blue bars) for different compositions of films prepared using the CB antisolvent. The red lines indicate the positions of the distribution peaks for FA 0% and FA 100% samples. (g) PL spectral maxima (red symbols) and FWHM (blue symbols) obtained from the bulk film PL spectra in (a)-(f) for the different compositions. (h) Example of 2D spectral plot (position vs. wavelength) for a selected location in the FA 30% film.

3.3.2 Nanoscale PL spectroscopy

On microscopic level, the emission from the perovskite films is spatially heterogeneous with bright emitting spots on a darker background. We carried out nanoscale spectral characterization by measuring PL spectra from the individual bright emitting spots in the different films. Examples are shown in Figure 3.4h and Figure 3.5h. For each sample we analyzed approximately 50 spectra taken at different locations in the films, and plotted the PL maxima in histograms in Figure 3.4a-f for EA and in Figure 3.5a-f for CB. For the FA 0% and FA 100 % films, the PL peaks show narrow distributions and mostly coincide with the bulk PL maxima. The mixed cation samples (FA 10%, FA 30%, FA 50% and FA 70%) show much broader distributions of the local spectral PL peaks, similar for both

antisolvents. The broadest distributions are found for the FA 50% samples. For both CB and EA these distributions stretch from 794 nm to 824 nm, thus covering the whole spectral range corresponding to all compositions from FA 0% to FA 100%. The examples in Figure 3.4h and Figure 3.5h show that such spectral diversity can be observed within 10 μm region of the film. The nanoscale spectral distributions in the mixed ion films are an unexpected result and provide evidence of local compositional heterogeneity of the films. In particular, the FA 50% samples contain purely MA domains (FA 0%-like spectra), purely FA domains (FA 100% -like spectra) and domains composed of mixed MA/FA cations of varying ratios. The existence of the nanoscale spectral distributions also helps to explain the larger FWHM of the bulk spectra of the mixed ion samples (Figure 3.4g and Figure 3.5g)

One possible origin of the compositional heterogeneity could be migration of the cations with the films. We checked for such possibility on two different time scales. First, we looked at spectral stability from individual spots over the periods of tens of seconds but found no signs of spectral diffusion which would point to local compositional changes. Second, we measured the spectral distribution of the FA 50% samples on the day the samples were prepared, and then checked the distributions again after 3 weeks. We have not observed any differences between the distribution widths over the prolonged periods of time. This result suggests that the compositional heterogeneity is a result of the film fabrication process and that the as-prepared film is structurally stable without any signs of cation migration.

The fact that we observe PL spectra covering the whole range of wavelengths indicates that reabsorption (or photon recycling) is not effective despite the favorable overlap of the high-energy domain PL spectra with the low-energy domain absorption. One reason for this might be that we detect emission mainly from the interface between the perovskite film and the PEDOT layer, that is, emission propagating away from the bulk of the film. The situation could be different for PL passing the thickness of the film where the shorter-wavelength emission could be reabsorbed. On the other hand, this suppression of the reabsorption on the surface gives us the opportunity to spectrally detect the compositional heterogeneity of the films.

Apart from reabsorption, another closely related process is resonant energy transfer from the high-energy domains to the low-energy ones. The conditions for this process (spectral overlap) are also favorable, and energy transfer can happen in the plane of the film surface. Such efficient energy transfer could prevent emission from the high-energy

domains by funneling all the excitation to the lowest energy ones which would be emitting. The fact that we do observe the whole range of PL spectra indicates that this funneling is not taking place in the films.

3.3.3 PL blinking

Another unexpected observation from the microscopic PL characterization is that many of the bright emission spots show PL intensity fluctuations, so called blinking. PL blinking is readily observed for perovskite nanocrystals and even for microcrystals of various shapes[17,20,27,33] but rarely in bulk films.[15,24] Examples of PL images of the FA 50% films for both CB and EA antisolvents are shown in Figure. 3.6a, d. Continuous detection of hundreds of such consecutive microscopic images reveals the presence of different blinking spots in the samples. Analysis of the images provides PL intensity time traces (blinking traces), examples of which are also shown in the Figure 3.6b, e, together with their locations. Interestingly, for the examples shown, the blinking from different locations shows high degree of correlation. Blinking correlated over the whole area of a single microcrystal has been shown before[27] but is unexpected for polycrystalline films. Here, the correlation is preserved over significant distances. For the example in Figure 3.6a, for FA 50% CB the distance from spot 1 to spot 2 is 3.2 μm and that from spot 1 to spot 3 is 4.4 μm. The extent of correlation between the blinking traces was evaluated by calculating the Pearson's coefficient. Its value for the blinking traces 1 and 2 is 0.54, and that for the traces 1 and 3 is 0.58. Similarly, for FA 50% EA in Figure 3.6d the distances between spots 1 and 2, and 1 and 3 are 2.4 μm and 3.7 μm, respectively, with the corresponding Pearson's coefficients of 0.82 and 0.75. Overall, we observe similar trends with comparable degree of correlation in all films used in this study. The Figure 3.7 and Figure 3.8 show examples of blinking traces for all film compositions for the CB and EA antisolvents, respectively. Similar to Figure 3.6b, e, each example shows three traces that are correlated to a large extent. The distance between the blinking spots is on the order of several μm and the corresponding Pearson's coefficients are summarized in Table 3.1. As seen from the table, for all films we find pair of locations that show Pearson's coefficient larger than 0.4, and for most of the films it is larger than 0.5.

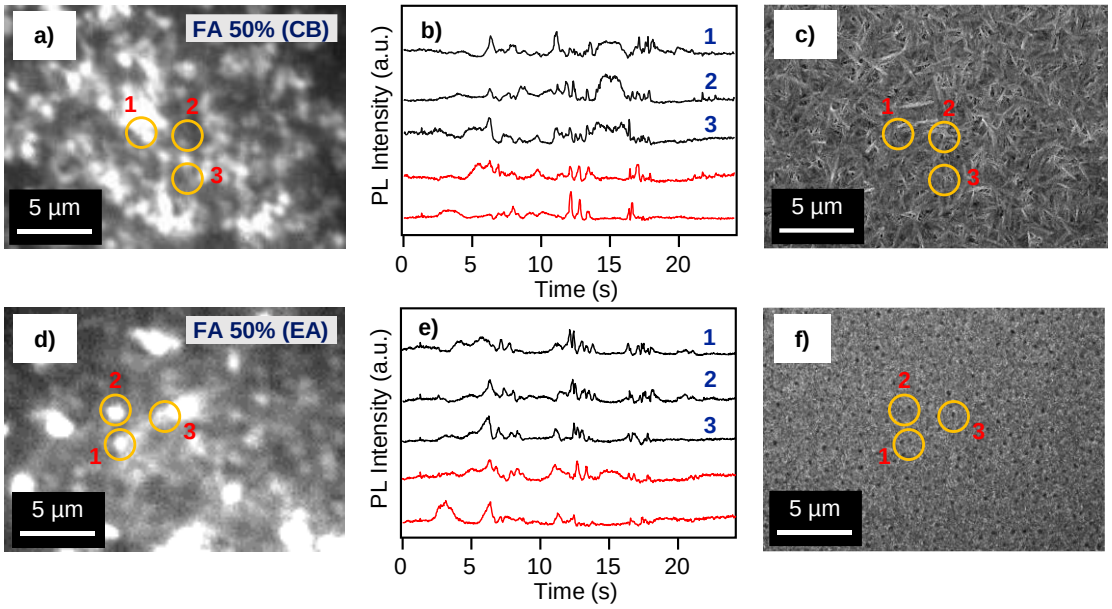

Figure 3.6. (a), (d) Microscopic PL images of the FA 50% films prepared using CB (a) and EA (d) antisolvents. The numbered circles indicate positions where the blinking was analyzed. (b), (e) PL intensity time traces (blinking) obtained at different locations in the two films, (b) for CB, (e) for EA, including the positions indicated in (a), (d). (c), (f) SEM images of the FA 50% films prepared using CB (c) and EA (f) antisolvents. The circles illustrate the relative positions of the blinking locations obtained in the PL images on the same scale. The circles in PL and SEM images do not indicate the same locations in the sample.

FA 0% CB	FA 0% EA	FA 10% CB	FA 10% EA	FA 30% CB	FA 30% EA	FA 50% CB	FA 50% EA	FA 70% CB	FA 70% EA	FA 100% CB	FA 100% EA
spot 1 to 2,3,4,5	spot 1 to 2,3,4,5	spot 1 to 2,3,4,5	spot 1 to 2,3,4,5	spot 1 to 2,3,4,5	spot 1 to 2,3,4,5	spot 1 to 2,3,4,5	spot 1 to 2,3,4,5	spot 1 to 2,3,4,5	spot 1 to 2,3,4,5	spot 1 to 2,3,4,5	spot 1 to 2,3,4,5
0.597808	0.429211	0.515777	0.613238	0.570714	0.546692	0.541831	0.820032	0.643766	0.4234124	0.502323	0.475913
0.525925	0.469449	0.59095	0.529567	0.518788	0.576491	0.575899	0.752043	0.612894	0.44762	0.464124	0.419735
0.222686	0.146788	-0.0976777	0.19402	0.184285	-0.216772	0.282869	0.205804	0.158085	-0.184958	0.0278712	0.00322091
0.134592	0.242533	0.171817	0.0912973	0.045937	0.0384592	-0.113649	0.00322091	-0.00291135	0.155499	-0.0550131	0.285817

Table 3.1. Pearson's coefficients between PL blinking traces at selected locations (spots) 1-5 in films of different compositions.

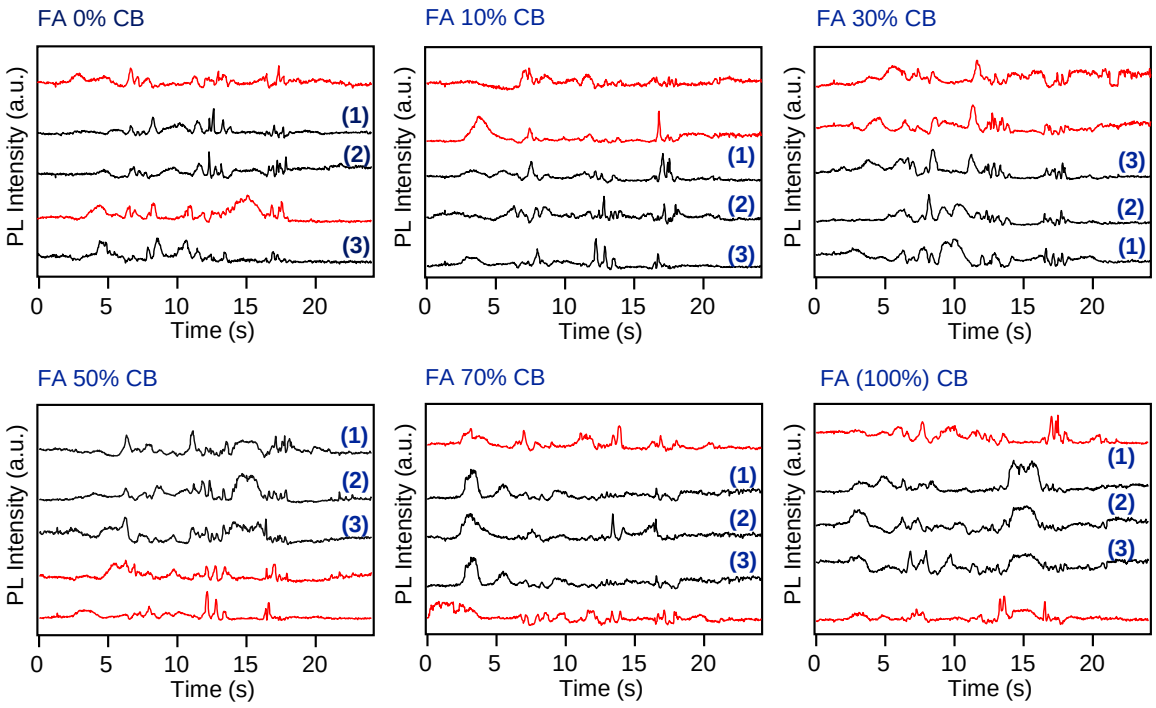

Figure 3.7. PL intensity time traces (blinking) obtained at different locations in the films of different FA content, prepared from the CB antisolvent. The numbers indicate traces from different locations that are correlated to a significant extent. The corresponding Pearson's coefficients are presented in Table 3.1.

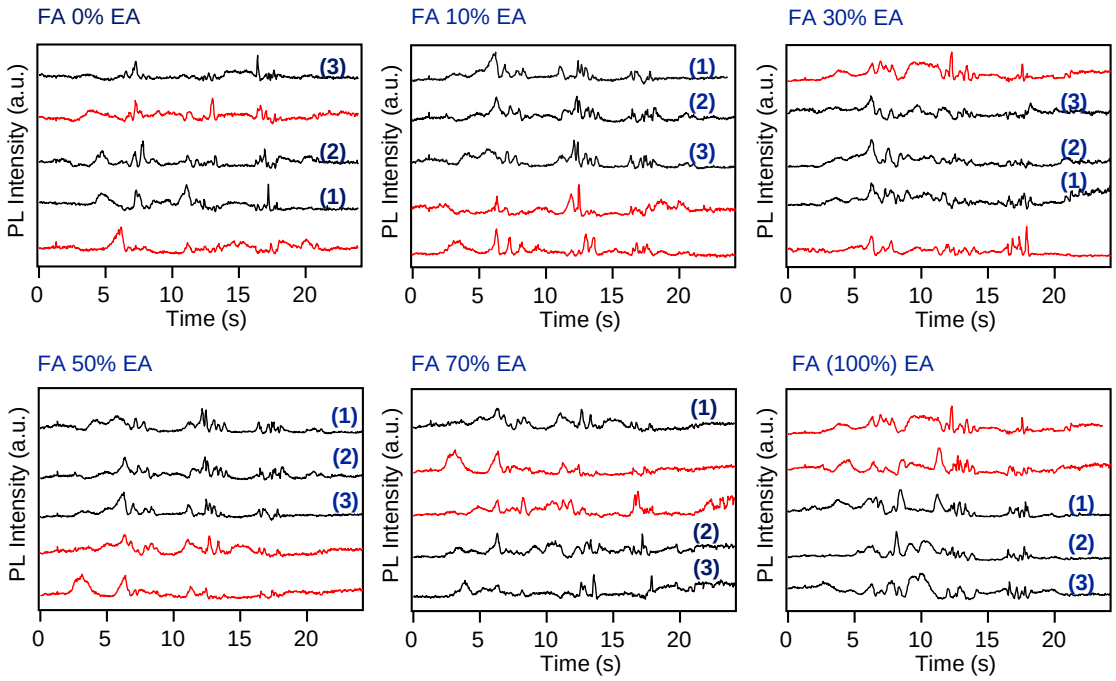

Figure 3.8. PL intensity time traces (blinking) obtained at different locations in the films of different FA content, prepared from the EA antisolvent. The numbers indicate traces from different locations that are correlated to a significant extent. The corresponding Pearson's coefficients are presented in Table 3.1.

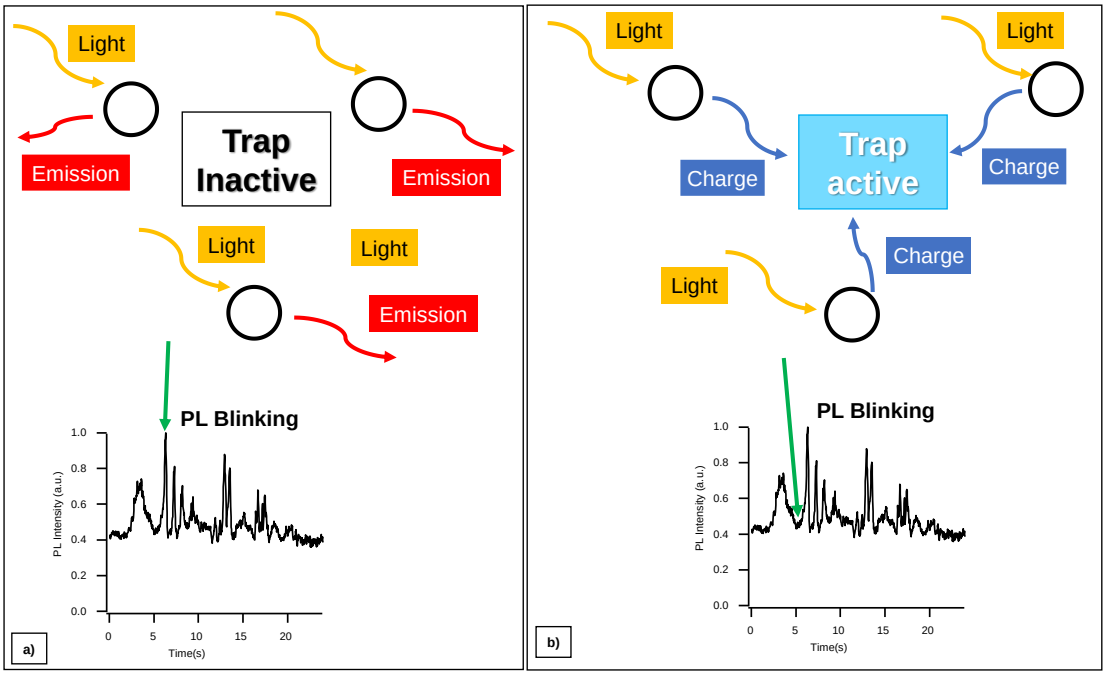

Figure 3.9. Schematic diagram of PL fluctuation

3.3.4 Mechanism of PL blinking

The correlated PL blinking observed for the perovskite films shows similarities with PL blinking of single nano- or microcrystals of different perovskite materials,[17,20,27,33] which in many cases is correlated over the whole crystal size. It has been argued in literature that the blinking in such perovskite microcrystals originates from the presence of a very efficient quenching defect (charge trap) which can switch between active and inactive states.[17] This proposed mechanism is schematically shown in the Figure 3.9. If the trap is inactive (Figure 3.9a), the neighboring crystal domains in the film absorb light and the photocarriers forming the exciton recombine radiatively, leading to high PL intensity (so called 'on' state in the blinking trace). When the trap switches to an active state the photocarriers excited in its vicinity migrate to the trap and recombine non-radiatively, leading to a decrease of PL intensity and appearance of the dim ('grey') or 'off' states in the blinking trace (Figure 3.9b).

While the physical origin of the switchable active-inactive quencher (trap) is still debated and there is no consensus on its nature, the correlated blinking phenomenon itself can provide valuable information on the charge (photocarrier) migration in the perovskite films. The large degree of correlation of blinking in the examples in Figure 3.6 (as well as

in Fig. 3.7 and Figure 3.8) means that in each sample the spots 1-3 share the same efficient quencher which has a capture radius of approximately 2 μm (or more). In other words, the long-distance correlated blinking points to efficient charge transport over distances on the order of 1 μm or more. It is interesting to put the distances between the spots 1-3 into perspective with the film microscopic structure. For illustration, the Figure 3.6c, f also shows SEM images of the same samples (however, the observation areas in PL and SEM images are *not* correlated). The comparison shows that on the way to the common trap from the spots 1-3 the charges have to cross many grain boundaries (on average 8 in the CB samples and 9 in the EA samples). The fact that in spite of these large numbers of grain boundaries, the blinking of the spots is still largely correlated indicates that the grain boundaries themselves do not function as traps and are transparent towards charge migration. A similar conclusion has been reached before on related perovskite films.[45]

It is interesting to consider the long-range efficient charge transport in context with the above-mentioned lack of energy funneling in the films. We have occasionally observed the whole range of the PL spectra across the spatial scale of 10 μm (e.g., Figure 3.4h). This implies lack of energy communication between individual film domains over micrometer distances, in contrast with the observed long-range correlation of the blinking. We note that we have previously observed similar lack of energy transfer and at the same time efficient charge transport in aggregates of $CsPbBr_3$ nanocrystals over the distances of hundreds of nm.[26]

3.3.5 Dynamic PL quenching

For further analysis we noticed significant differences between the blinking behavior of films with different composition. To quantify the differences we chose to evaluate what we term potential loss of PL intensity. This is illustrated in the blinking trace from one PL spot in Figure 3.10a. The intensity is normalized on a scale 0 – 1, where 1 corresponds to the maximum intensity during the blinking 'on' event. This value thus represents potentially the maximum PL intensity that can be emitted from this spot, and a decrease from this intensity in the form of 'grey' or 'off' events represents the intensity loss. In the Figure 3.10a this intensity loss is shaded in blue and is evaluated as a fraction of the total integrated potential intensity (which would be equal to 1 if the spot emitted with the maximum intensity throughout the measurement interval). We realize the shortcomings of this type of

analysis – it reflects the dynamic phenomenon of activating-deactivating the quencher, and it is monitored over a limited time interval of tens of seconds. It thus cannot account for permanent exciton quenching or quenching dynamics occurring with much longer timespans. With these limitations in mind we analyzed the blinking behavior for around 60-70 PL spots in each sample for both antisolvents and plotted the results in histograms in Figure 3.10b-g for EA and in Figure 3.11a-f for CB. It can be seen that the histogram peaks shift to lower intensity loss with increasing FA content from FA 0% to FA 50% and then start shifting back to higher loss for FA 70% and FA 100%. This trend is apparent from the plots of the histogram peaks vs. composition in Figure 3.10h and Figure 3.11g. For both the CB and EA antisolvents the minimum potential intensity losses are observed for the mixed FA 30% and especially FA 50% samples.

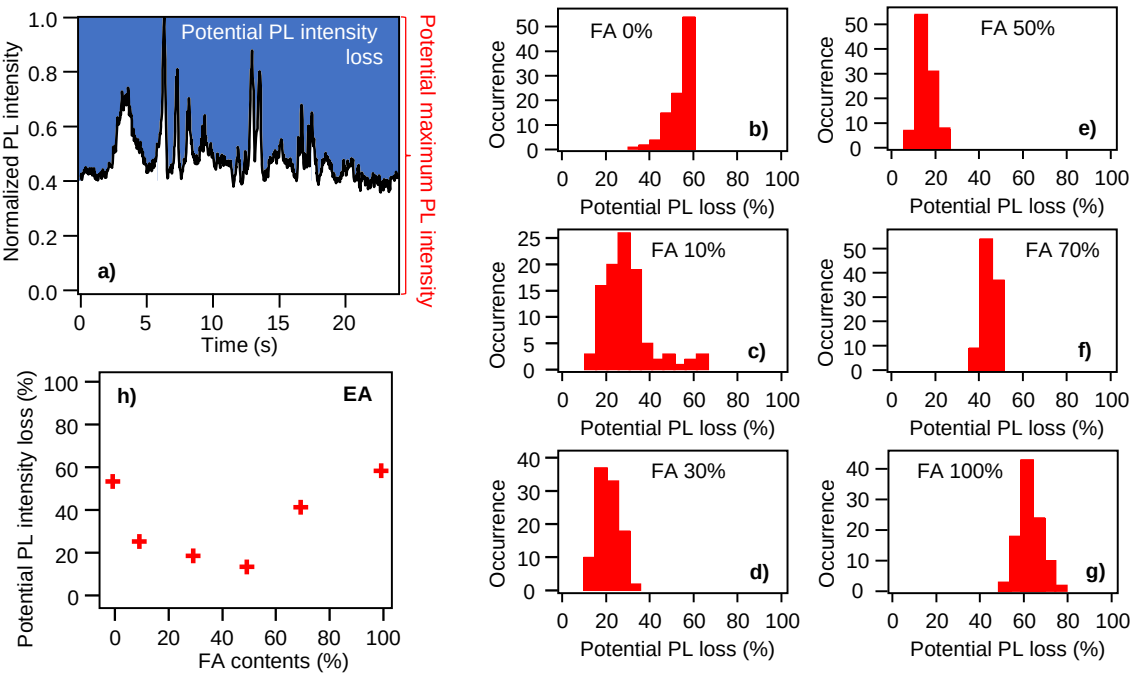

Figure 3.10. (a) An example of a blinking trace indicating schematically the definition of the potential PL intensity loss parameter. (b)-(g) Histograms of the potential PL intensity loss obtained for different film compositions prepared using the EA antisolvent. (h) Peaks of the distributions in (b)-(g) plotted as a function of the FA content.

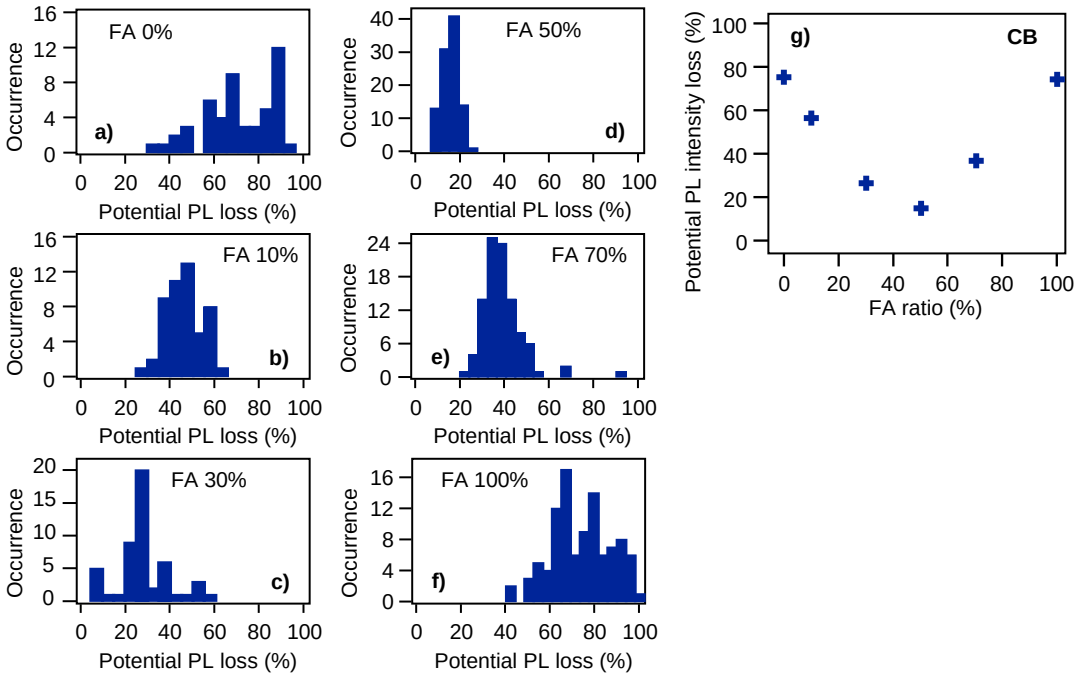

Figure 3.11. (a)-(f) Histograms of the potential PL intensity loss obtained for different film compositions prepared using the CB antisolvent. (g) Peaks of the distributions in (a)-(f) are plotted as a function of the FA content.

The minimum intensity loss for the FA 50% films means that the dynamic non-radiative relaxations due to the efficient switchable quencher are most suppressed for these samples. At the same time, the distribution of the PL spectra showed that the FA 50% films exhibit the largest compositional heterogeneity of all the samples. These seemingly contradictory results indicate that the presence of the truly mixed $MA_{1-x}FA_xPbI_3$ (x = 0.5) domains in the FA 50% films is crucial for the suppression of the dynamic non-radiative losses. In addition, the fact that despite the presence of pure MA and pure FA domains in these films we do not observe blinking behavior corresponding to these samples is another indication of the importance of efficient inter-grain charge transport. The formation of the truly mixed phase should be further optimized in the mixed cation film preparation.

3.4 Conclusions

In conclusion, we studied nanoscale structural and optical properties of a series of mixed cation halide perovskite films using fluorescence microscopy and spectroscopy. The use of this technique helped to uncover properties that are otherwise inaccessible using conventional characterization methods. In particular, the work surprisingly showed large nanoscale compositional heterogeneity of the mixed ion samples, something what was not expected from ensemble-level spectroscopy. It also showed that, within the heterogeneity, the truly mixed ion domains of the films are the ones least affected by the non-radiative losses, and are thus most promising in terms of the solar cell performance. In addition, the work showed that irrespective of the antisolvent used for the preparation, grain boundaries do not represent barriers for charge transport and do not work as charge traps, enabling efficient charge migration over micrometer distances.

3.5 Appendix

3.5.1 Effect of electron transporting layer (ETL) on perovskite films photophysics

The current experiments were done on perovskite films grown on a hole-transporting layer of PEDOT-PSS. It is interesting to see how the observed characteristics change for for perovskites grown on electron-transporting layers. For that we prepared the FA 50% film on the electron-transporting layer of SnO_2. The results presented in Figure 3.12 indicate that the long-distance correlation of blinking is preserved and is the property of the perovskite film itself.

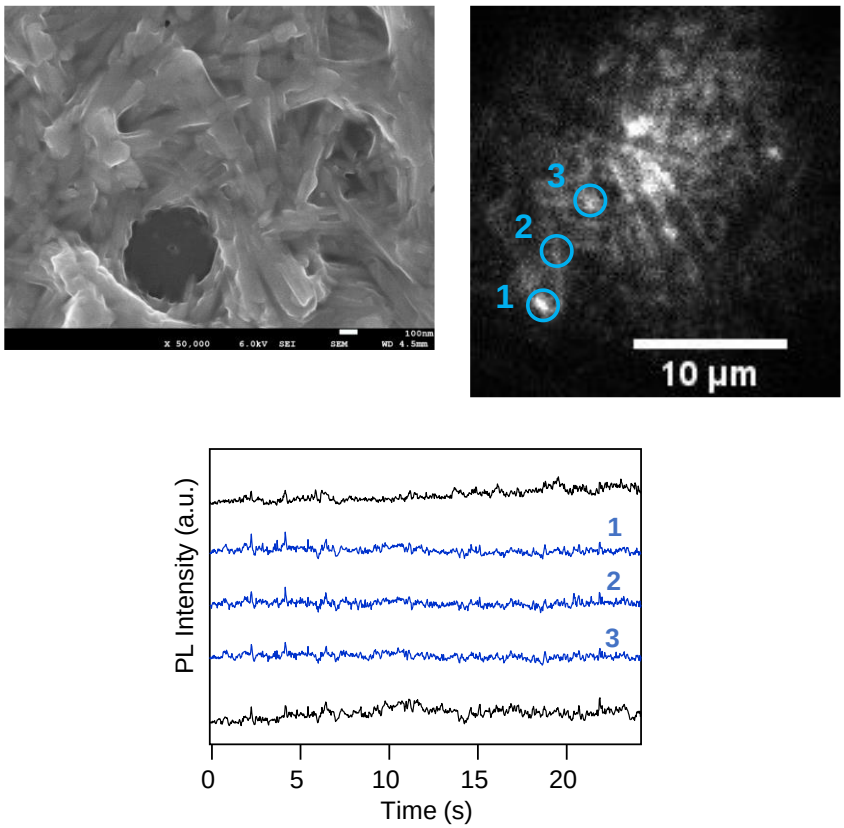

Figure 3.12. Top left: SEM images of perovskite film of the FA 50% composition prepared on the SnO_2 substrate. Top right: PL image of the same film with the numbers indicating locations where correlated blinking traces were detected. Bottom: PL blinking traces; the numbers correspond to the locations in the PL image. The Pearson's coefficient between the traces 1 and 2 is 0.78, that between 1 and 3 is 0.85.

3.5.2 Effect of antisolvent on the PL blinking

Preparation using antisolvents such as toluene, ether and isopropyl alcohol and the precursor concentration of 1 M resulted in films of lower quality, as shown in SEM images for the examples of the FA 50% films in the Figure. 3.13. Examples of PL blinking on these samples are also shown in the Figure 3.13. As the results show, the various kinds of antisolvents do not significantly affect the blinking dynamics.

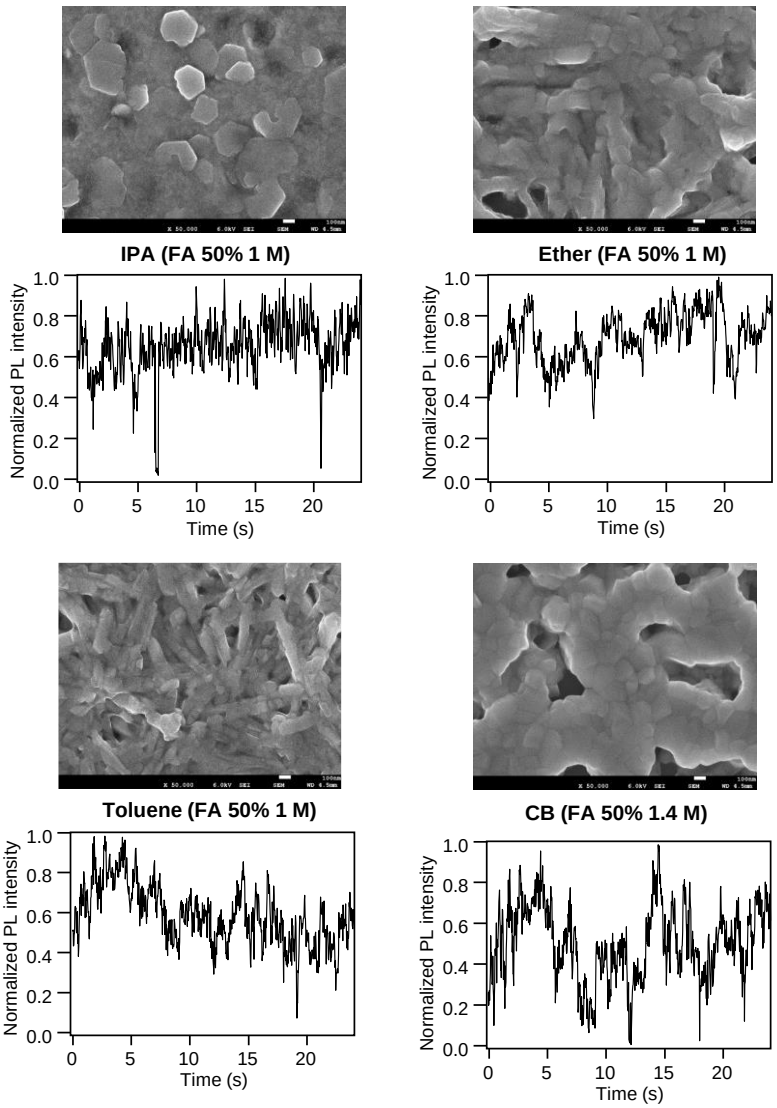

Figure 3.13. SEM images of FA 50% perovskite films prepared using different antisolvent and precursor concentrations (as indicated below the images), together with examples of representative PL blinking traces taken from the respective films.

3.5.3 Blinking density measurements

With regards to the PL blinking and the corresponding potential PL intensity loss, we also characterized the relative spatial occurrence of the blinking spots by analyzing 'blinking density' of the MA/FA series (0% - 100%) of the films prepared with the EA and CB, respectively, as shown in figure 3.14. The blinking density is defined as the ratio of the summed area of all blinking spots vs. the measured area. The results are given in the Table 3.2 and 3.3 for the CB and EA samples, respectively. We can see that the blinking density was lowest for the FA (50%) composition in both EA and CB as compared to other compositions. Also, for all the EA samples the blinking density was the lower compared to the CB samples of the same composition. These results well complement the conclusions obtained from the potential PL intensity loss analysis.

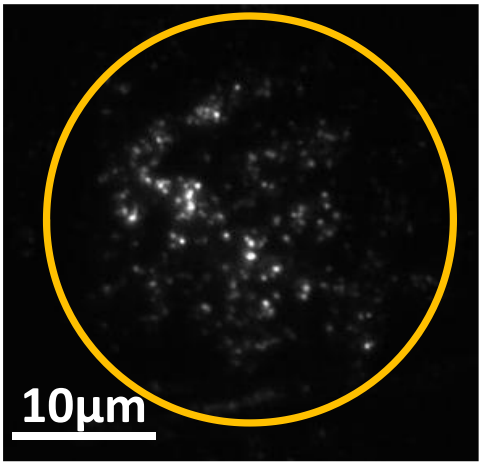

Figure 3.14. Schematic of blinking density calculation

Sample (CB)	Number of blinking spots	Measurement area (nm^2)	Summed area of the blinking spots (nm^2)	Blinking density (%)
0%	58	632525522	36014738	5.7
10%	64	632525522	39740400	6.3
30%	54	632525522	33530963	5.3
50%	33	632525522	20491144	3.2
70%	72	632525522	44707950	7.1
100%	76	632525522	47191725	7.5

Table 3.2. Blinking density calculation of the MA/FA series (0% - 100%) of the films prepared with the CB

Sample (EA)	Number of blinking spots	Measurement area (nm^2)	Summed area of the blinking spots (nm^2)	Blinking density (%)
0%	34	632525522	21112088	3.3
10%	44	632525522	27321525	4.3
30%	32	632525522	19870200	3.1
50%	21	632525522	13039819	2.1
70%	67	632525522	41603231	6.6
100%	68	632525522	42224175	6.7

Table 3.2. Blinking density calculation of the MA/FA series (0% - 100%) of the films prepared with the EA

3.6 References

1. Min, H.; Lee, D. Y.; Kim, J.; Kim, G.; Lee, K. S.; Kim, J.; Paik, M. J.; Kim, Y. K.; Kim, K. S.; Kim, M. G.; Shin, T. J., Sang, I. S. Perovskite Solar Cells with Atomically Coherent Interlayers on SnO_2 Electrodes. *Nature* **2021**, *598* (7881), 444–450.
2. Li, Z.; Li, B.; Wu, X.; Sheppard, S. A.; Zhang, S.; Gao, D.; Long, N. J.; Zhu, Z. Organometallic-Functionalized Interfaces for Highly Efficient Inverted Perovskite Solar Cells. *Science* **2022**, *376*, 416–420.
3. Kim, J. Y.; Lee, J.-W.; Jung, H. S.; Shin, H.; Park, N.-G. High-Efficiency Perovskite Solar Cells, *Chem. Rev*. **2020**, *120* (15), 7867–7918.
4. Zarick, H.; Soetan, N.; Erwin, W. R.; Bardhan, R. Mixed Halide Hybrid Perovskites: A Paradigm Shift in Photovoltaics. *J. Mater. Chem. A* **2018**, 6, 5507-5537.
5. Zhang, Y.; Grancini, G.; Feng, Y. Q.; Asiri, A. M.; Nazeeruddin, M. K. Optimization of Stable Quasi-Cubic $FA_{(x)}MA_{(1-x)}PbI_{(3)}$ Perovskite Structure for Solar Cells with Efficiency beyond 20%. *ACS Energy Lett*. **2017**, *2*, 802−806.
6. Grüninger, H.; Bokdam, M.; Leupold, N.; Tinnemans, P.; Moos, R.; De Wijs, G. A.; Panzer, F.; Kentgens, A. P. M. Microscopic (Dis)order and Dynamics of Cations in Mixed FA/MA Lead Halide Perovskites. *J. Phys. Chem. C* **2021**, *125*, 1742−1753.
7. Knight, A. J.; Herz, L. M. Preventing Phase Segregation in Mixed-Halide Perovskites: A Perspective. *Energy Environ. Sci*. **2020**, *13*, 2024−2046.
8. Singh, S.; Laxmi; Kabra, D. Defects in Halide Perovskite Semiconductors: Impact on Photo-Physics and Solar Cell Performance. *J. Phys. D Appl. Phys.* **2020**, *53* (50), 503003.
9. Kang, J.; J, Li; S.-H. Wei. Atomic-scale Understanding on the Physics and Control of Intrinsic Point Defects in Lead Halide Perovskites. *Appl. Phys. Rev*. **2021**, *8*, 031302.
10. Jin, H.; Debroye, E.; Keshavarz, M.; Scheblykin, I. G.; Roeffaers, M. B. J.; Hofkens, J.; Steele, J. A. It's a Trap! On the Nature of Localised States and Charge Trapping in Lead Halide Perovskites. *Mater. Horiz*. **2020**, *7* (2), 397−410.
11. deQuilettes, D. W.; Frohna, K.; Emin, D.; Kirchartz, T.; Bulovic, V.; Ginger, D. S.; Stranks, S. D. Charge-Carrier Recombination in Halide Perovskites: Focus Review. *Chem. Rev*. **2019**, *119* (20), 11007−11019.
12. Stranks, S. D. Nonradiative Losses in Metal Halide Perovskites. *ACS Energy Lett*. **2017**, *2*, 1515-1525.

13. Sherkar, T. S.; Momblona, C.; Gil-Escrig, L.; Avila, J.; Sessolo, M.; Bolink, H. J.; Koster, L. J. A. Recombination in Perovskite Solar Cells: Significance of Grain Boundaries, Interface Traps, and Defect Ions. *ACS Energy Lett*. **2017**, *2* (5), 1214−1222.
14. Chu, Z.; Yang, M.; Schulz, P.; Wu, D.; Ma, X.; Seifert, E.; Sun, L.; Li, X.; Zhu, K.; Lai, K. J. Impact of Grain Boundaries on Efficiency and Stability of Organic-Inorganic Trihalide Perovskites. *Nat. Commun*. **2017**, *8*, 2230.
15. Wen, X.; Ho-Baillie, A.; Huang, S.; Sheng, R.; Chen, S.; Ko, H.-C.; Green, M. A. Mobile Charge-Induced Fluorescence Intermittency in Methylammonium Lead Bromide Perovskite. *Nano Lett*. **2015**, *15*, 4644−4649
16. deQuilettes, D. W.; Jariwala, S.; Burke, S.; Ziffer, M. E.; Wang, J. T.-W.; Snaith, H. J.; Ginger, D. S. Tracking Photoexcited Carriers in Hybrid Perovskite Semiconductors: Trap-Dominated Spatial Heterogeneity and Diffusion. *ACS Nano* **2017**, *11* (11), 11488−11496.
17. Merdasa, A.; Tian, Y.; Camacho, R.; Dobrovolsky, A.; Debroye, E.; Unger, E. L.; Hofkens, J.; Sundström, V.; Scheblykin, I. G. "Supertrap" at Work: Extremely Efficient Nonradiative Recombination Channels in $MAPbI_3$ Perovskites Revealed by Luminescence Super-Resolution Imaging and Spectroscopy. *ACS Nano* **2017**, *11*, 5391− 5404.
18. Jones, T. W.; Osherov, A.; Alsari, M.; Sponseller, M.; Duck, B. C.; Jung, Y.-K.; Settens, C.; Niroui, F.; Brenes, R.; Stan, C. V.; Li, Y.; AbdiJalebi, M.; Tamura, N.; Macdonald, J. E.; Burghammer, M.; Friend, R. H.; Bulovic, V.; Walsh, A.; Wilson, G. J.; Lilliu, S.; Stranks, S. D. Lattice Strain Causes Non-Radiative Losses in Halide Perovskites. *Energy Environ. Sci*. **2019**, *12*, 596−606.
19. Jariwala, S.; Sun, H.; Adhyaksa, G. W. P.; Lof, A.; Muscarella, L. A.; Ehrler, B.; Garnett, E. C.; Ginger, D. S. Local Crystal Misorientation Influences Non-Radiative Recombination in Halide Perovskites. *Joule* **2019**, *3*, 3048−3060.
20. Gerhard, M.; Louis, B.; Camacho, R.; Merdasa, A.; Li, J.; Kiligaridis, A.; Dobrovolsky, A.; Hofkens, J.; Scheblykin, I. G. Microscopic Insight into Non-Radiative Decay in Perovskite Semiconductors from Temperature-Dependent Luminescence Blinking. *Nat. Commun*. **2019**, *10*, 1698.
21. Yuan, H.; Debroye, E.; Bladt, E.; Lu, G.; Keshavarz, M.; Janssen, K. P.; Roeffaers, M. B.; Bals, S.; Sargent, E. H.; Hofkens, J. Imaging Heterogeneously Distributed Photo-Active Traps in Perovskite Single Crystals. *Adv. Mater*. **2018**, *30*, 1705494.

22. Ledinsky, M.; Vlk, A.; Schönfeldova, T.; Holovsky, J.; Aydin, E.; Dang, H. X.; Hajkova, Z.; Landova, L.; Valenta, J.; Fejfar, A.; De Wolf, S. Impact of Cation Multiplicity on Halide Perovskite Defect Densities and Solar Cell Voltages, *J. Phys. Chem. C* **2020**, *124*, 27333−27339.
23. Vacha, M.; Sharma, D. K.; Hirata, S. Single-Molecule Studies beyond Optical Imaging: Multi-Parameter Single-Molecule Spectroscopy. *J. Photochem. Photobiol. C* **2018**, *34*, 121-136.
24. Li, C.; Zhong, Y.; Luna, C. A.; Unger, T.; Deichsel, K.; Gräser, A.; Köhler, J.; Köhler, A.; Hildner, R.; Huettner, S. Emission Enhancement and Intermittency in Polycrystalline Organolead Halide Perovskite Films. *Molecules* **2016**, *21*, 1081.
25. Draguta, S.; Thakur, S.; Morozov, Y. V.; Wang, Y.; Manser, J. S.; Kamat, P. V.; Kuno, M. Spatially Non-Uniform Trap State Densities in Solution-Processed Hybrid Perovskite Thin Films. *J. Phys. Chem. Lett*. **2016**, *7*, 715−721.
26. Sharma, D. K.; Hirata, S.; Vacha, M. Single-Particle Electroluminescence of $CsPbBr_3$ Perovskite Nanocrystals Reveals Particle-Selective Recombination and Blinking as Key Efficiency Factors. *Nat. Commun*. **2019**, *10*, 4499.
27. Pathoor, N.; Halder, A.; Mukherjee, A.; Mahato, J.; Sarkar, S. K.; Chowdhury, A. Fluorescence Blinking Beyond Nanoconfinement: Spatially Synchronous Intermittency of Entire Perovskite Microcrystals. *Angew. Chem. Int. Ed*. **2018**, *57*, 11603−11607.
28. Hou, L.; Zhao, C.; Yuan, X.; Zhao, J.; Krieg, F.; Tamarat, P.; Kovalenko, M. V.; Guo, C.; Lounis, B. Memories in the Photoluminescence Intermittency of Single Cesium Lead Bromide Nanocrystals. *Nanoscale* **2020**, *12*, 6795−6802.
29. Kim, T.; Jung, S. Il.; Ham, S.; Chung, H.; Kim, D. Elucidation of Photoluminescence Blinking Mechanism and Multiexciton Dynamics in Hybrid Organic−Inorganic Perovskite Quantum Dots. *Small* **2019**, *15*, 1900355.
30. Gibson, N. A.; Koscher, B. A.; Alivisatos, A. P.; Leone, S. R. Excitation Intensity Dependence of Photoluminescence Blinking in $CsPbBr_3$ Perovskites Nanocrystals. *J. Phys. Chem. C* **2018**, *122*, 12106–12113.
31. Yarita, N.; Tahara, H.; Saruyama, M.; Kawawaki, T.; Sato, R.; Teranishi, T.; Kanemitsu, Y. Impact of Postsynthetic Surface Modification on Photoluminescence Intermittency in Formamidinium Lead Bromide Perovskite Nanocrystals. J. *Phys. Chem. Lett*. **2017**, *8* (24), 6041−6047.

32. Tian, Y.; Merdasa, A.; Peter, M.; Abdellah, M.; Zheng, K.; Ponseca, C. S.; Pullerits, T.; Yartsev, A.; Sundström, V.; Scheblykin, I. G. Giant Photoluminescence Blinking of Perovskite Nanocrystals Reveals Single-Trap Control of Luminescence. *Nano Lett*. **2015**, *15*, 1603−1608.
33. Yuan, H.; Debroye, E.; Caliandro, G.; Janssen, K. P. F.; van Loon, J.; Kirschhock, C. E. A.; Martens, J. A.; Hofkens, J.; Roeffaers, M. B. J. Photoluminescence Blinking of Single-Crystal Methylammonium Lead Iodide Perovskite Nanorods Induced by Surface Traps. *ACS Omega* **2016**, *1*, 148−159.
34. Seth, S.; Ahmed, T.; Samanta, A. Photoluminescence Flickering and Blinking of Single $CsPbBr_3$ Perovskite Nanocrystals: Revealing Explicit Carrier Recombination Dynamics. *J. Phys. Chem. Lett*. **2018**, *9* (24), 7007−7014.
35. Karimata, I; Tachikawa, T.; In Situ Exploration of the Structural Transition during Morphology- and Efficiency-Conserving Halide Exchange on a Single Perovskite Nanocrystal. *Angew. Chem. Int. Ed*. **2021**, *60* (5) 2548-2553.
36. Yoshimura, H.; Yamauchi, M.; Masuo, S. In Situ Observation of Emission Behavior during Anion-Exchange Reaction of a Cesium Lead Halide Perovskite Nanocrystal at the Single-Nanocrystal Level. *J. Phys. Chem. Lett*. **2020**, *11*, 530−535.
37. Jin, H.; Steele, J. A.; Cheng, R.; Parveen, N.; Roeffaers, M. B. J.; Hofkens, J.; Debroye, E. Experimental Evidence of Chloride-Induced Trap Passivation in Lead Halide Perovskites through Single Particle Blinking Studies. *Adv. Opt. Mater*. **2021**, *9* (23) 2002240
38. Chouhan, L.; Ghimire, S.; Biju, V. Blinking Beats Bleaching: The Control of Superoxide Generation by Photo-Ionized Perovskite Nanocrystals. *Angew. Chem. Int. Ed.* **2019**, *58*, 4875−4879.
39. Trinh, C. T.; Minh, D. N.; Ahn, K. J.; Kang, Y.; Lee, K.-G. Organic-Inorganic $FAPbBr_3$ Perovskite Quantum Dots as a Quantum Light Source: Single-Photon Emission and Blinking Behaviors. *ACS Photonics* **2018**, *5*, 4937−4943.
40. Manser, J. S.; Christians, J. A.; Kamat, P. V. Intriguing Optoelectronic Properties of Metal Halide Perovskites. *Chem. Rev*. **2016**, *116* (21), 12956−13008.
41. Kim, Y.-H.; Cho, H.; Lee, T.-W.; Rogers, J. A. Metal Halide Perovskite Light Emitters. *Proc. Natl. Acad. Sci. U.S.A*. **2016**, *113*, 11694−11702.
42. Chen, B.; Rudd, P. N.; Yang, S.; Yuan, Y.; Huang, J. Imperfections and Their Passivation in Halide Perovskite Solar Cells. *Chem. Soc. Rev*. **2019**, *48*, 3842−3867.

43. Zhang, Y.; Chen, M.; Zhou, Y. Y.; Li, W. H.; Lee, Y. H.; Kanda, H.; Gao, X. X.; Hu, R. Y.; Brooks, K. G.; Zia, R.; Kinge, S.; Padture, N. P.; Nazeeruddin, M. K. The Synergism of DMSO and Diethyl Ether for Highly Reproducible and Efficient $MA_{0.5}FA_{0.5}PbI_3$Perovskite Solar Cells. *Adv. Energy Mater*. **2020**, *10* (29), 2001300.
44. Saliba, M.; Correa-Baena, J. P.; Wolff, C. M.; Stolterfoht, M.; Phung, N.; Albrecht, S.; Neher, D.; Abate, A. How to Make over 20% Efficient Perovskite Solar Cells in Regular (n-i-p) and Inverted (p-i-n) Architectures. *Chem. Mater.* **2018**, *30* (13), 4193−4201.
45. Tian, W.; Cui, R.; Leng, J.; Liu, J.; Li, Y.; Zhao, C.; Zhang, J.; Deng, W.; Lian, T.; Jin, S. Limiting Perovskite Solar Cell Performance by Heterogeneous Carrier Extraction. *Angew. Chem. Int. Ed*. **2016**, *55*, 13067−13071.

Chapter 4

Air-stable mixed cation lead halide perovskite films and microscopic study of their degradation process

4.1 Introduction

Organic-inorganic hybrid perovskite solar cells (PSCs) have attracted considerable attention around the world owing to their excellent semiconducting properties. The progress in power conversion efficiency improvement of the solar cells has been very rapid, overcoming 25% efficiency[1,2] in the last few years. The preparation of high-quality and long-term stable perovskite thin films is the key to obtaining highly efficient and environmentally stable perovskite solar cells. The commonly used technique for the fabrication of the perovskite active layer is one-step spin coating, as the method is simple and easy to control. However, the films often have incomplete surface coverage and poor morphology, which results in nonradiative recombination in the solar cells. So far, solvent engineering including the use of antisolvents has been considered one of the most efficient ways to control the morphology and crystal structure of perovskite materials and obtain highly uniform perovskite film.[3] A mixture of N,N-dimethylformamide (DMF), and dimethyl sulfoxide (DMSO) is a well-known polar solvent for the preparation of perovskite precursor solution. The function of the antisolvent is to remove the high boiling-point solvent DMF and form a transparent intermediate (e.g., $FA_xMA_{(1-x)}I{-}PbI_2{-}DMSO$) from its perovskite precursor solution, which leads to a smooth and uniform perovskite films with fewer pinholes and with good optoelectronic properties.[4]

At the same time, even the most uniform perovskite films have concerns with stability in ambient air. When the fabrication is carried out in an environment with the uncontrolled presence of humidity or air, the perovskite absorber layer is very sensitive to moisture and oxygen and can easily degrade as a result of high humidity either during the fabrication process or during device operation. To solve this problem, PSCs are being prepared mostly inside inert gas-filled gloveboxes to avoid humidity, which potentially increases the solar cell manufacturing costs.[5] Therefore, research into the area of fabricating perovskite films in ambient air is highly desirable.[6-8] In addition, most of the high-performance reported PSCs are based on toxic antisolvents, such as chlorobenzene, methylbenzene, diethyl ether or toluene which is another major issue for the potential commercialization of PSCs. As a solution to both the above issues, the use of acetates including ethyl acetate (EA) as antisolvents[9] has been proposed. EA features relatively low toxicity and low boiling point. During the formation of perovskite grains from the precursor solution under ambient conditions, the high moisture resistance of acetates can reduce

pinholes and achieve complete coverage on the substrate, forming high-quality perovskite films.[7]

So far, great effort has been spent on the improvement of the stability of the PSCs by choice of charge-transporting materials, perovskite compositional engineering, or use of a wide array of additives.[10,11] On the other hand, less attention has been paid to the long-term ambient stability of the perovskite films themselves. In terms of compositional engineering, mixed cation $MA_{1-x}FA_xPbI_3$ with x between 0.3 and 0.8 have shown increased stability due to the optimized tolerance factor.[12] Further, the use of EA antisolvent has been also shown to increase the stability of perovskite films in ambient humidity.[6] Using these approaches, stability of 80 days for devices without sealing in ambient air with controlled humidity has been demonstrated.[13]

Here, we report the preparation of mixed cation perovskite films in the air with long-term stability and characterization of their degradation process by photoluminescence (PL) microscopy and spectroscopy over extended periods of time. PL microscopy has been a powerful tool to find the relationship between nanoscale structure and properties in a variety of perovskite materials[14] including films[15-18] and micro-/nanocrystals.[19,20] We show that $MA_{1-x}FA_xPbI_3$ films with x of 0.3 and 0.5 prepared in air using EA antisolvent are compositionally stable in ambient air for more than a year. The onset of degradation in these films is characterized by in-situ PL spectra which reveal emission of the decomposition intermediates.

4.2 Experimental Section

***Synthesis of mixed MA/FA perovskite films**:*

$MA_{1-x}FA_xPbI_3$ films with x = 0, 0.3 and 0.5 were synthesized as reported before.[15] Prior to the perovskite synthesis, a freshly cleaned microscope cover glass was spin-coated (at 4000 rpm for 40 s) with 40 nm thick layer of PEDOT: PSS (Clevios P AI4083, H. C. Starck) and annealed at 150 °C for 15 min. To prepare the perovskite film on top of the PEDOT:PSS, 1M perovskite precursor solutions were prepared by mixing PbI_2, MAI (methylammonium iodide) and FAI (formamidinium iodide) with molar ratios of 1:1:0, 1:0.7:0.3 and 1:0.5:0.5, respectively, in mixed solvent of DMSO (20%) and DMF (80%) by stirring at 60 °C. The precursor solutions were spin-coated on the substrates at 1000 rpm for 10 s followed by 5000 rpm for 30 s. Antisolvents were applied in the last 10 s of the 5000 rpm spinning, by

dropping either 100 µL of ethyl acetate (EA) or 100 µL of chlorobenzene (CB). The deposition time of the antisolvent was optimized by choosing different pipette tips and adjusting their diameters. The time range between 0.6 s and << 0.1 s was tested, and the optimal deposition time of 0.1 s was used in the film preparation. The films were then annealed at 100 °C for 40 min. The film thickness was around 450 nm, as measured by SEM. Absorption spectra and XRD has been measured to confirm the presence of perovskite in the aged films.

PL microscopy and spectroscopy: The setup for the PL characterization was described previously.[15] Briefly, PL from the perovskite films was measured using an inverted microscope (IX 71, Olympus) with 442 nm *cw* laser excitation. The signal was collected by an oil immersion objective lens (UplanFLN 100×, N.A. 1.3, Olympus) and detected with an electron-multiplying (EM) CCD camera (iXon, Andor Technology) with an exposure time of 30 ms for blinking and of 50 ms for spectral measurements. For the spectral measurements the signal was dispersed using an imaging spectrograph (CLP-50LD, Bunkou Keiki) placed between the microscope and the CCD camera.

4.3 Results and discussion

4.3.1 Structural characterization

The $MA_{1-x}FA_xPbI_3$ films with x = 0, 0.3 and 0.5 were prepared on PEDOT-PSS layer using one-step spin coating followed by the application of the antisolvent, as reported before.[15] The antisolvent application step was optimized with respect to the deposition time. Apart from the EA antisolvent, chlorobenzene (CB) was used as a reference. After annealing the resulting film thickness was on the order of 450 nm. The films were kept in ambient conditions with air humidity ranging between 40% and 60% and in ambient light for prolonged periods of time. The films prepared 12 months ago, 9 months ago, 6 months ago, as well as freshly prepared films were then compared, and their properties examined.

The Figure 4.1 shows photographs of the x = 0, 0.3 and 0.5 films (denoted as FA 0%, FA 30% and FA 50%, respectively) prepared using EA and for comparison the FA 50% film prepared using CB, at different stages of aging. The remaining compositions prepared using CB are shown in Figure 4.2. The size of each sample in the figures is 24 x 24 mm. The FA 0% (EA) , as well as all the CB sample (FA 0% (CB), FA 30% (CB), and FA 50%

(CB) films, show a color change from brown to yellow after 6 months, and further color bleaching as the aging proceeds. Compared to that, the FA 30% (EA) and FA 50% (EA) films keep their original brown color throughout the 12 months period. The effect of aging can be seen as slightly lighter color pattern mainly near the edges of the films but overall, the films retain their original appearance.

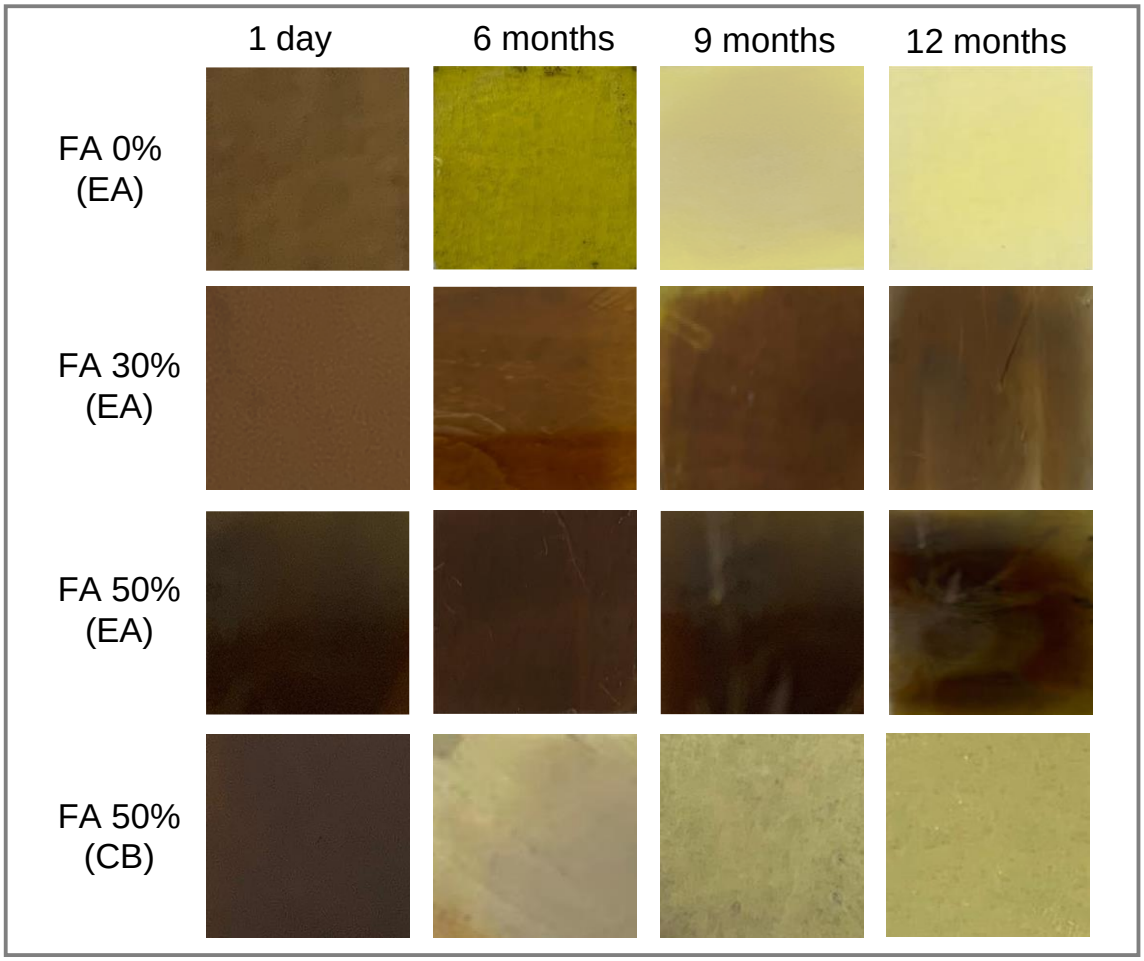

Figure 4.1. Photographs of perovskite films of prepared on 24 x 24 mm microscope cover glass at different stages of aging from 1 day to 12 months. The perovskite compositions and antisolvent used are indicated in the Figure (EA: Ethyl acetate).

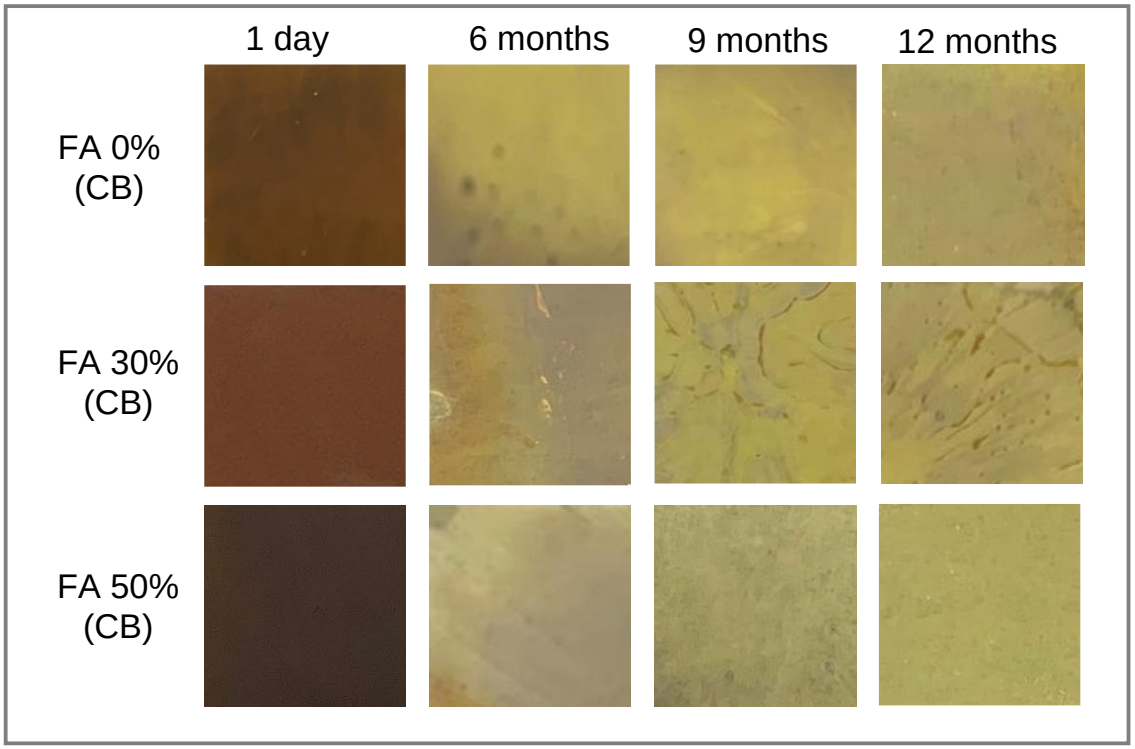

Figure 4.2. Photographs of perovskite films of prepared on 24 x 24 mm microscope cover glass at different stages of aging from 1 day to 12 months. The perovskite compositions and antisolvent used are indicated in the Figure (CB: Chlorobenzene).

To check the corresponding changes in the film morphology we carried out SEM imaging near the center of the films for the FA 0% (EA), FA 30% (EA) and FA 50% (EA) samples, as presented in Figure 4.3. All fresh films show good crystal quality with very few pinholes, which is largely retained for the FA 30% (EA) and FA 50% (EA) after 6 months. In the FA 0% (EA) sample the crystal morphology starts progressively disappearing even after 6 months, and the 12 months sample does not show any of the original film structure. Compared to that, for the FA 30% (EA) and FA 50% (EA) samples the individual crystal grains appear to coalesce into larger ones, but the crystal morphology is still visible even after 12 months, especially in the FA 30% (EA) sample.

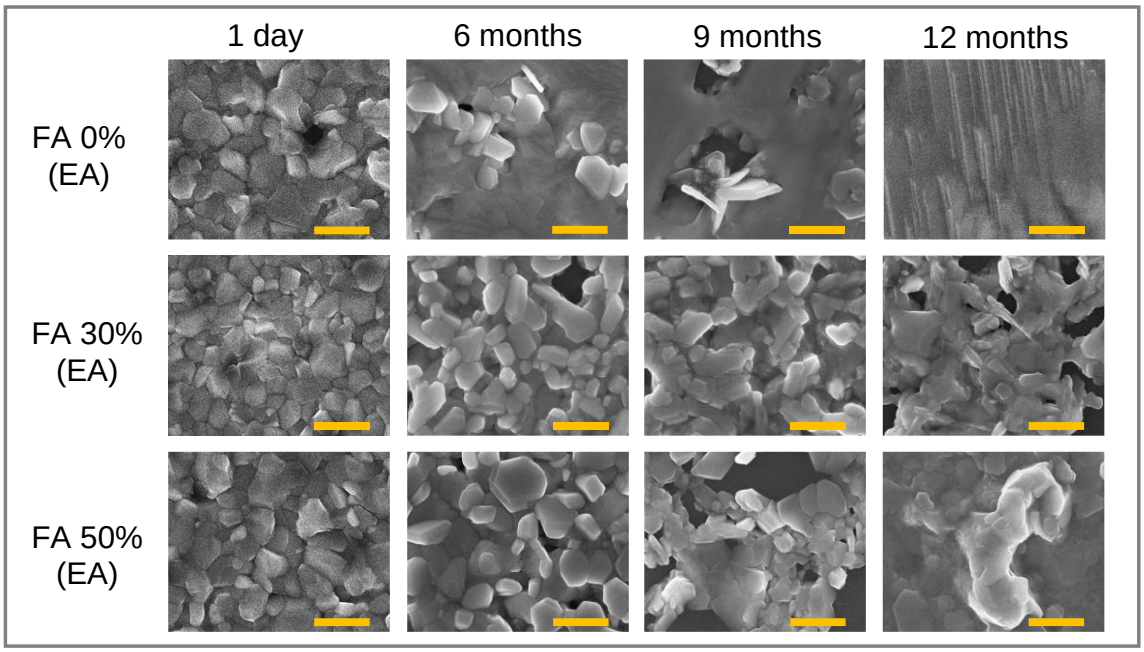

Figure 4.3. SEM images of the perovskite films of different compositions prepared using the EA antisolvent at the same stages of aging as in (a). The images are taken from the centers of the films, the scale bars are 500 nm.

4.3.2 UV-Vis absorption and XRD characterization

To examine changes in the electronic structure of the samples due to aging we have measured the UV–Vis absorption spectra of the FA (0%) films prepared at different stages of aging and compared them with the spectra of PbI_2 film, as shown in the Figure 4.4a.

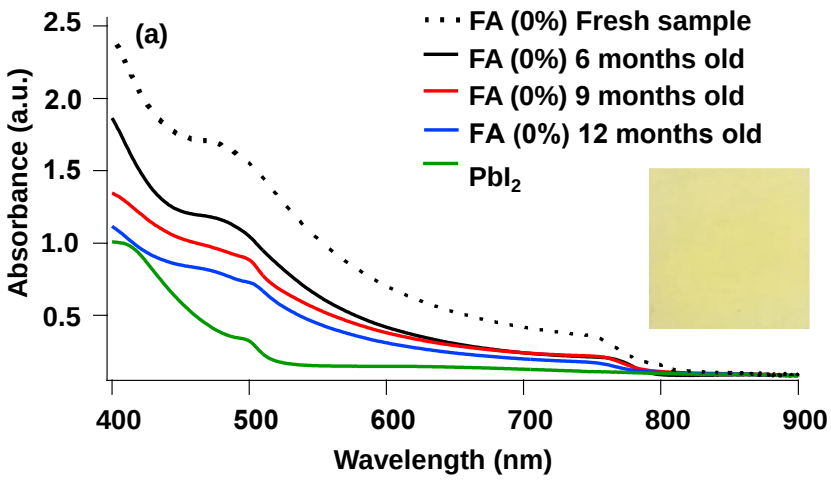

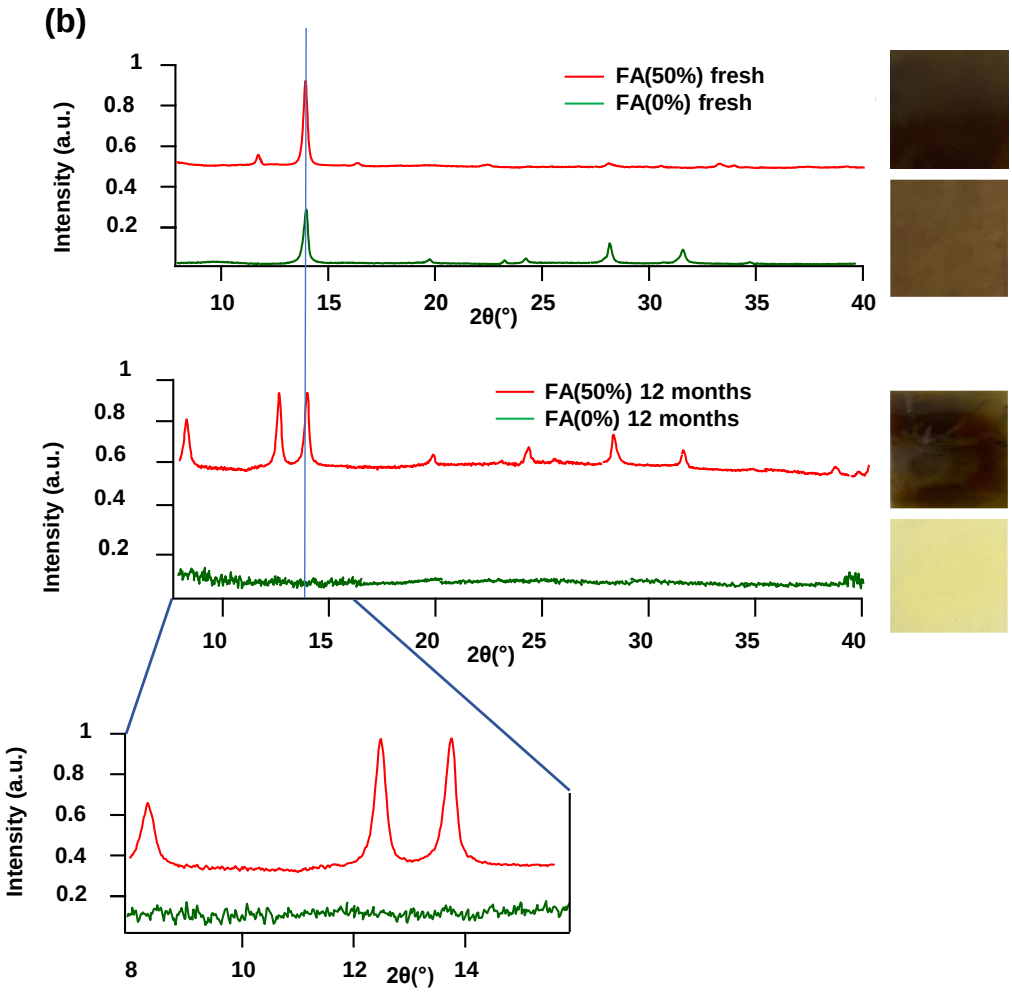

Figure 4.4. (a) Absorption spectra of the FA (0%) films at the different stages of aging; (b) XRD data of the FA(0%) and FA(50%) films for fresh samples (top) and 12 months old samples (bottom).

The absorption spectra show the clear band edge typical of perovskites, even after 12 months. However, the aging caused a gradual decrease of absorbance with time. To get further insight into the structural changes related to aging we measured XRD as shown in Figure 4.4b of the fresh and 12 months old FA(0%) and FA(50%) samples. In the results, we can see that in the fresh samples there are peaks appearing around 14º which is a characteristic perovskite peak. The peaks appearing below ~ 14º in the 12 months old FA(50%) sample could originate from 2D perovskite layers.

4.3.3 Microscopic PL characterization

To study the effect of aging on the compositional stability of the perovskite films we carried out microscopic in-situ PL spectroscopy of the samples. The PL is excited with 442 nm laser and spectra are recorded from diffraction-limited size locations across the films. The results for the 12 months EA samples are shown in Figure 4.5

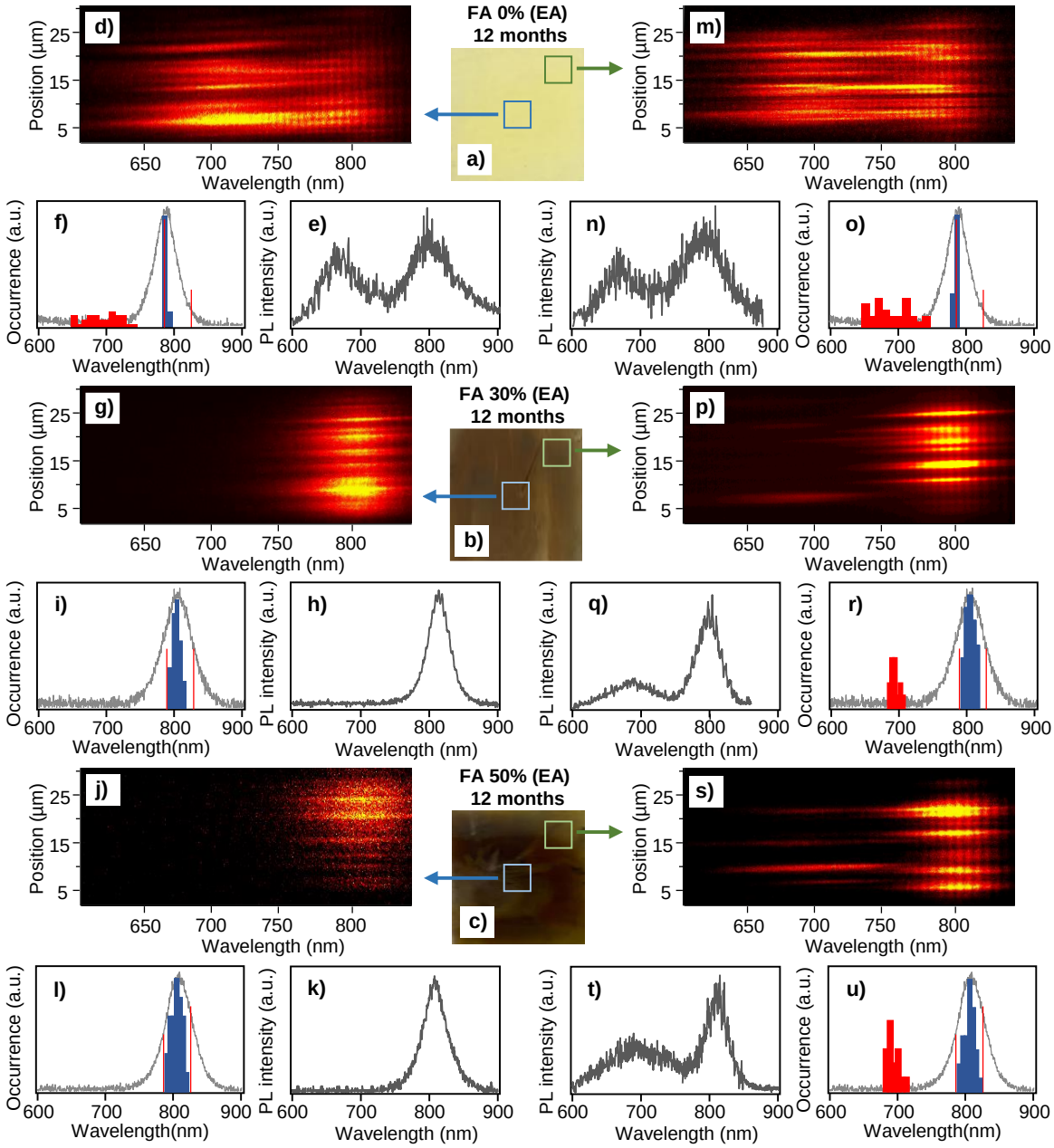

Figure 4.5. Spectroscopic characterization of the degradation process. (a)-(c) Photographs of perovskite films of different compositions as indicated in the Figure taken 12 months after the films fabrication. The squares and arrows indicate symbolically the areas used for

the spectral measurements. (d), (g), (j) Representative 2D PL spectral plots (position vs. wavelength) for central locations in the respective films. (m), (p), (s) Same plots for locations close to the film edges. (e), (h), (k) Examples of typical PL spectra taken in central locations in the respective films. (n), (q), (t) Same PL spectra taken in locations close to the film edges. (f), (i), (l) Histograms of local PL spectral maxima (blue and red bars) measured in central locations in the respective films. The red lines indicate the positions of the distribution peaks for FA 0% and FA 100% samples. Bulk PL spectra of freshly prepared films of the respective composition are shown by solid grey lines. (o), (r), (u) Same histograms obtained from spectra measured in locations close to the film edges.

Here, we measured and analyzed separately the center areas of the films (5 x 5 mm) and the areas close to the edges. The two types of locations are schematically indicated in the photographs of the films in Figure 4.5a-c. For the FA 30% (EA) and FA 50% (EA) samples, the center areas show exclusively spectra corresponding to the mixed cation perovskite phase. Examples of such spectra at different locations in the film spanning more than 25 μm are plotted as 2D spectral plots (position vs. wavelength) in Figure 4.5g, j. These plots show distributions of the PL peaks within the spectral range of the corresponding perovskite composition. Typical PL spectra exhibiting a single peak are shown in Figure 2h, k. We further analyzed the spectral peak positions (by Gaussian fitting) for a statistical sample of locations and plotted their distributions as histograms in Figure 4.5i, l, together with bulk PL spectra of the corresponding freshly prepared films. Both FA 30% (EA) and FA 50% (EA) samples show broad distributions of the local PL spectral peaks, with the distribution maxima corresponding to the bulk PL spectral peaks. The distribution is broader for the FA 50% (EA) sample where it spans a range from 790 nm to 825 nm. This range covers the whole spectral range of all compositions from FA 0% to FA 100%, as reported before.[15] This result is evidence of local compositional heterogeneity of the films and means that the FA 50% (EA) samples contain purely MA domains (FA 0%-like spectra), purely FA domains (FA 100% -like spectra) and domains composed of mixed MA/FA cations of varying ratios. The wavelengths corresponding to the FA 0% and FA100% compositions are marked in the histograms by red lines. Compositional heterogeneity is found in the FA 30% (EA) films as well, but in this case the longest-wavelength components (corresponding to FA100%) are missing in the histogram. We have reported such compositional

heterogeneity for freshly prepared samples before[15] and it is interesting to observe how the heterogeneity evolves with aging of the samples.

Histograms of the PL peak positions for all three samples (FA 0% (EA), FA 30% (EA) and FA 50% (EA)) in the film center areas are shown in Figure 4.6 at different stages of aging, i.e., from fresh to 6 months, 9 months and 12 months. Most interestingly, the wavelength ranges of the distributions for the FA 30% (EA) and FA 50% (EA) samples have not changed over the period of one year, and the shapes of the histograms at different times are also similar. This means that the samples (in their center areas) are compositionally stable for at least one year, and that there is no observable cation migration over this period that would change the shape of the histograms, shift their positions, or cause appearance of FA 100% components in the FA 30% (EA) samples.

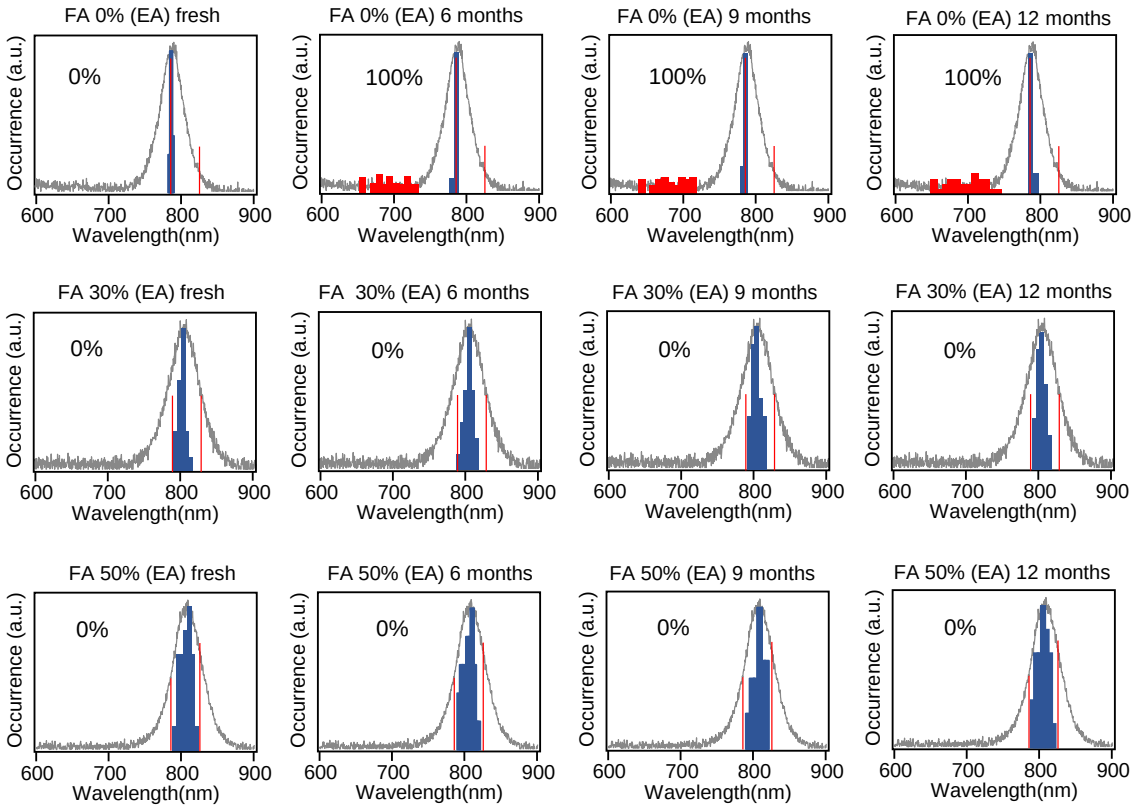

Figure 4.6. Histograms of local PL spectral maxima (blue and red bars) measured in central locations in the respective films at different stages of aging, as indicated in the Figure. The red lines indicate the positions of the distribution peaks for FA 0% and FA 100% samples. Bulk PL spectra of freshly prepared films of the respective composition are shown by solid

grey lines. The percentage numbers indicate the fractions of the degradation product spectra with respect to the spectra of the perovskites.

PL spectral data for center area of the 12 months old FA 0% (EA) sample (which is apparently degraded in the Figure 4.1) are shown in Figure 4.5d-f. The 2D spectral plots as well as the typical PL spectrum show peaks around 785 nm corresponding to pure $MAPbI_3$ perovskite phase from all measured locations. This is a surprising result since in the film appearance and SEM images the sample looks completely degraded. In addition, there are broader PL peaks with higher intensity which are shifted to the blue from the perovskite peaks. Histogram of the PL spectral peaks shown in Figure 4.5f confirms a narrow distribution of the perovskite peaks at 785 nm and broad distribution of the blue-shifted band which spans a range from 641 to 759 nm. We assume that the blue shifted PL originates from products of the degradation process.

Similar features are observed for the PL spectra of all samples taken from the edges of the films. For the FA 30% (EA) and FA 50% (EA) samples (Figure 4.5p-u) the main fraction are PL spectra corresponding to the mixed cation perovskite phase. Distribution of these spectra are similar to those obtained from the center areas and for the FA 50% (EA) sample cover the whole spectral range of all mixed cation compositions. The blue-shifted spectra are distributed between 680 and 711 nm and their fraction is larger for the FA 50% (EA) sample. This result indicated that on microscopic scales there are domains which are compositionally stable as well as domains which are degrading. Since occasionally both types of spectra are observed from the same diffraction limited spot, the size of the domains can be smaller than that, less than ~ 200 nm. The spectral data for the FA 0% (EA) sample (Figure 4.5m-o) closely resemble those of the center area, i.e., show similar narrow distribution of the pure $MAPbI_3$ phase at 785 nm and broad distribution of the blue-shifted peaks between 639 and 758 nm.

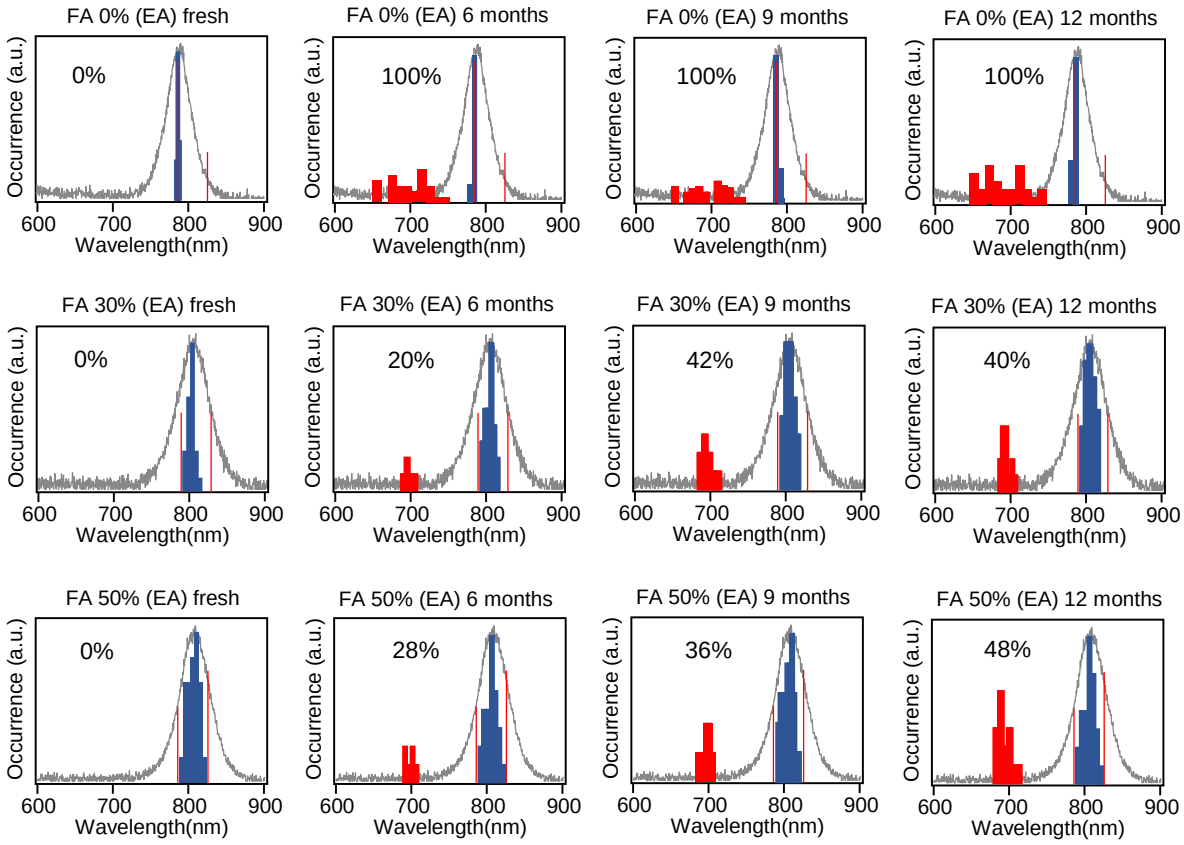

Figure 4.7. Histograms of local PL spectral maxima (blue and red bars) measured in locations close to the edges of the respective films at different stages of aging, as indicated in the Figure. The red lines indicate the positions of the distribution peaks for FA 0% and FA 100% samples. Bulk PL spectra of freshly prepared films of the respective composition are shown by solid grey lines. The percentage numbers indicate the fractions of the degradation product spectra with respect to the spectra of the perovskites.

Evolution of the PL spectral distributions taken from the film edges during the aging process is shown in Figure 4.7. Similar to the center areas, for the FA 30% (EA) and FA 50% (EA) samples the wavelength ranges of the distributions and the peaks of the histograms are mostly stable over the observation period. For the FA 30% (EA) sample we observe slight widening of the histogram without a change of the wavelength range, caused by increased fraction of spectra in the wings of the distributions from fresh to 12 month samples. This points to some degree of the cation migration which leads to an increase of the pure MA phase and corresponding increase of the FA rich phase. In contrast to that, the blue shifted PL is increasing with the aging, in agreement with the assumption that this PL

is due to the degradation product. The fraction of the blue-shifted emission spectra relative to the perovskite spectra is shown as percentage points in the Figures 4.6 and 4.7. In both FA 30% (EA) and FA 50% (EA) samples it is increasing from ~ 20% (in the FA 30% (EA) sample) to close to 50% (in the FA 50% (EA) sample). The evolution of the PL spectra of the FA 0% (EA) sample is similar both at the film center and at its edges. Compared to the mixed cation samples, the fraction of the blue shifted PL is constant with aging after 6 months, i.e., every location examined shows the degradation product spectra.

4.3.4 Proposed mechanism of the degradation process

Studies on the degradation mechanism of perovskite films and solar cells[20-27] commonly conclude that the final product of the degradation is PbI_2 which is formed via several intermediates. PbI_2 as the degradation product has been identified also by low-temperature PL spectroscopy.[28] We attempted to detect the PL from PbI_2 in the spectral range of its peak emission around 520 nm but failed to detect any spectral band that could be identifiable with PbI_2 even with single-molecule level detection sensitivity. The only degradation products we detect in all samples are spectrally located between 632 and 760 nm.

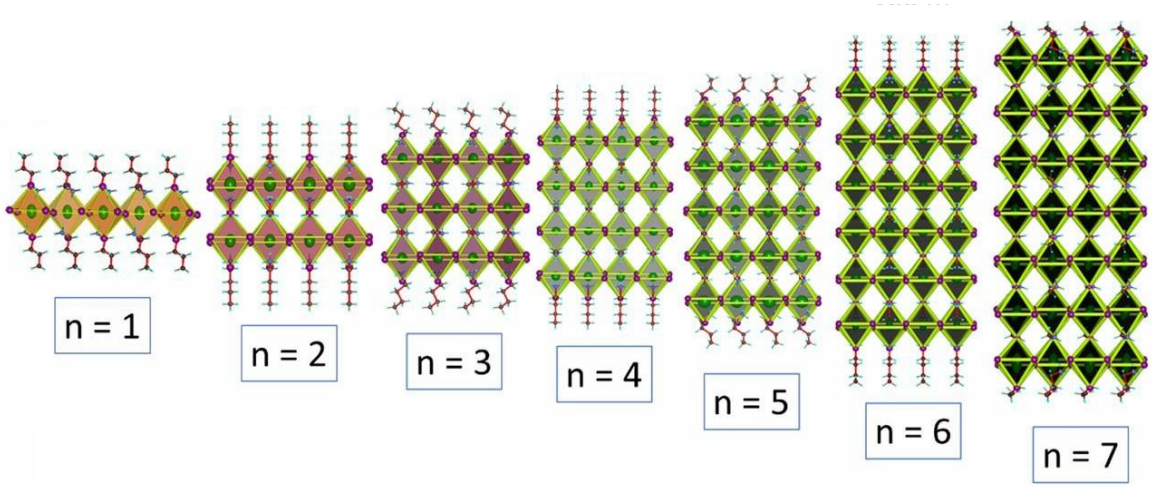

Figure 4.8. Crystal structure of 2D $MA_{n-1}Pb_nI_{3n}$ (n = 1–7) (reproduced from ref. 35 with permission).

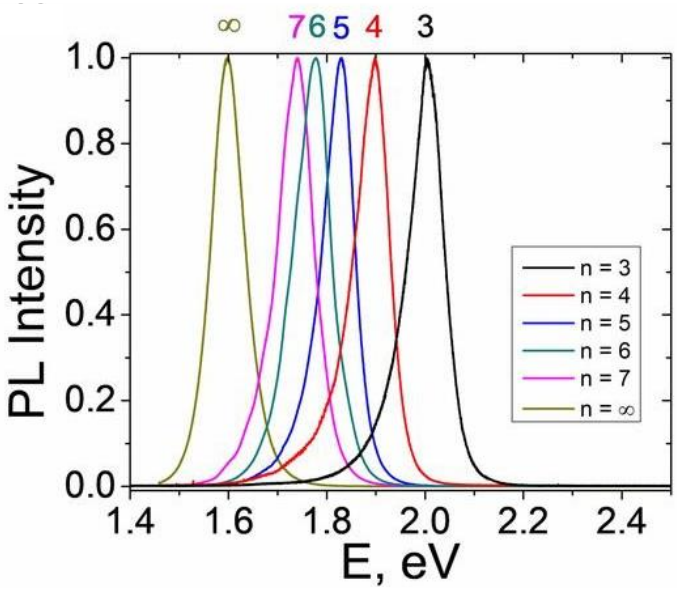

Figure 4.9. PL emission spectra of 2D $MA_{n-1}Pb_nI_{3n}$ series (n = 3–7, ∞) (reproduced from ref. 35 with permission).

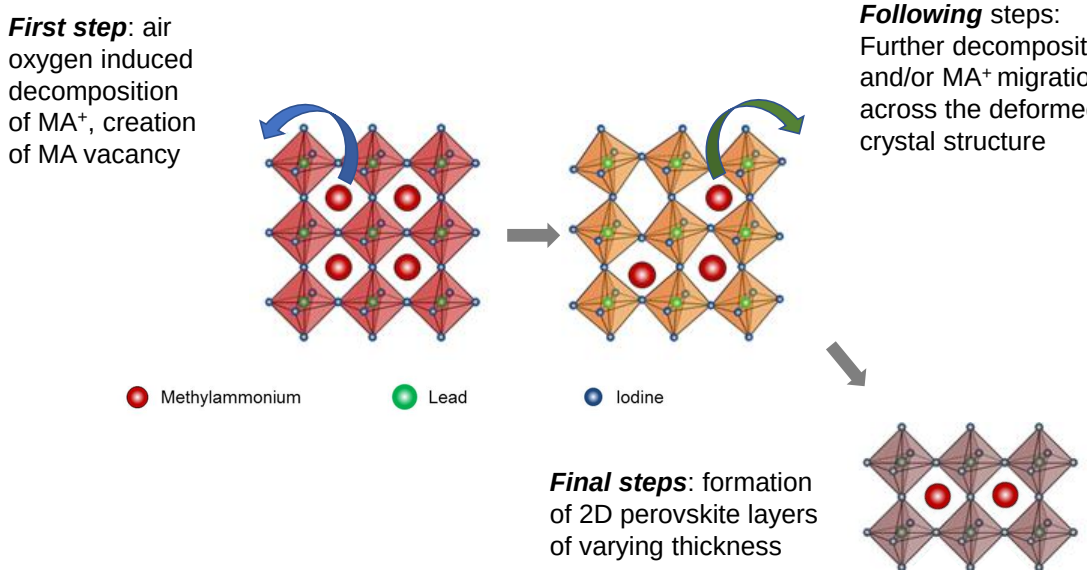

Figure 4.10. Schematic mechanism of the 3D perovskite degradation. Initially, oxygen induced degradation of an MA^+ ion creates a MA vacancy (top left). Degradation proceeds by MA^+ migration into the created vacancies or by further MA^+ decomposition (top right). As a result, 2D layered perovskite of varying thickness is formed in the degraded location in the film (modified from ref. 38 with permission).

Blue shifted PL spectra in similar spectral range as that observed here have been reported before. The appearance of PL in a broad range between 600 and 760 nm during the formation of $MAPbI_3$ films[29,30] was explained by initial growth of small nanocrystals which continue to form the films by Ostwald ripening.[29] Quantum confinement in $MAPbI_3$ nanocrystals has been shown to produce PL with emission peak between 650 and 760 nm.[31] However, in our films we have not observed any nanocrystal formation with aging in the SEM images – on contrary, the crystal grains tend to coalesce and form larger structures. The origin of the blue shifted emission due to quantum confinement in nanocrystals is thus unlikely. Alternatively, blue-shifted PL has been ascribed to emission of trap sites at the interface between PbI_2 and $MAPbI_3$.[32] Such PL has been shown to disappear with increasing excitation intensity, but in our case we do not observe any intensity dependence of the ratio of the blue-shifted and perovskite PL, and thus we exclude the trap origin of the blue-shifted PL.

Most likely candidates for the degradation intermediates that give rise to the blue-shifted PL are 2D-layered perovskite sheets.[33,34] The structures of the 2D analogues (obtained from high-resolution X-ray analysis) of the 3D perovskite $MAPbI_3$ are schematically shown in the Figure 4.8 for the number of layers n = 1 ~ 7. It has been known that the 2D perovskites work as quantum wells with quantum confinement effective in 1 dimension, and that depending on the 2D sheet thickness (given by the number of layers) the PL spectral peaks can vary between 525 and 713 nm.[35-37] The Figure 4.9 shows PL spectra of the 2D perovskite series of n = 1 ~ 7 with the structure presented in Figure 4.8. The spectral range of 680 nm ~ 711 nm of the blue-shifted degradation product in the mixed cation samples (FA 30% (EA) and FA 50% (EA) samples) in our study corresponds to the spectral range of the emission of 2D perovskite sheets with 5 to 7 layers.[35] The possible mechanism of formation of the 2D perovskite phases could be local cation migration which was proposed as an explanation of spectral blue shift in $MAPbI_3$ nanocrystals,[38] as shown in Figure 4.10. It is plausible that the slow cation migration over the long periods of time leads to stabilized 2D sheets of this size. On the other hand, spectral range of 632 nm ~ 760 nm of the degradation product of FA 0% (EA) samples points to much wider distribution of the 2D sheet thickness from 3 (or 4) to 7 layers. The longer-wavelength part of the distribution (up to 760 nm) cannot be explained by known 2D perovskite emission but could originate from the sheet edges.[39]

Degradation of perovskite films in environment with high humidity has been shown to proceed via hydration intermediates, including monohydrate $CH_3NH_3PbI_3 \cdot H_2O$ and dihydrate $(CH_3NH_3)_4PbI_6 \cdot 2H_2O$.[40,41] Structurally, the monohydrate is a 1D perovskite and we looked into the possibility if this phase could be the origin of the blue-shifted PL. PL spectra of a closely related 1D perovskite crystal have been reported recently.[42,43] The PL bands are indeed blue-shifted from the 3D perovskites but their maxima appear around 600 nm at room temperature, at far shorter wavelength than the degradation products observed here. Perovskite hydrates are thus unlikely the origin of the blue shifted emission in the aged perovskite films.

4.3.5 Effect of aging on PL blinking

We have previously reported on a series of mixed MA/FA perovskite films that samples of the FA 30% and FA 50% compositions prepared using EA antisolvent show the least amount of dynamic PL quenching, as observed in the form of potential PL intensity loss in PL blinking from individual nanoscale locations in the films.[15] We have also found on the same samples that PL blinking from different locations separated by a few μm can be highly correlated. Assuming a common quencher which is repeatedly activated and deactivated, the correlated blinking points to very efficient charge migration over micrometer scale distances in the films. In the case of the FA 30% and FA 50% samples such efficient charge migration was happening across multiple grain boundaries which do not present a barrier to the transport.[15] It is interesting to verify how the film aging affects these nanoscale photophysical properties of the films. Potential PL intensity loss analyzed from a statistical sample of film locations is presented in the form of histogram for 12 months old films of the FA 30% (EA) and FA 50% (EA) samples in the Figure 4.11a, b. In both samples the distribution peak is around 20% intensity loss value, with the distribution of the FA 50% (EA) sample being narrower. For comparison, the Figure 4.11c, d shows PL intensity loss distributions for freshly prepared films of the same samples. The peaks of these distributions are around the same 20% loss values, and the distribution of the FA 50% sample is also narrower compared to the FA 30% sample. For reference, the Figure 4.11e explains the definition of the potential PL intensity loss from the blinking traces. We can thus conclude that the film aging does not lead to an increase in the dynamic PL quenching.

Comparison of the PL blinking traces from different locations in the films together with the locations indicated in PL images is shown in the Figure 4.11f, g for the FA 30% (EA) sample and in the Figure 4.11h, i for the FA 50% (EA) sample. In both samples there are locations (denoted by numbers 1 – 3) which are separated by several µm but which show highly correlated PL blinking behavior. In concrete terms, for the FA 30% (EA) film the distances between spots 1 and 2, and those between 1 and 3 are 2.4 µm and 1.8 µm, respectively, and the corresponding Pearson's coefficients calculated for the blinking traces are 0.73 and 0.75. The distances for the 1-to-2 and 1-to-3 locations in the FA 50% (EA) film are 2.1 µm and 2.5 µm, and the Pearson's coefficients are 0.77 and 0.76, respectively. As in the case of the results previously reported on freshly prepared films,[15] these values indicate very efficient charge migration over micrometer scales, similar to what has been observed before on trihalide perovskite films.[43] On average the Pearson's coefficients are even higher than those for the freshly prepared films, which might reflect the partial coalescing of the crystal grains as seen in the SEM images.

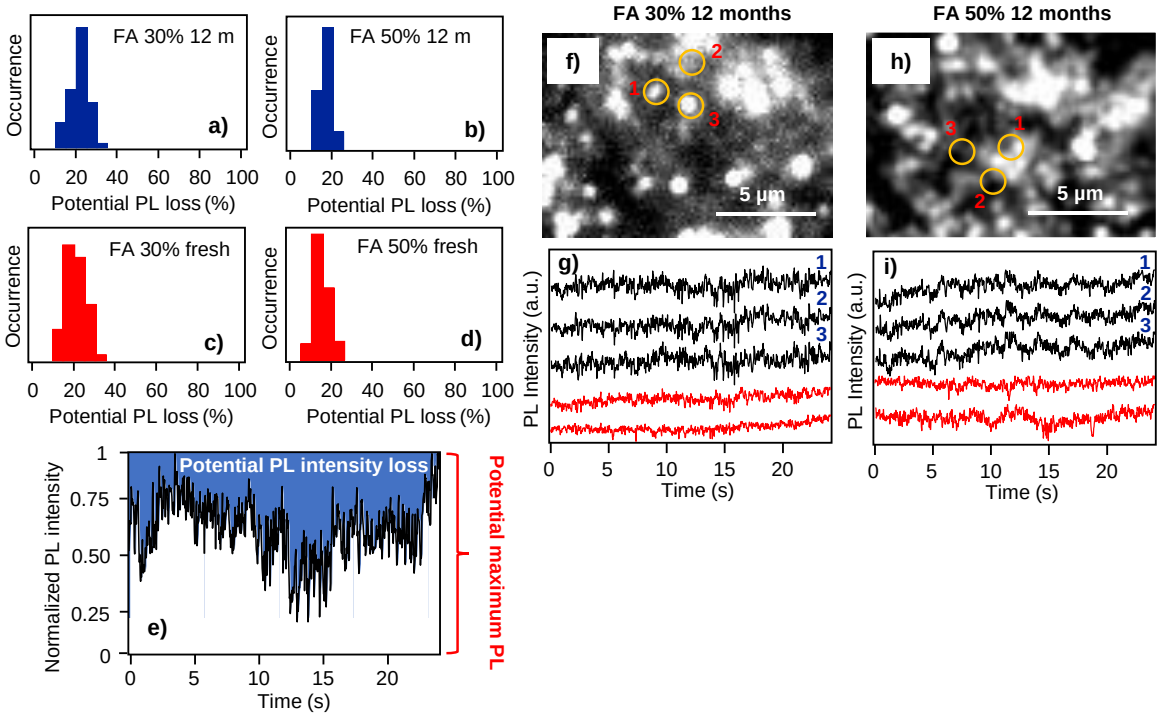

Figure 4.11. (a), (b) Histograms of the potential PL intensity loss obtained from PL blinking traces measured 12 months after film preparation, for sample compositions as indicated in the Figure. (c), (d) Same for freshly prepared films. (e) Example of a PL blinking trace

indicating schematically the definition of the potential PL intensity loss. (f), (h) Microscopic PL images of the 12 months old films. The numbered circles indicate positions where the blinking was analyzed. (g), (i) PL intensity time traces (blinking) obtained at different locations in the two films, including the positions indicated in (f) and (h).

4.4 Conclusions

In conclusion, we report long-term ambient air stable mixed MA/FA cation perovskite films prepared using ethyl acetate as antisolvent. The films containing 30% and 50% of the FA cation are largely compositionally stable for more than a year as observed from nanoscale PL spectra. In terms of morphology, the films retain their grain structure but show coalescence into larger crystal grains during the aging. The morphology change and aging do not affect the long charge diffusion lengths observed for the freshly prepared samples. Slow cation migration causes partial local degradation of the 3D perovskites, probably into 2D sheets with 5 ~ 7 layers. This process happens near the film edges where the quality of the spin coated film might be lower than in the center. The center area of 5 x 5 mm does not show any signs of compositional degradation.

In contrast, reference mixed cation samples prepared by identical process using chlorobenzene as the antisolvent degrade fast within 6 months. Currently, we have not identified any single factor that would solely be responsible for the long term stability of the FA 30% (EA) and FA 50% (EA) films. It is likely a combination of several factors, including the optimum tolerance factor in the crystal structure of the two compositions, and water-absorbing property of the EA antisolvent which ensures minimum residual water in the films even when prepared in ambient conditions.

4.5 References

1. Min, H.; Lee, D. Y.; Kim, J.; Kim, G.; Lee, K. S.; Kim, J.; Paik, M. J.; Kim, Y. K.; Kim, K. S.; Kim, M. G.; Shin, T. J., Sang, I. S. Perovskite solar cells with atomically coherent interlayers on SnO_2 electrodes. *Nature* **2021**, 598, 444–450.
2. Li, Z.; Li, B.; Wu, X.; Sheppard, S. A.; Zhang, S.; Gao, D.; Long, N. J.; Zhu, Z. Organometallic-functionalized interfaces for highly efficient inverted perovskite solar cells. *Science* **2022**, 376, 416–420.
3. Jeon, N. J.; Noh, J. H.; Kim, Y. C.; Yang, W. S.; Ryu, S.; Seok, S. I. Solvent engineering for high-performance inorganic-organic hybrid perovskite solar cell. *Nat. Mater*. **2014**, 13, 897-903.
4. Taylor, A. D.; Sun, Q.; Goetz, K.P.; An, Q.; Schramm, T.; Hofstetter, Y.; Litterst, M.; Paulus, F.; Vaynzof, Y. A general approach to high-efficiency perovskite solar cells by any antisolvent. *Nat. Commun*. **2021**, 12, 1878
5. Miao, S.; Liu, T.; Du, Y.; Zhou, X.; Gao, J.; Xie, Y.; Shen, F.; Liu, Y.; Cho, Y. 2D Material and Perovskite Heterostructure for Optoelectronic Applications. *Nanomaterials* **2022**, 12, 2100.
6. Troughton, J.; Hooper, K.; Watson, T. M. Humidity resistant fabrication of $CH_3NH_3PbI_3$ perovskite solar cells and modules. *Nano Energy* **2017**, 39, 60–68
7. Zhang, Z.; Luo, X.; Ding, J.; Zhang, J. Preparation of high-quality perovskite thin film in ambient air using ethylacetate as anti-solvent *J. Solid State Chem.* **2019**, 274, 199–206.
8. Jung, K.; Oh, K.; Kim, D. H.; Choi, J. W.; Kim, K. C.; Lee, M. J. Ambient-air fabrication of stable mixed cation perovskite planar solar cells with efficiencies exceeding 22% using a synergistic mixed antisolvent with complementary properties. *Nano Energy* **2021**, 89, 106387
9. Yang, F.; Kapil, G.; Zhang, P.; Hu, Z.; Kamarudin, M. A.; Ma, T.; Hayase, S. Dependence of Acetate-Based Antisolvents for High Humidity Fabrication of $CH_3NH_3PbI_3$ Perovskite Devices in Ambient Atmosphere. *ACS Appl. Mater. Interfaces* **2018**, 10, 16482−16489.
10. Mazumdar, S.; Zhao, Y.; Zhang, X. Stability of Perovskite Solar Cells: Degradation Mechanisms and Remedies. *Frontiers in Electronics* **2021**, 2, 712785

11. Leijtens, T.; Bush, K.; Cheacharoen, R.; Beal, R.; Bowring, A.; McGehee, M. D. Towards enabling stable lead halide perovskite solar cells; interplay between structural, environmental, and thermal stability. *J. Mater. Chem. A* **2017**, 5, 11483–11500
12. Charles, B.; Dillon, J.; Weber, O. J.; Saiful Islam, M.; Weller, M. T. Understanding the stability of mixed A-cation lead iodide perovskites. *J. Mater. Chem. A* **2017**, 5, 22495–22499
13. Bu, T.; Wu, L.; Liu, X.; Yang, X.; Zhou, P.; Yu, X.; Qin,T.; Shi, J.; Wang, S.; Li, S.; Ku, Z.; Peng, Y.; Huang, F.; Meng, Q.; Cheng, Y. B.; Zhong, J. Room Temperature Processing of Inorganic Perovskite Films to Enable Flexible Solar Cells. *Adv. Energy Mater.* **2017**, 7, 1700576.
14. Goetz, K. P.; Taylor, A. D.; Paulus, F.; Vaynzof, J. Shining Light on the Photoluminescence Properties of Metal Halide Perovskites. *Adv. Funct. Mater.* **2020**, 30, 1910004.
15. Agarwal, A.; Omagari, S.; Vacha, M. Nanoscale Structural Heterogeneity and Efficient Intergrain Charge Diffusion in a Series of Mixed MA/FA Halide Perovskite Films. *ACS Energy Lett.* **2022**, 7, 2443−2449.
16. Li, C.; Zhong, Y.; Luna, C. A.; Unger, T.; Deichsel, K.; Gräser, A.; Köhler, J.; Köhler, A.; Hildner, R.; Huettner, S. In situ investigation of light soaking in organolead halide perovskite films. *Molecules* **2016**, 21, 1081.
17. Draguta, S.; Thakur, S.; Morozov, Y. V.; Wang, Y.; Manser, J. S.; Kamat, P. V.; Kuno, M. Au−$CsPbBr_3$ Hybrid Architecture: Anchoring Gold Nanoparticles on Cubic Perovskite Nanocrystals. *J. Phys. Chem. Lett.* **2016**, 7, 715−721.
18. Chauhan, M.; Zhong, Y.; Schötz, K.; Tripathi, B.; Köhler, A.; Huettnerc, S.; Panzer, F. Investigating two-step $MAPbI_3$ thin film formation during spin coating by simultaneous in situ absorption and photoluminescence spectroscopy. *J. Mater. Chem. A* **2020**, 8, 5086–5094.
19. Yuan, H.; Debroye, E.; Bladt, E.; Lu, G.; Keshavarz, M.; Janssen, K. P.; Roeffaers, M. B.; Bals, S.; Sargent, E. H.; Hofkens, J. Imaging Heterogeneously Distributed Photo-Active Traps in Perovskite Single Crystals. *Adv. Mater.* **2018**, 30, 1705494.
20. Merdasa, A.; Bag, M.; Tian, Y.; Källman, E.; Dobrovolsky, A.; Scheblykin, I. G. Spatially Resolved Analysis of Defect Annihilation and Recovery Dynamics in Metal Halide Perovskite Single Crystals. *J. Phys. Chem. C* **2016**, 120, 10711−10719.

21. Kundu, S.; Kelly, T. L. In situ studies of the degradation mechanisms of perovskite solar cells. *EcoMat.* **2020**, 2, 12025.
22. Smecca, E.; Valenzano, V.; Deretzis, I.; Valastro, S.; Carallo, S.; Colella, S.; Mannino, G.; Rizzo, A.; La Magna, A.; Alberti, A. $CsPbBr_3$, $MAPbBr_3$, and $FAPbBr_3$ Bromide Perovskite Single Crystals: Interband Critical Points under Dry N_2 and Optical Degradation under Humid Air. *J. Phys. Chem. C* **2022**, 126, 16825−16833
23. Juarez-Perez, E. J.; Ono, L. K.; Maeda, M.; Jiang, Y.; Hawash, Z.; Qi, Y. Photodecomposition and thermal decomposition in methylammonium halide lead perovskites and inferred design principles to increase photovoltaic device stability. *J. Mater. Chem. A* **2018**, 6, 9604–9612
24. Abdelmageed, G.; Jewell, L.; Hellier, K.; Seymour, L.; Luo, B.; Bridges, F.; Zhang, J. Z.; Carter, S. Effect of film structure on $CH_3NH_3PbI_3$ perovskite thin films' degradation. *Appl. Phys. Lett*. **2016**, 109, 233905
25. Chen, S.; Zhang, X.; Zhao, J,; Zhang, Y.; Kong, G.; Li, Q.; Li, N.; Yu, Y.; Xu, N.; Zhang, J.; Liu, K. Zhao, Q.; Cao, J.; Feng, J.; Li, X.; Qi, J.; Yu, D.; Li, J.; Gao, P. Atomic scale insights into structure instability and decomposition pathway of methylammonium lead iodide perovskite. *Nat. Commun*. **2018**, 9, 4807
26. Song, Z.; Abate, A.; Watthage, S. C.; Liyanage, G. K.; Phillips, A. B.; Steiner, U.; Graetzel, M.; Heben, M. J. Perovskite Solar Cells in Space: Evaluation of Perovskite Solar Cell Hole Transport Material in Space Environment. *Adv. Energy Mater*. **2016**, 6, 1600846
27. Yang, J.; Siempelkamp, B. D.; Liu, D.; Kelly, T. L. The Importance of Moisture in Hybrid Lead Halide Perovskite Thin Film Fabrication. *ACS Nano* **2015**, 9, 1955–1963.
28. Jemli, K.; Diab, H.: Lédée, F.; Trippé-Allard, G.; Garrot, D.; Geffroy, B.; Lauret, J.-B.; Audebert, P.; Deleporte, E. Using Low Temperature Photoluminescence Spectroscopy to Investigate $CH_3NH_3PbI_3$ Hybrid Perovskite Degradation. *Molecules* **2016**, 21, 885.
29. Li, J.; Dobrovolsky, A.; Merdasa, A.; Unger, E. L.; Scheblykin, I. G. Luminescent Intermediates and Humidity-Dependent Room-Temperature Conversion of the $MAPbI_3$ Perovskite Precursor. *ACS Omega* **2018**, 3, 14494−14502.
30. Chauhan, M.; Zhong, Y.; Schötz, K.; Tripathi, B.; Köhler, A.; Huettnerc, S.; Panzer, F. Investigating two-step MAPbI3 thin film formation during spin coating by simultaneous in situ absorption and photoluminescence spectroscopy. *J. Mater. Chem. A* **2020**, 8, 5086– 5094.

31. Zhang, F.; Huang, S.; Wang, P.; Chen, X.; Zhao, S.; Dong, Y.; Zhong, H. PbS Capped $CsPbI_3$ Nanocrystals for Efficient and Stable Light-Emitting Devices Using p–i–n Structures. *Chem. Mater*. **2017**, 29, 3793−3799
32. Merdasa, A.; Kiligaridis, A.; Rehermann, C.; Abdi-Jalebi, M.; Stöber, J.; Louis, B.; Gerhard, M.; Stranks, S. D.; Unger, E. L.; Scheblykin, I. G. Critical Assessment of the Use of Excess Lead Iodide in Lead Halide Perovskite Solar Cells. *ACS Energy Lett*. **2019**, 4, 1370−1378.
33. Li, X.; Hoffman, J. M.; Kanatzidis, M. C. The 2D Halide Perovskite Rulebook: How the Spacer Influences Everything from the Structure to Optoelectronic Device Efficiency. *Chem. Rev.* **2021**, *121*, 2230−2291.
34. Ghimire, S.; Klinke, C. Two-dimensional halide perovskites: synthesis, optoelectronic properties, stability, and applications. *Nanoscale* **2021**, 13, 12394
35. Soe, C. M. M.; Nagabhushana, G. P.; Shivaramaiah, R.; Tsai, H.; Nie, W.; Blancon, J.-C.; Melkonyan, F.; Cao, D. H.; Traoré, B.; Pedesseau, L.; Kepenekian, M.; Katan, C.; Even, J.; Marks, T. J.; Navrotsky, A.; Mohite, A. D.; Stoumpos, C. C.; Kanatzidis, M. G. Structural and thermodynamic limits of layer thickness in 2D halide perovskites. *Proc. Natl. Acad. Sci USA* **2019**, 116, 58–66.
36. Liu, J.; Leng, J.; Wu, K.; Zhang, J.; Jin, S. Observation of Internal Photoinduced Electron and Hole Separation in Hybrid Two-Dimentional Perovskite Films. *J. Am. Chem. Soc.* **2017**, 139, 1432−1435.
37. Wang, W.; Cai, M.; Wu, Y.; Ji, K.; Cheng, B.; Liu, X.; Lv, H.; Dai, S. Defect Healing of $MAPbI_3$ Perovskite Single Crystal Surface by Benzylamine. *Symmetry* **2022**, 14, 1099.
38. Merdasa, A.; Bag, M.; Tian, Y.; Källman, E.; Dobrovolsky, A.; Scheblykin, I. G. Spatially Resolved Analysis of Defect Annihilation and Recovery Dynamics in Metal Halide Perovskite Single Crystals. *J. Phys. Chem. C* **2016**, 120, 10711−10719.
39. Blancon, J.-C.; Tsai, H.; Nie, W.; Stoumpos, C. C.; Pedesseau, L.; Katan, C.; Kepenekian, M.; Soe, C. M. M.; Appavoo, K.; Sfeir, M. Y.; Tretiak, S.; Ajayan, P. M.; Kanatzidis, M. G.; Even, J.; Crochet, J. J.; Mohite, A. D. Theoretical assessment of thermodynamic stability of 2D octane-1,8-diammonium lead halide perovskites. *Science* **2017**, 355, 1288–1292.
40. Leguy, A. M. A.; Hu, Y.; Campoy-Quiles, M.; Alonso, M. I.; Weber, O. J.; Azarhoosh, P.; van Schilfgaarde, M.; Weller, M. T.; Bein, T.; Nelson, J.; Docampo, P.; Barnes, P.

R. F. The reversible hydration of $CH_3NH_3PbI_3$ in films, single crystals and solar cells. *Chem. Mater.* **2015**, 27, 3397−3407.

41. Yang, J.; Siempelkamp, B. D.; Liu, D.; Kelly, T. L. Investigation of CH3NH3PbI3 degradation rates and mechanisms in controlled humidity environments using in situ techniques. *ACS Nano* **2015**, 9, 1955–1963
42. Cheng, X.; Ma, J.; Zhou, X.; Fang, C.; Wang, J.; Li, J.; Wen, X.; Li, D. Optical anisotropy of one-dimensional perovskite $C_4N_2H_{14}PbI_4$ crystals. *J. Phys. Photonics* **2020**, 2, 014008
43. Stranks, S. D.; Eperon, G. E.; Grancini, G.; Menelaou, C.; Alcocer, M. J. P.; Leijtens, T.; Herz, L. M.; Petrozza, A.; Snaith, H. Electron-hole diffusion lengths exceeding 1 micrometer in an organometal trihalide perovskite absorber. *J. Science* **2013**, 342, 341-344.

Chapter 5

Photoluminescence dynamics in mixed (MA/FA) halide perovskite films under the applied electrical field

5.1 Introduction

The rapid development of metal halide-based perovskites (MHPs) solar cells in the past few decades is noticeable, and MHPs are getting more attention due to their advantages such as low-temperature processing, high absorption coefficient, long electron–hole diffusion length, and tunable band gap.[1–4] However, the instability of MHP materials remains a major hurdle that limits the commercialization of the perovskite solar cells, particularly under operating conditions such as illumination and internal electrical bias. Recent literature indicates that ion migration is intrinsic to MHP, and that it contributes to many effects in perovskite materials and devices such as hysteresis, photo-induced giant dielectric constants, photoluminescence (PL) enhancement, degradation, PL blinking and flickering, and so on.[5–15] Ion migration has also been reported to be responsible for the formation of structural defects and eventual degradation of perovskite semiconductors.[6,16–19] Defect states in MHP have been widely discussed in literature because of their direct influence on the carrier lifetime and diffusion length, which are crucial for reaching high efficiency of the MHP-based devices.[20–26] However, the defect states can also be annihilated by ion migration, as demonstrated, e.g., by PL enhancement due to light soaking, or by solar cells efficiency recovery after keeping devices in dark. These seemingly contradictory observations further complicate the overall picture.[27-28] Although substantial efforts have been made to study ion migration under illumination and external electric field (EF),[6–8,13,16,29,30], the underlying fundamental physics concerning nonradiative recombination induced by ion migration remains elusive. A deeper insight into the ion migration effect in MHP, particularly under illumination and external bias, is imperative to solve the instability problem of perovskite-based devices.

Recently, electric field-based experiments on MHP films with lateral electrodes have shown both reversible and irreversible PL quenching, which has been attributed to the formation of traps due to ion migration.[31-32] In most of the experiments, however, perovskite films or crystals were directly in contact with at least one of the electrodes.[6,30–36] This makes direct charge injection and decomposition of the material under the influence of current an important factor for the PL response. Thus, the lack of insulation layers makes it difficult to tell apart the pure effect of the electric field from the effect of current and mass transfer over the device.

Also, in recent advancements in research, a few studies have shown the electric field effect on MA-based perovskite nanocrystals and thin films. However, no particular study has been carried out on mixed cation or MA/FA-based perovskite thin films. In our recent study[37], we found that MA/FA-based perovskite films (in particular, $MA_{0.7}FA_{0.3}PbI_3$ and $MA_{0.5}FA_{0.5}PbI_3$) show promising results in terms of long-term stability and lack of dynamic quenching. Based on these results, here we have chosen to carry out a comparative study of the effect of external electric field on PL dynamics on three samples, including pure $MAPbI_3$, as well as mixed $MA_{0.7}FA_{0.3}PbI_3$ and $MA_{0.5}FA_{0.5}PbI_3$ perovskite films. Further, the difference of our approach from previous studies is that we want to exclude direct charge injection to have a better insight into the electric field-induced PL response. To achieve this, we studied individual sub-micrometer MHP polycrystalline thin film capacitor-like devices with well-insulated electrodes. The PL properties of MA/FA mixed lead iodide perovskite were studied under a constant externally applied electric field to emulate the internal bias present in the working perovskite solar cells. It was found that the PL of $MA_xFA_{1-x}PbI_3$ samples shows various position-dependent responses to the constant electric field, including reversible PL quenching and PL intensity and spectral fluctuations. The various phenomena are discussed in the context of grain boundaries and light-induced ion migration under the effect of the applied electric field. We note that the ability to actively control the PL by electric field can be potentially used in future optoelectronic devices.

5.2 Experimental methods

5.2.1 Sample preparation

Synthesis of mixed MA/FA perovskite films:

$MA_{1-x}FA_xPbI_3$ films with x = 0, 0.3 and 0.5 were synthesized as reported before.()Prior to the perovskite synthesis, a freshly cleaned etched ITO-coated substrate was spin-coated (at 4000 rpm for 40 s) with 40 nm thick layer of PEDOT: PSS (Clevios P AI4083, H. C. Starck) and annealed at 150 °C for 15 min. To prepare the perovskite film on top of the PEDOT:PSS, 1M perovskite precursor solutions were prepared by mixing PbI2 , MAI (methylammonium iodide) and FAI (formamidinium iodide) with molar ratios of 1:1:0, 1:0.7:0.3 and 1:0.5:0.5, respectively, in the mixed solvent of DMSO (20%) and DMF (80%) by stirring at 60 °C. The precursor solutions were spin-coated on the substrates at 1000 rpm for 10 s followed by 5000 rpm for the 30s. Antisolvents were applied in the last 10s of the 5000-rpm spinning, by dropping 100μL of ethyl acetate (EA). The films were then annealed at 100 °C for 40 min. The film thickness was around 450 nm, as measured by SEM.

To fabricate a capacitor-like device, on the top of the perovskite layer 5 wt% toluene solution of poly(methyl methacrylate) (PMMA) was spin-coated to form around 200 nm thick PMMA layer, with the purpose to isolate the perovskite layer from the direct contact with the electrode and to prevent direct charge transfer into the device. Finally, using the vacuum deposition technique 110 nm thick aluminum layer has been coated on top of the PMMA layer. Finally, the sample look like the below Figure: 5.1.

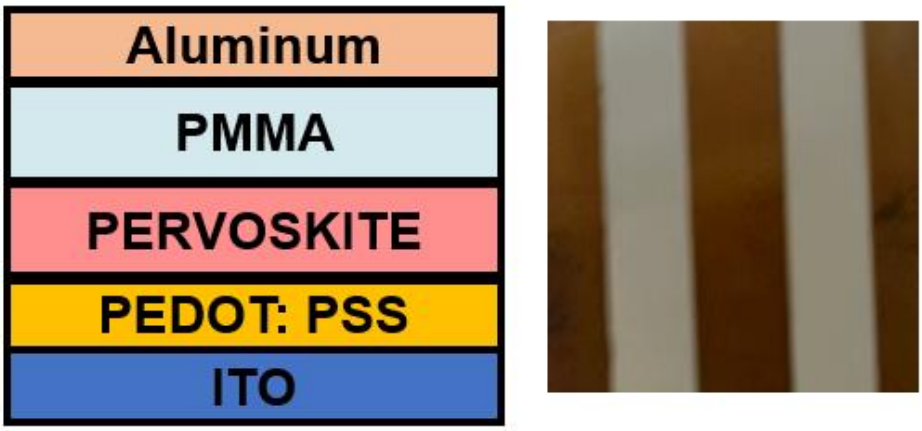

Figure 5.1. Schmatic diagrame of device fabrication

5.2.2 PL microscopy and spectroscopy

The setup for the PL characterization was described previously in Chapter 3. Briefly, PL from the perovskite films was measured using an inverted microscope (IX 71, Olympus) with 442 nm cw laser excitation. The signal was collected by an oil immersion objective lens (UplanFLN 100×, N.A. 1.3, Olympus) and detected with an electron-multiplying (EM) CCD camera (iXon, Andor Technology) with an exposure time of 30 ms for blinking and of 30ms for spectral measurements. For the spectral measurements, the signal was dispersed using an imaging spectrograph (CLP-50LD, Bunkou Keiki) placed between the microscope and the CCD camera.(iXon, Andor Technology).

5.2.3 External electric-field modulation

Constant and waveform electric field across the capacitor-like device was generated using dc voltage provided and controlled by a multimeter (Keithley, Tektronics) and a function generator. Care has been taken that the perovskite layer was electrically isolated and no direct transport of charge occurred in the devices for applied voltages of up to 5V. All measurements were performed in the air at room temperature.

5.3 Result and discussion

As a result of the experimental study of several different positions in each sample we have identified two completely different phenomena: 1. Strong quenching of PL due to the applied field and slow PL recovery after the field removal and, 2. PL intensity fluctuations and PL spectra modulations due to the applied field. Below, we describe the two types of phenomena separately.

5.3.1 PL quenching and recovery

Related to the first phenomenon of PL quenching, the Figure 5.2a shows a typical PL image of a pure $MAPbI_3$ film within the capacitor-like device. (See the Experimental Section). The bright spots presented in this image show individual $MAPbI_3$ crystal grains which are also visible in the corresponding SEM image (Figure 5.2d). We note that the PL and SEM images are taken from different areas of the sample and are not correlated. In the PL image, some crystals were occasionally staying in long-lived off states and were not always visible on PL images. Figures 5.2a-c are the PL images of the same sample location corresponding to the switching of the applied external dc field of 5 V in the sequence 0 V – 5 V – 0 V. We found that PL images were getting dark (PL disappeared) when the voltage was on and were getting again bright (PL reappeared) when the voltage was off. Figure 5.2e shows the PL intensity trace of a randomly selected bright spot in the PL image. In that we can see that PL is quenched when the electric field was applied, and it started to recover when the electric field was switched off. Similarly, Figure 5.2f-h are PL spectra with respect to the switching off-on-off cycle taken along a vertical line position in the same sample location. In Figure 5.2i we have traced one of the PL spectra from Figure 5.2f with respect to time on the scale of 24 s. Similar to the PL images we found that due to the quenching of PL, this spectrum completely disappeared during the active electric field. After removal of the electric field the PL started recovering, but interestingly the PL reappeared in the images quite differently from the original pattern (Figure 5.2a vs. Figure 5.2c). The changes before and after the applied field can be also clearly seen in the spectra.

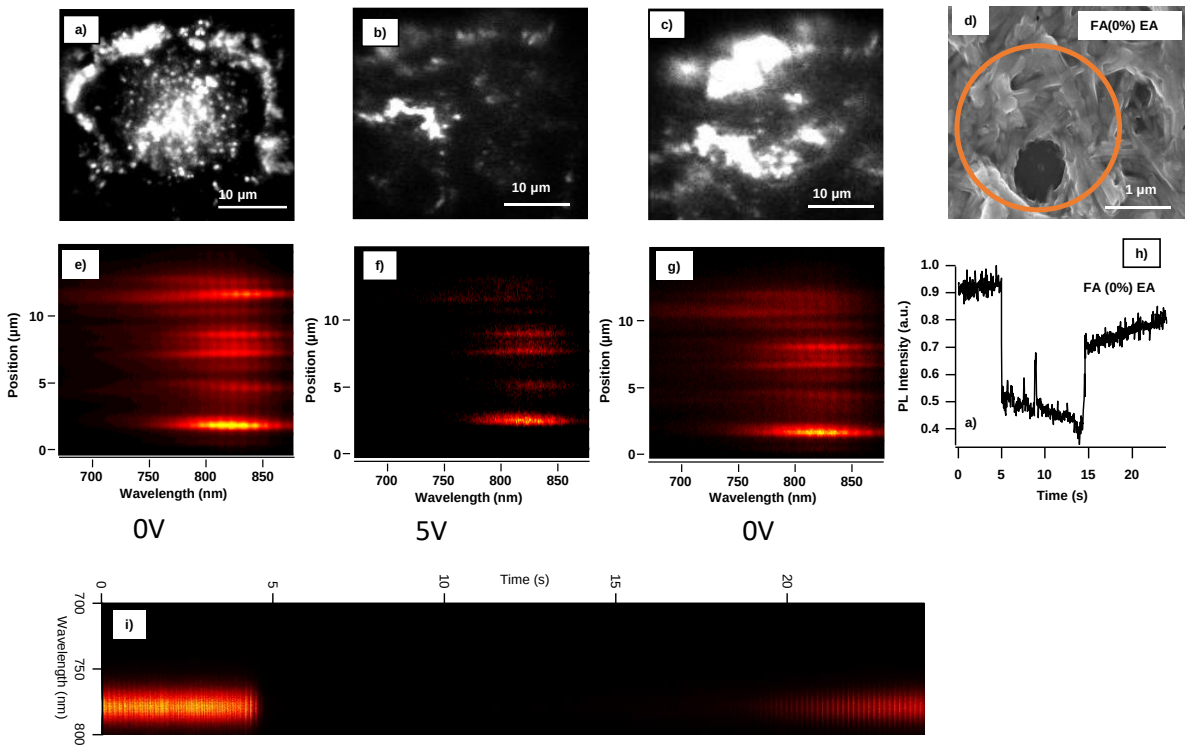

Figure 5.2. PL quenching and recovery of $MAPbI_3$ perovskite sample

Similarly to the Figure 5.2, the Figures 5.3 and 5.4 show the results of the PL quenching and recovery for the $MA_{0.7}FA_{0.3}PbI_3$ and $MA_{0.5}FA_{0.5}PbI_3$ samples, respectively, together with their SEM images. The observed phenomena on these two samples are qualitatively similar to that observed on the pure $MAPbI_3$ film: the PL images were getting dark/disappearing when the voltage was on and were getting brighter/reappearing again when the voltage was off. The recovered PL images were generally different from the original ones, but in the case of the $MA_{0.5}FA_{0.5}PbI_3$ sample the difference was less pronounced (Figure 5.3a vs. 5.3c and Figure 5.4a vs. 5.4c, respectively). Differences in the reappeared PL are also visible in the spectra, again less pronounced for the $MA_{0.5}FA_{0.5}PbI_3$ sample.

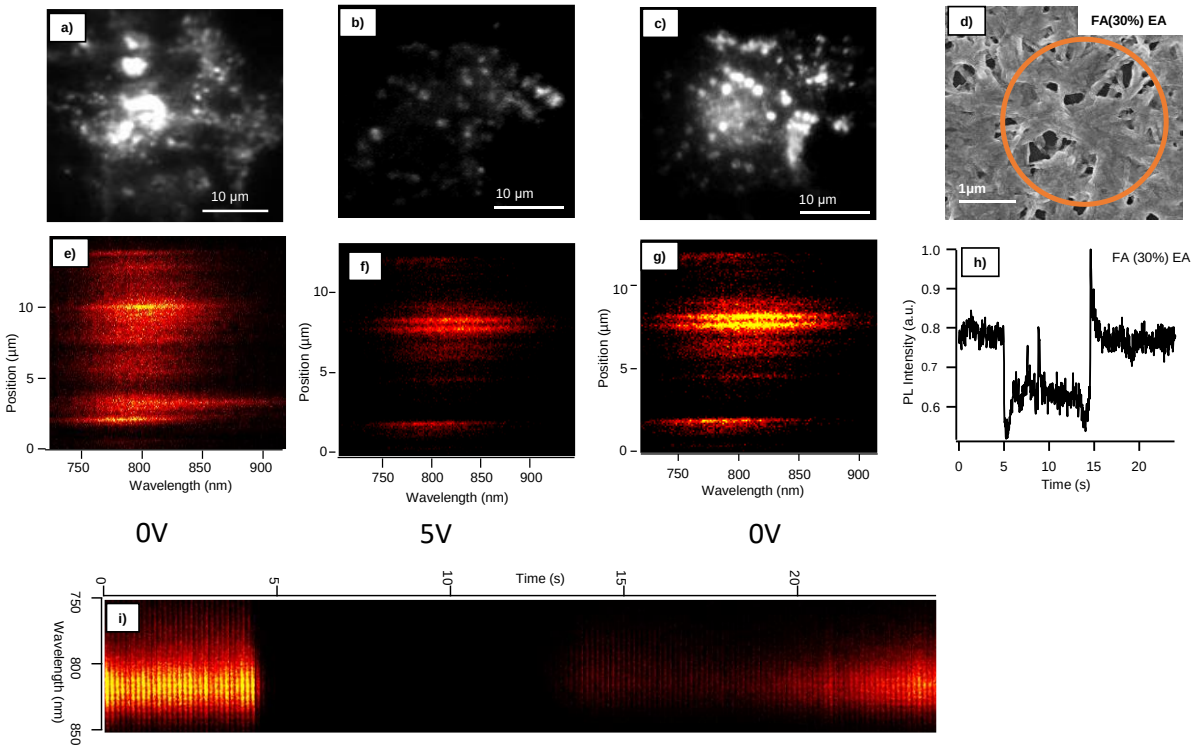

Figure 5.3. PL quenching and recovery of $MA_{0.7}FA_{0.3}PbI_3$ perovskite sample

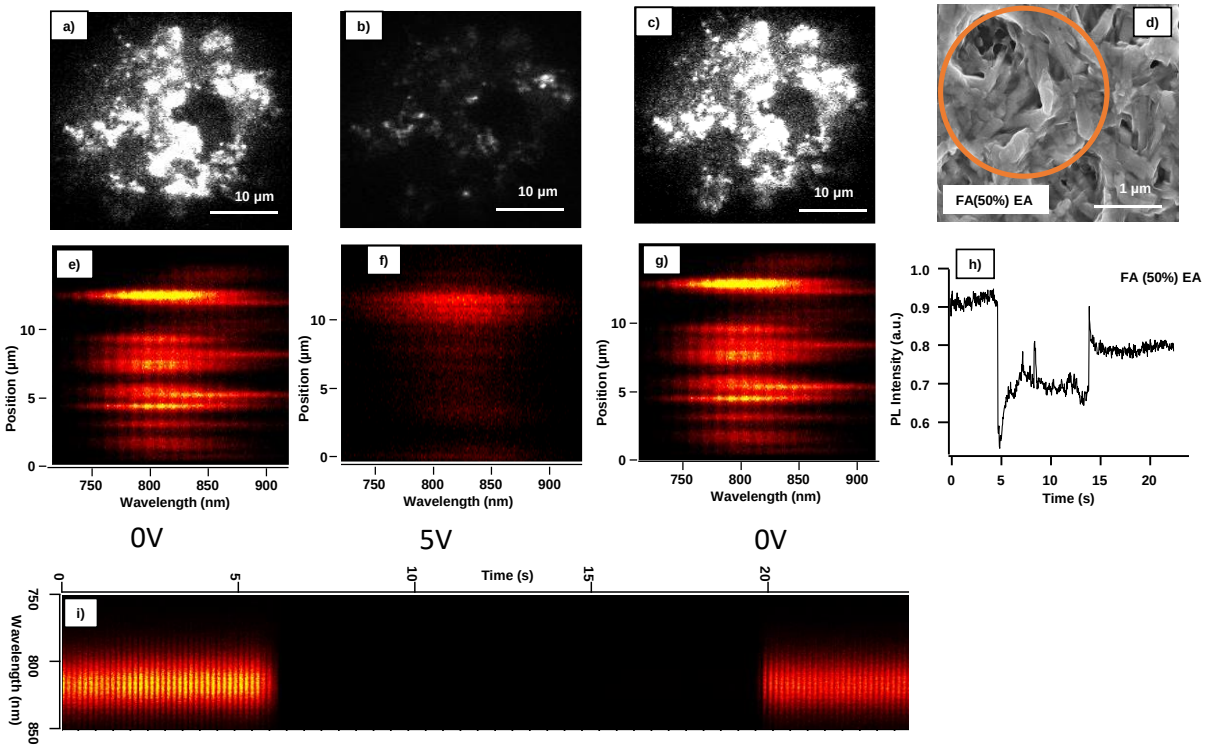

Figure 5.4. PL quenching and recovery of $MA_{0.5}FA_{0.5}PbI_3$ perovskite sample

5.3.2 PL intensity fluctuations

The results of the second phenomenon are shown in Figure 5.5. PL image of the pure $MAPbI_3$ film within the capacitor-like device is shown in the Figure 5.5a and the corresponding SEM image (taken at a different location in the sample and not correlated with the PL image) in the Figure 5.5d. Figures 5.5a-c are the PL images of the same location corresponding to the switching of the applied external dc field of 5 V in the sequence 0 V – 5 V – 0 V. We found that in the images the PL intensity is somewhat decreasing when the voltage is on and increasing again when the voltage is off. However, compared to the phenomenon described in the section 3.1. the relative PL intensity changes due to the applied electric field are smaller. Also, unlike the case of the strong quenching, the PL images before, during and after the applied field are very similar. The Figure 5.5e-g are PL spectra corresponding to the switching off-on-off cycle taken along a vertical line position in the same sample location. Surprisingly, we found that the PL spectra can show either a blue shift or a red shift (within the range of the composition) after the applied voltage is switched off, depending on the position across the sample. Figure 5.5h shows the PL intensity trace of a randomly selected bright spot in the PL images in that we can see that instead of the strong PL quenching the PL intensity is fluctuating when the electric field was applied. We note that these results were obtained on the same sample as those presented in the Figure 5.2. Though the sample is same it is interesting to see two completely different phenomena with respect to different locations using microscopy.

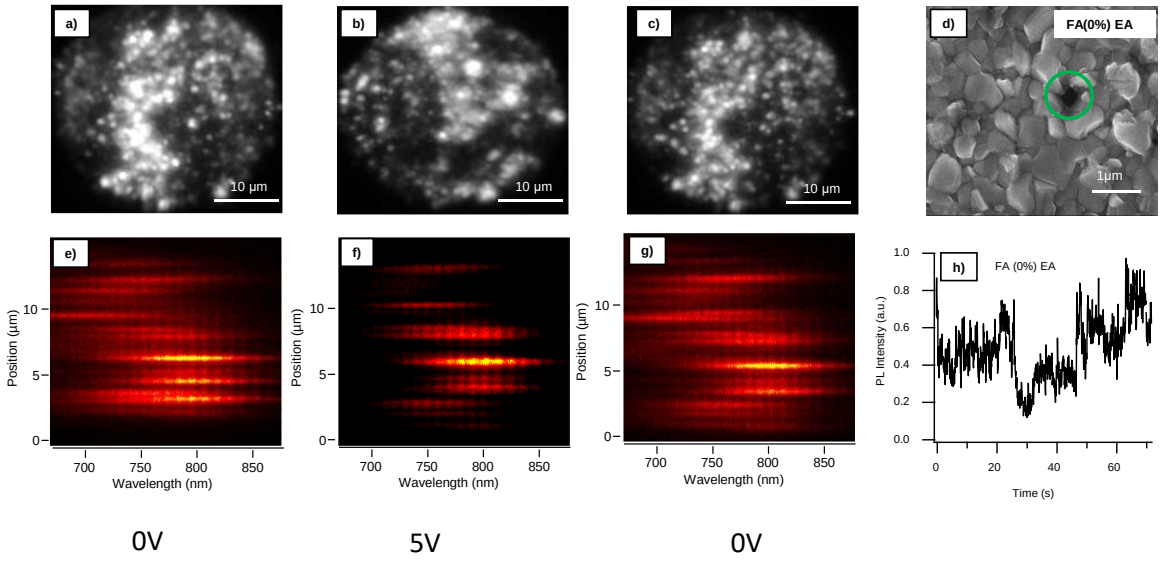

Figure 5.5. PL flickering and recovery of $MAPbI_3$ perovskite sample

Similarly, to the Figure 5.5, the Figures 5.6 and 5.7 show the results of the PL fluctuations for the $MA_{0.7}FA_{0.3}PbI_3$ and $MA_{0.5}FA_{0.5}PbI_3$ samples, respectively, together with their SEM images. The observed phenomena on these two samples are qualitatively similar to that observed on the pure $MAPbI_3$ film.

We reiterate that both the phenomena of PL quenching and PL fluctuations were observed in the same perovskite samples. Within that, the PL quenching is restricted to a very small area in each sample, and it was often difficult to find such area. At the same time, the PL images (Figure 5.2a, 5.3a, 5.4a) show that the PL quenching occurs in a location in the sample which is highly inhomogeneous. This lead us to the assumption that the PL quenching phenomenon occurs around a pinhole or other structural inhomogeneity, and indeed such pinholes (inhomogeneities) can be found in the SEM images (Figure 5.2d, 5.3d, 5.4d On the other hand, the electric-field induced PL fluctuations are a common observation in most of the sample areas. Since the corresponding PL images (Figures 5.5a, 5.6a, 5.7a show a more regular PL distribution (overall dark background with a large number of bright emitting spots) we assume that the PL fluctuation occur in homogeneous parts of the film, characterized by the regular grain structure (as shown in the SEM images in Figure 5.5d, 5.6d, 5.7d).

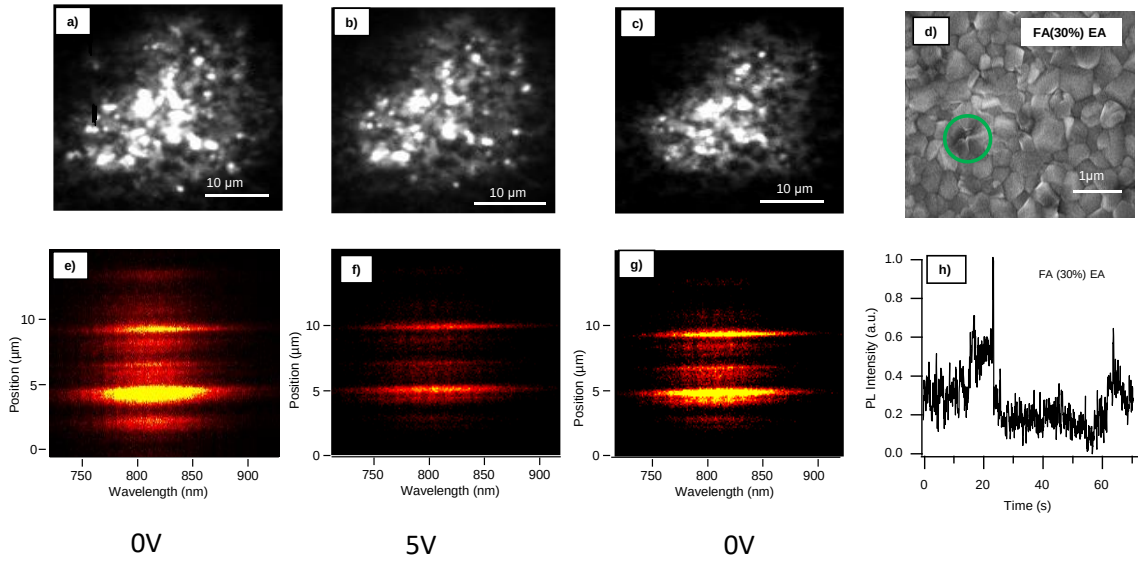

Figure 5.6. PL flickering and recovery of $MA_{0.7}FA_{0.3}PbI_3$ perovskite sample

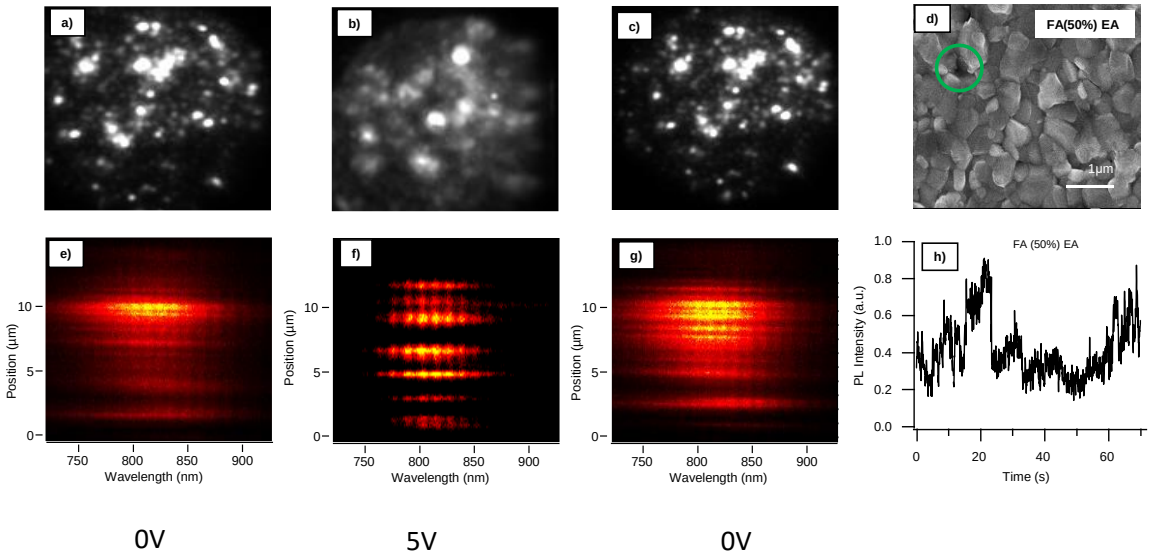

Figure 5.7. PL flickering and recovery of $MA_{0.5}FA_{0.5}PbI_3$ perovskite sample

5.3.3 PL spectral fluctuations

Figure 5.8b-e are the PL spectra of the pure $MAPbI_3$ film at randomly selected spots from the PL image in Figure 5.5e. Evolution of the spectra under the applied voltage of 5 V were monitored over the time of 70 s and the plots are constructed as wavelength vs. time 2D images. We have found that all the PL spectra measured showed intensity and wavelength fluctuations due to the external electric field. For comparison, the Figure 5.8a shows time evolution of a spectrum without the external field applied. The spectrum is stable over the period of the 70 s. In Figure 5.8f we have traced a few examples of PL spectra selected at different time locations with respect to the same spot. All the spectra were fitted with a combination of gaussian functions. Figure 5.8g (spectra 2-4) are PL spectra that show the effect of applied electric field. In addition, Figure 5.8g (spectrum 1) is a PL spectrum without the applied voltage. The Gaussian fitting of the spectra showed that there was an additional, mostly blue shifted, PL spectral peak that appeared in time as a result of the applied electric field. In Figure 5.8h we plotted a histogram of the distribution of all PL spectra peaks from the different spots and at different times. In the histogram, blue bars show the original main PL peak and the newly appeared additional PL peaks are shown in red. We note that the range of the wavelength distribution of both blue and red bars in the histogram falls within the expected distribution of pure $MAPbI_3$ perovskite PL spectra.[38]

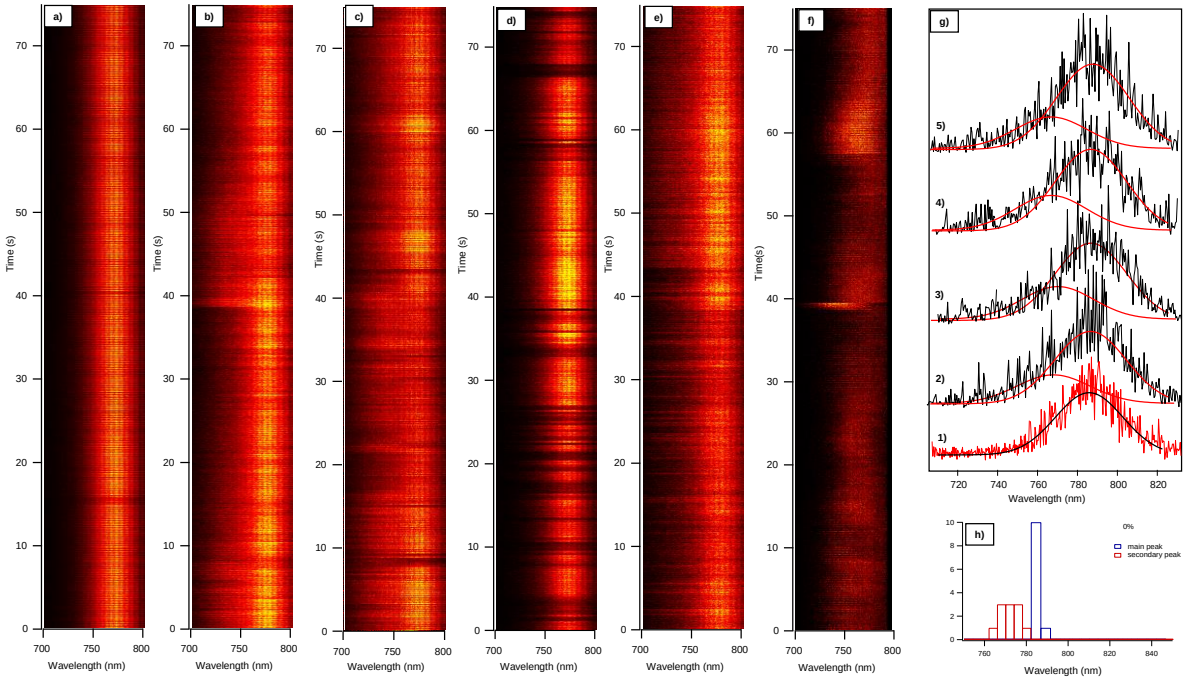

Figure 5.8. Time evolution PL Spectra of $MAPbI_3$ perovskite film. (a) PL spectra without external voltage. (b-f) PL spectra with applied 5V external voltage. (g) 2-4: PL spectra under applied field of 5V taken at different times from the trace (c); 1: PL spectrum without external filed taken from the trace (a). The solid lines are Gaussian fits to the spectra. (h) Histogram of PL spectral peaks analyzed from the traces (b) - (f).

Similar results have been found in Figure 5.9b-e for the $MA_{0.3}FA_{0.7}PbI_3$ samples and in Figure 5.10b-e for the $MA_{0.5}FA_{0.5}PbI_3$ samples. In all time evolution plots of the PL spectra we observe PL intensity and wavelength fluctuations. The gaussian fitting again reveals the appearance of additional blue-shifted PL spectral peaks due to the applied electric field. Compared to the pure $MAPbI_3$ for which the distribution of the additional peaks was centered around 770 nm, the additional peak distributions of the $MA_{0.3}FA_{0.7}PbI_3$ and $MA_{0.5}FA_{0.5}PbI_3$ samples are centered around 780 nm and 790 nm, respectively.

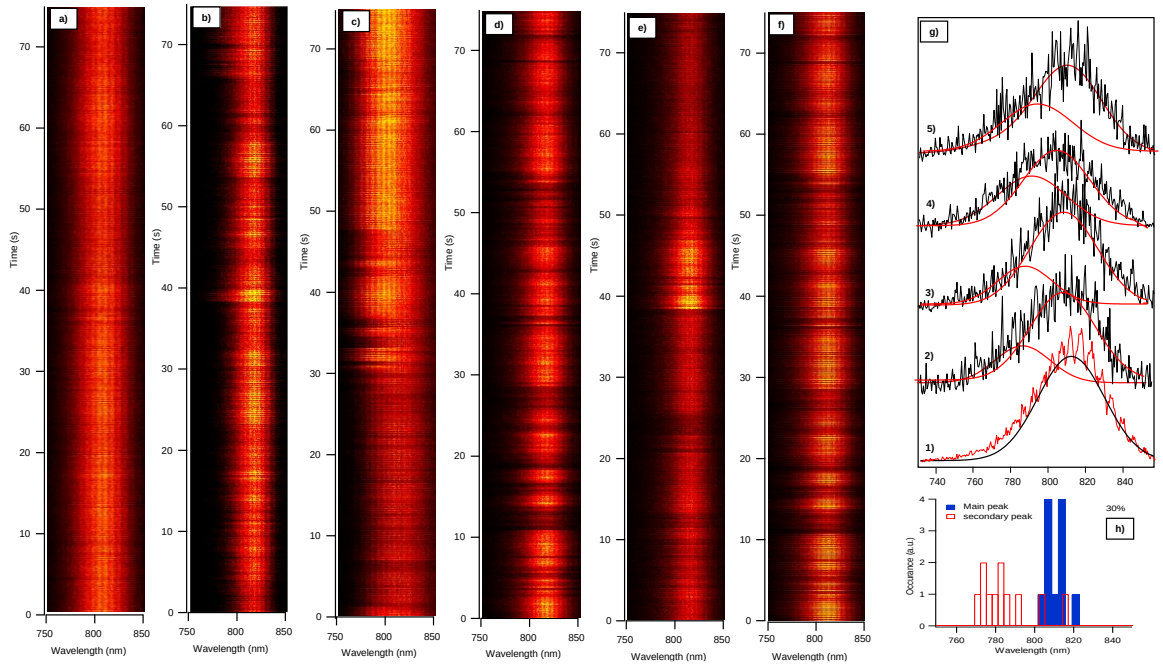

Figure 5.9. Time evolution PL Spectra of $MA_{0.7}FA_{0.3}PbI_3$ perovskite film. (a) PL spectra without external voltage. (b-f) PL spectra with applied 5V external voltage. (g) 2-4: PL spectra under applied field of 5V taken at different times from the trace (c); 1: PL spectrum without external filed taken from the trace (a). The solid lines are Gaussian fits to the spectra. (h) Histogram of PL spectral peaks analyzed from the traces (b) - (f).

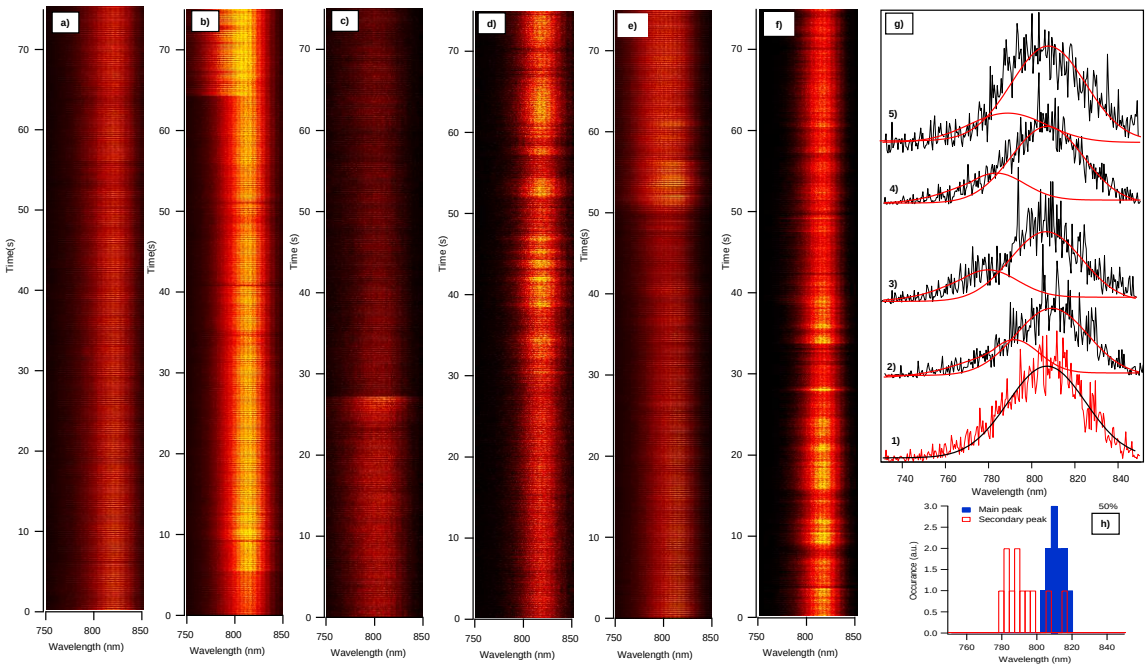

Figure 5.10. Time evolution PL Spectra of $MA_{0.5}FA_{0.5}PbI_3$ perovskite film. (a) PL spectra without external voltage. (b-f) PL spectra with applied 5V external voltage. (g) 2-4: PL spectra under applied field of 5V taken at different times from the trace (c); 1: PL spectrum without external filed taken from the trace (a). The solid lines are Gaussian fits to the spectra. (h) Histogram of PL spectral peaks analyzed from the traces (b) - (f).

5.3.4 Interpretation of the PL dynamics in terms of ion diffusion

Several studies indicated that organic MHPs are not only semiconductors but also ionic conductors, i.e. the applied bias can induce both charge carrier flow and ion flow.[38-39] The ion migration effect was found to be responsible for the solar cell current density-voltage (J-V) hysteresis. Taking into account the different types of defects in MHPs, possible mobile ions are I^-, MA^+, FA^+ and Pb^{+2}.[40-51] Theoretical calculations and experimental measurements have been carried out to access the activation energy for the ion migration process. Some of the typical values are summarized in the Table 5.1.

origin	Activation energy Ea (eV)	Ref
I^-	0.08 - 0.16	44
MA^+	0.46 - 0.84	49
FA^+	1.20	50
Pb^{+2}	0.58	48

Table 5.1. Activation energy of I^-, MA^+ and FA^+, Pb^{+2} ions in perovskite

Moreover, diffusion of FA^+ as compared to MA^+ is more complex because the higher tolerance factor as well and crystal structure cause overall higher stability for the FA^+ ions. Organic cations and the halides in the perovskite structure form hydrogen bonding between the acidic MA or FA hydrogen atoms and the perovskite iodides. Furthermore, regardless of the cation size, the tetragonal-to-quasi cubic structural evolution when moving from MA^+ to FA^+ is due to enhanced hydrogen bonding in FA^+ compared to MA^+.

Up to now, a consensus on the migrating ionic species and the concrete energy barriers is still missing. So far, most works suggest that iodine-related defects, i.e. I^- ion, are more active to migrate. The pathway of I^- vacancies (V_I) was suggested to occur along the I-I edge of the PbI_6 octahedron with an activation energy of 0.58 eV[45], while MA^+ vacancies migrate through the unit cell face comprised of four I- ions, yielding a higher activation energy of 0.84 eV[46] Delugas et al. modeled the ion migration through V_I and I^- ion

mechanisms. The results imply that at room temperature the V_I is more mobile than the I^- ion.[47] Experimental results from Cheng et al. demonstrate that under an electric field the I/Pb ratio is higher at the anode, which also supports the V_I/I^- ion-dominant migration. On the other hand, MA^+ ion accumulation under an electric field was detected with photothermal induced resonance[48] (PTIR)It is not contrary to the observation of I^- ion redistribution because an applied electric field is able to drive the two ions at the same time. Theoretical calculations showing the activation energy of MA^+ vacancy of 0.46 eV and that of V_I and I^- ion both of 0.08 eV implicate that the electric-field-driven migration of MA^+ vacancy should occur on the timescale from milliseconds to minutes, while that of iodine related defects on scales of less than 1 μs.[46]

Under photoexcitation only a minor part of the absorbed energy is emitted as PL because the PL quantum yield is quite low. Thus, most of the photo generated charges recombine nonradiative generating not only heat but also chemical/structural modifications of the material. Nonradiative recombination occurs via charge trapping by various defect states. Both light-induced PL enhancement and PL degradation have been discussed in relation to ion migration which can assist in annihilation and creation of defects.[44–46] When an MHP material is placed in an external electric field, both free charges and ions are able to drift along with the field direction.[33,43]

Taking into account the above-mentioned current state of understanding, we propose the flowing interpretation of the experimental observations. In our study we found that there are mainly two areas in the sample, structurally inhomogeneous pinhole area and a homogenous area of the film, and the effect of electric field is different in the two. The effect in the homogeneous area is summarized symbolically in the Figure 5.11. We assume that there are defects present in the film in the form of iodine vacancies V_I. In the mixed FA/MA samples there is a distribution of composition between individual domains (grains) in the film as found in Chapter 3, i.e., there are FA rich domains as well as FA poor domains (including pure MA domains) coexisting in the films. This composition is reflected in the PL spectra of the films. We further assume that because of their lower tolerance factor the defects are more likely present in the FA poor domains. This situation is schematically shown in the Figure 5.11a. Upon application of an external electric field (Figure 5.11c) both I- and MA+ migration can occur, but we assume that because of its lower activation energy the I- migration is dominant. For the forward bias shown in the Figure 5.11c the I- ions will

be moving towards and accumulating near the anode. The V_I vacancies present in this area (predominantly in the FA poor domains) will be filled and these domains will start emitting PL that is blue-shifted because of the lower content of FA ions. This is reflected in the appearance and dynamics of the new blue-shifted spectral bands observed in the Figures 5.8 – 5.10. In a similar way, the ion migration also affects the local PL intensity and causes the observed PL fluctuations. We note that because of the thickness (~ 450 nm) and high extinction coefficient of the perovskite films the PL microscopy can detect emission from only a thin layer of the sample just above the anode (PEDOT-PSS film), as shown in the Figure 5.11d.

Regarding the phenomenon of PL quenching in the inhomogeneous areas of the sample, we assume that the structural defects (pinholes) can work as traps for the migrating ions resulting in the quenching of the PL.

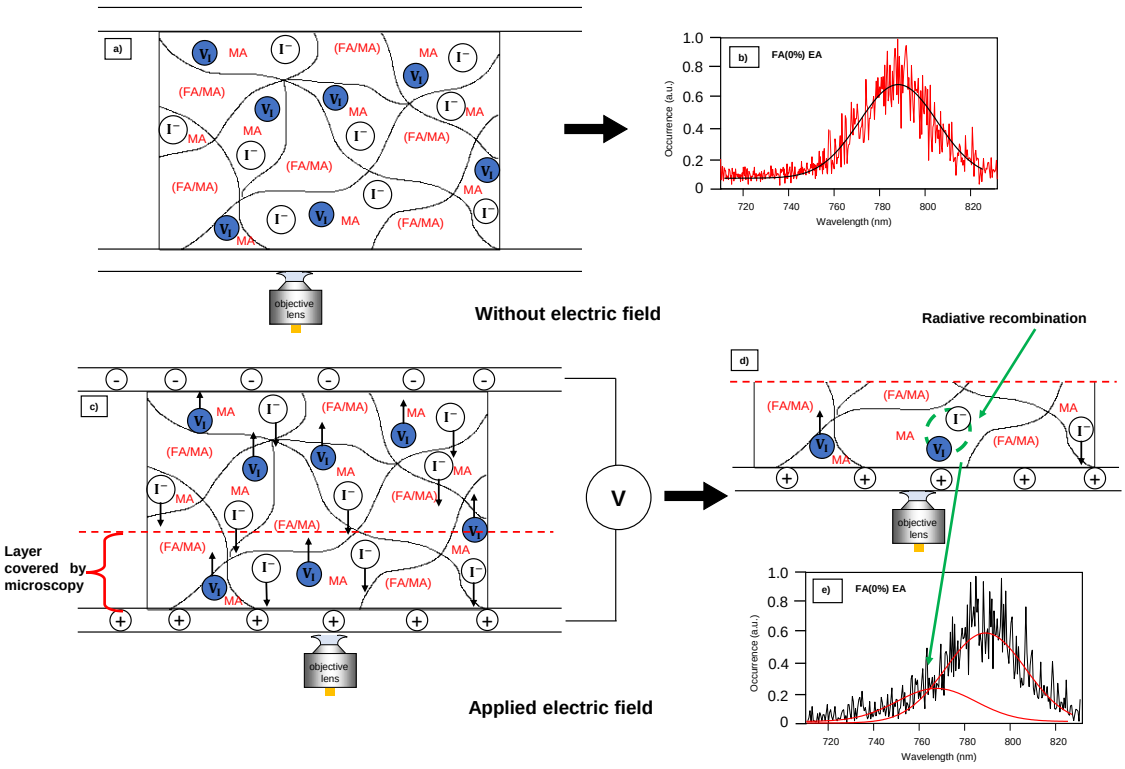

Figure 5.11. Schematic diagram of electric biasing effect on $MA_xFA_{1-x}PbI_3$ films

5.4 Conclusions

We applied an external electric field to the $MA_xFA_{1-x}PbI_3$ films in capacitance-like device to simulate the internal bias in working solar cells, and simultaneously monitored the PL dynamic behavior. Two different PL responses were observed in the same sample. Reversible PL quenching was observed under an electric field in locations characterized by changed morphology. PL intensity and spectral fluctuations due to externally applied field were found in homogeneous areas of the films. Both phenomena were attributed to migration of the iodine ions and vacancies due to the field. Filling of the vacancies in a layer of the film close to the microscope objective lens causes appearance of new blue-shifted PL band which causes the apparent spectral fluctuations. Such results can help us to gain a deep insight into how the ionic movements in the perovskite absorber layer influence the performance of the perovskite-based optoelectronic devices under working conditions.

5.5 References

1. Yu, J. C.; Kim, D. B.; Baek, G.; Lee, B. R.; Jung, E. D.; Lee, S.; Chu, J. H.; Lee, D.-K.; Choi, K. J.; Cho, S.; Song, M. H. High- Performance Planer Perovskite Optoelectronic Devices: A Morphological and Interfacial Control by Polar Solvent Treatment. *Adv. Mater*. 2015, 27, 3492−3500.
2. Tan, Z.-K.; Moghaddam, R. S.; Lai, M. L.; Docampo, P.; Higler, R.; Deschler, F.; Price, M.; Sadhanala, A.; Pazos, L. M.; Credgington, D.; Hanusch, F.; Bein, T.; Snaith, H. J.; Friend, R. H. Bright Light- Emitting Diodes Based on Organometal Halide Perovskite. *Nat. Nanotechnol*. 2014, 9, 687−692.
3. Li, G.; Tan, Z.-K.; Di, D.; Lai, M. L.; Jiang, L.; Lim, J. H-W.; Friend, R. H.; Greenham, N. C. Efficient Light-Emitting Diodes Based on Nanocrystalline Perovskite in a Dielectric Polymer Matrix. *Nano Lett.* 2015, 15, 2640−2644.
4. Liu, J.; Xue, Y.; Wang, Z.; Xu, Z.-Q.; Zheng, C.; Weber, B.; Song, J.; Wang, Y.; Lu, Y.; Zhang, Y.; Bao, Q. Two-Dimensional CH3NH3PbI3 Perovskite: Synthesis and Optoelectronic Application. *ACS Nano* 2016, 10, 3536−3542.
5. Lee, M. M.; Teuscher, J.; Miyasaka, T.; Murakami, T. N.; Snaith, H. J. Efficient Hybrid Solar Cells Based on Meso-Superstructure Organometal Halide Perovskites. *Science* 2012, 338, 643−647.
6. Kojima, A.; Teshima, K.; Shirai, Y.; Miyasaka, T. Organometal Halide Perovskites as Visible-Light Sensitizers for Photovoltaic Cells. *J. Am. Chem. Soc*. 2009, 131, 6050−6051.
7. Saliba, M.; Matsui, T.; Seo, J.-Y.; Domanski, K.; Correa-Baena, J.- P.; Nazeeruddin, M. K.; Zakeeruddin, S. M.; Tress, W.; Abate, A.; Hagfeldt, A.; Grätzel, M. Cesium-Containing Triple Cation Perovskite Solar Cells: Improved Stability, Reproducibility and High efficiency. *Energy Environ. Sci*. 2016, 9, 1989−1997.
8. Green, M. A.; Emery, K.; Hishikawa, Y.; Warta, W.; Dunlop, E. D. Solar Cell Efficiency Tables. Prog. *Photovoltaics* 2016, 24, 905−913.
9. Xing, G.; Mathews, N.; Sun, S.; Lim, S. S.; Lam, Y. M.; Grätzel, M.; Mhaisalkar, S.; Sum, T. C. Long-Range Balanced Electron and Hole Transport Lengths in Organic-Inorganic $CH_3NH_3PbI_3$. *Science* 2013, 342, 344−347.
10. Stranks, S. D.; Eperon, G. E.; Grancini, G.; Menelaou, C.; Alcocer, M. J. P.; Leijtens, T.; Herz, L. M.; Petrozza, A.; Snaith, H. J. Electron-Hole diffusion Lengths Exceeding

1 Micrometer in an Organometal Trihalide Perovskite Absorber. *Science* 2013, 342, 341− 344.

11. Li, F.; Ma, C.; Wang, H.; Hu, W.; Yu, W.; Sheikh, A. D.; Wu, T. Ambipolar Solution-Processed Hybrid Perovskite Phototransistors. *Nat. Commun*. 2015, 6, 8238.
12. Even, J.; Pedesseau, L.; Katan, C. Analysis of Multivalley and Multibandgap Absorption and Enhancement of Free Carries Relatedto Exciton Screening in Hybrid Perovskites. *J. Phys. Chem.* C 2014, 118, 11566−11572.
13. Wehrenfennig, C.; Eperon, G. E.; Johnston, M. B.; Snaith, H. J.; Herz, L. M. High Charge Carrier Mobilities and Lifetimes in Organolead Trihalide Perovskites. *Adv. Mater*. 2014, 26, 1584−1589.
14. Manser, J. S.; Kamat, P. V. Band Filling with Free Charge Carriers in Organometal Halid Perovskites. *Nat. Photonics* 2014, 8, 737−743.
15. Marchioro, A.; Teuscher, J.; Friedrich, D.; Kunst, M.; van de Krol, R.; Moehl, T.; Grätzel, M.; Moser, J.-E. Unravelling the Mechanism of Photoinduced Charge Transfer Processes in Lead Iodide Perovskite Solar Cells. *Nat. Photonics* 2014, 8, 250−255.
16. Hsu, H.-Y.; Wang, C.-Y.; Fathi, A.; Shiu, J.-W.; Chung, C. C.; Shen, P.-S.; Guo, T. F.; Chen, P.; Lee, Y.-P.; Diau, E. W.-G. Femtosecond Excitonic Relaxation Dynamics of Perovskite on Mesoporous Films of Al2O3 and NiO Nanoparticles. *Angew. Chem., Int. Ed.* 2014, 53, 9339−9342.
17. D'Innocenzo, V.; Grancini, G.; Alcocer, M. J. P.; Kandada, A. R. S.; Stranks, S. D.; Lee, M. M.; Lanzani, G.; Snaith, H. J.; Petrozza, A. Excitons versus Free Charges in Organo-Lead Tri-Halide Perovskites. *Nat. Commun*. 2014, 5, 3586.
18. Hutter, E. M.; Eperon, G. E.; Stranks, S. D.; Savenije, T. J. Charge Carrier in Planar and Meso-Structured Organic-Inorganic Perovskites: Mobilities, Lifetimes, and Concentrations of Trap States. *J. Phys. Chem. Lett*. 2015, 6, 3082−3090.
19. Ponseca, C. S., Jr.; Savenije, T. J.; Abdellah, M.; Zheng, K.; Yartsev, A.; Pascher, T.; Harlang, T.; Chabera, P.; Pullerits, T.; Stepanov, A.; Wolf, J.-P.; Sundström, V. Organometal Halide Perovskite Solar Cell Materials Rationalized: Ultrafast Charge Generation, High and Microsecond-Long Balanced Mobilities, and Slow Recombination. *J. Am. Chem. Soc*. 2014, 136, 5189−5192.
20. Menke, S. M.; Holmes, R. J. Exciton Diffusion in Organic Photovoltaic Cells. E*nergy Environ. Sci.* 2014, 7, 499−512.

21. Kirchartz, T.; Mattheis, J.; Rau, U. Detailed Balance Theory of Excitonic and Bulk Heterojunction Solar Cells. Phys. Rev. B: *Condens. Matter Mater. Phys*. 2008, 78, 235320.
22. Deschler, F.; Price, M.; Pathak, S.; Klintberg, L. E.; Jarausch, D.- D.; Higler, R.; Hüttner, S.; Leijtens, T.; Stranks, S. D.; Snaith, H. J.; Atatüre, M.; Phillips, R. T.; Friend, R. H. High Photoluminescence Efficiency and Optically Pumped Lasing in Solution-Processed Mixed Halide Perovskite Semiconductors. *J. Phys. Chem. Lett.* 2014, 5, 1421− 1426.
23. Yamada, Y.; Nakamura, T.; Endo, M.; Wakamiya, A.; Kanemitsu, Y. Photocarrier Recombination Dynamics in Perovskite CH3NH3PbI3 for Solar Cell Application. *J. Am. Chem. Soc.* 2014, 136, 11610−11613.
24. Narra, S.; Chung, C.-C.; Diau, E. W.-G.; Shigeto, S. Simultaneous Observation of an Intraband Transition and Distinct Transient Species in the Infrared Region for Perovskite Solar Cells. *J. Phys. Chem. Lett*. 2016, 7, 2450−2455.
25. Ohta, N. Electric Field Effects on Photochemical Dynamics in Solid Films. Bull. *Chem. Soc. Jpn.* 2002, 75, 1637−1655.
26. Hsu, H.-Y.; Chiang, H.-C.; Hu, J.-Y.; Awasthi, K.; Mai, C.-L.; Yeh, C.-Y.; Ohta, N.; Diau, E. W.-G. Field-Induced Fluorescence Quenching and Enhancement of Porphyrin Sensitizers on TiO2 Films and in PMMA Films. *J. Phys. Chem. C* 2013, 117, 24761−24766.
27. Ohta, N.; Awasthi, K.; Okoshi, K.; Manseki, K.; Miura, H.; Inoue, Y.; Nakamura, K.; Kono, H.; Diau, E. W.-G. Stark Spectroscopy of Absorption and Emission of Indoline Sensitizers: A Correlation with the Performance of Photovoltaic Cells. *J. Phys. Chem. C* 2016, 120, 26206−26216.
28. Leijtens, T.; Kandada, A. R. S.; Eperon, G. E.; Grancini, G.; D'Innocenzo, V.; Ball, J. M.; Stranks, S. D.; Snaith, H. J.; Petrozza, A. Modulating the Electron-Hole Interaction in a Hybrid Lead Halide Perovskite with an Electric Filed. *J. Am. Chem. Soc.* 2015, 137, 15451-15459.
29. Qiu, C.; Grey, J. K. Modulating Charge Recommbination and Structural Dynamics in Isolated Organometal Halide Perovskite Crystals by External Electric Fields. *J. Phys. Chem. Lett.* 2015, 6, 4560−4565.

30. Xiao, Z.; Yuan, Y.; Shao, Y.; Wang, Q.; Dong, Q.; Bi, C.; Sharma, P.; Gruverman, A.; Huang, J. Giant Switchable Photovoltaic Effects in Organometal Trihalide Perovskite Devices. *Nat. Mater*. 2014, 14, 193−198.
31. Umeuchi, S.; Nishimura, Y.; Yamazaki, I.; Murakami, H.; Yamashita, M.; Ohta, N. Electric Field Effects on Absorption and Fluorescence Spectra of Pyrene Doped in a PMMA Polymer Film. *Thin Solid Films* 1997, 311, 239−245.
32. Tsushima, M.; Ushizaka, T.; Ohta, N. Time-Resolved Measurement System of Electrofluorescence Spectra. *Rev. Sci. Instrum*. 2004, 75, 479−485.
33. De Quilettes, D. W.; Vorpahl, S. M.; Stranks, S. D.; Nagaoka, H.; Eperon, G. E.; Ziffer, M. E.; Snaith, H. J.; Ginger, D. S. Impact of Microstructure on Local Carrier Lifetime in Perovskite Solar Cells. *Science* 2015, 348, 683−686.
34. Li, Y.; Yan, W.; Li, Y.; Wang, S.; Wang, W.; Bian, Z.; Xiao, L.; Gong, Q. Direct Observation of Long Electron-Hole Diffusion Distance in $CH_3NH_3PbI_3$ Perovskite Thin Film. *Sci. Rep*. 2015, 5, 14485.
35. Wang, Q.; Shao, Y.; Xie, H.; Lyu, L.; Liu, X.; Gao, Y.; Huang, J. Quantifying Composition Dependent p and n Self-Doping in $CH_3NH_3PbI_3$. *Appl. Phys. Lett*. 2014, 105, 163508.
36. Alemu, G.; Li, J.; Cui, J.; Xu, X.; Zhang, B.; Cao, K.; Shen, Y.; Cheng, Y.; Wang, M. Investigation on Regeneration Kinetics at Perovskite/oxide Interface with Scanning Electrochemical Microscopy. *J. Mater. Chem. A* 2015, 3, 9216−9222.
37. Agarwal, A.; Omagari, S.; Vacha, M. Nanoscale Structural Heterogeneity and Efficient Intergrain Charge Diffusion in a Series of Mixed MA/FA Halide Perovskite Films. *ACS Energy Lett.* 2022, 7, 2443−2449.
38. Soe, C. M. M.; Nagabhushana, G. P.; Shivaramaiah, R.; Tsai, H.; Nie, W.; Blancon, J. C.; Melkonyan, F.; Cao, D. H.; Traore, B.; Pedesseau, L.; Kepenekian, M.; Katan, C.; Even, J.; Marks, T. J.; Navrotsky, A.; Mohite, A. D.; Stoumpos, C. C.; Kanatzidis, M. G. Structural and Thermodynamic Limits of Layer Thickness in 2D Halide Perovskites. *Proc. Natl. Acad*. Sci. U. S. A. 2019, 116, 58−66.
39. Wu, C.; Li, F.; Guo, T. Efficient Tristable Resistive Memory Based on Single Layer Graphene/Insulating Polymer Multi-Stacking Layer. *Appl. Phys. Lett*. 2014, 104, 183105.

40. Wetzelaer, G.-J. A. H.; Scheepers, M.; Sempere, A. M.; Momblona, C.; Avila, J.; Bolink, H. J. Trap-Assisted Non- Recombination in Organic-Inorganic Perovskite Solar Cells. *Adv. Mater*. 2015, 27, 1837−1841
41. Deretzis, I.; Alberti, A.; Pellegrino, G.; Smecca, E.; Giannazzo, F.; Sakai, N.; Miyasaka, T.; La Magna, A. Atomistic Origins of CH3NH3PbI3 Degradation to PbI2 in Vacuum. *Appl. Phys. Lett*. 2015, 106, 131904.
42. Leguy, A. M. A.; Frost, J. M.; McMahon, A. P.; Sakai, V. G.; Kockelmann, W.; Law, C.; Li, X.; Foglia, F.; Walsh, A.; O'Regan, B. C.; Nelson, J.; Cabral, J. T.; Barnes, P. R. F. The Dynamics of Methylammonium Ions in Hybrid Organic-Inorganic Perovskite Solar Cell. *Nat. Commun.* 2015, 6, 7124.
43. Leijtens, T.; Hoke, E. T.; Grancini, G.; Slotcavage, D. J.; Eperon, G. E.; Ball, J. M.; De Bastiani, M.; Bowring, A. R.; Martino, N.; Wojciechowski, K.; McGehee, M. D.; Snaith, H. J.; Petrozza, A. Mapping Electric Field-Induced Switchable Poling and Structural Degradation in Hybrid Lead Halide Perovskite Thin Films. *Adv. Energy Mater.* 2015, 5, 1500962.
44. Bae, S.; Kim, S.; Lee, S.-W.; Cho, K. J.; Park, S.; Lee, S.; Kang, Y.; Lee, H.-S.; Kim, D. Electric-Field-Induced Degradation of Methylammonium Lead Iodide Perovskite Solar Cells. *J. Phys. Chem. Lett.* 2016, 7, 3091−3096.
45. Eames, C.; Frost, J. M.; Barnes, P. R. F.; O'Regan, B. C.; Walsh, A.; Islam, M. S. Ionic Transport in Hybrid Lead Iodide Perovskite Solar Cells. *Nat. Commun*. 2015, 6, 7497.
46. Delugas, P.; Caddeo, C.; Filippetti, A.; Mattoni, A. Thermally Activated Point Defect Diffusion in Methylammonium Lead Trihalide: Anisotropic and Ultrahigh Mobility of Iodine. *J. Phys. Chem. Lett.* 2016, 7 (13), 2356–2361.
47. Azpiroz, J. M.; Mosconi, E.; Bisquert, J.; De Angelis, F. Defect Migration in Methylammonium Lead Iodide and its Role in Perovskite Solar Cell Operation. *Energy Environ. Sci.* 2015, 8, 2118−2127
48. Yuan, H.; Debroye, E.; Janssen, K.; Naiki, H.; Steuwe, C.; Lu, G.; Moris, M.; Orgiu, E.; Uji-i, H.; de Schryver, F.; et al. Degradation of methylammonium lead iodide perovskite structures through light and electron beam driven ion migration. *J. Phys. Chem. Lett.* 2016, 7, 561–566.
49. Zhong, Y.; Luna, C. A. M.; Hildner, R.; Li, C.; Huettner, S. In Situ Investigation of Light Soaking in Organolead Halide Perovskite Films. *APL Mater*. 2019, 7, No. 041114.

50. A. Urbaniak, A. Czudek, J. Dagar, and E. L. Unger, Capacitance spectroscopy of thin-film formamidinium lead iodide based perovskite solar cells, *Solar Energy Mater. and Solar Cells* 238 (2022) 111618.

Chapter 6

Conclusion and outlook

6.1 Summary and general conclusion

The purpose of this thesis is to provide new insights into the mixed cation (MA/FA) based perovskite thin films using fluorescence microscopy which can help to understand the fundamental properties of this material. Such advances in thin-film semiconductor understanding will also find applications in the development of highly efficient and low-cost photovoltaics. Hybrid halide perovskites have emerged over the unprecedented timeframe over the last few decades as a promising class of materials for such applications. Most notably, their solar cells have achieved power conversion efficiencies above 25 % in the laboratory, even though many fundamental questions on their basic material properties still remain unanswered. Therefore, for halide perovskite thin-films to have an impact beyond the laboratory requires a systematic understanding for further improvement. In this thesis we have studied these materials and revealed answers to some of the important questions, such as structural and compositional heterogeneity, long-term environmental stability and degradation, and stability under external electrical bias.

In Chapter 1 we outline the background and literature of perovskite materials research including their basic semiconductor properties which indicate why this material needs attention, as well as introduction to the perovskite photophysical processes. In addition, by introducing the fluorescence microscopy we have also summarized key previous studies. It was emphasized that fluorescence microscopy is an essential technique to study not only nanoparticles but also bulk samples as it can reveal the nanoscale physical properties of the material.

In Chapter 2, we systematically optimized the $MA_xFA_{1-x}PbI_3$ perovskite thin film preparation methodology used in this thesis to improve the film quality, while pointing the way forward to eliminate the pinholes and ultimately design even better morphology samples. Firstly, we have introduced how processing, composition and surface passivation affect the results of fabrication. Technically, the optimization cycle involves controlled fabrication techniques involving careful changes based on a feedback from all the parameters of the halide perovskite thin films. By considering the parameters related to spin coating, precursor solutions, annealing temperature, appropriate choice of antisolvent and dropping technique of antisolvent, etc., we succeeded in optimizing the samples for the fluorescence microscopy study, and assume that the results will provide potentially useful feedback for solar cell performance.

Next in Chapter 3 we have used several characterization techniques including UV-absorption spectroscopy, SEM and fluorescence microscopy to systematically study the $MA_xFA_{1-x}PbI_3$ mixed cation-based perovskite thin films. We have used wide field microscopy to measure the photoluminescence properties in terms of PL blinking which reflects dynamic quenching due to the non-radiative recombination and PL spectra which show the compositional heterogeneity in the sample. We found out that the $MA_{0.5}FA_{0.5}PbI_3$ has the least dynamic quenching because it contains the lowest fraction of pure FA and pure MA domains, as reflected in the largest PL spectral distribution. Lastly, we have seen that the blinking is correlated between locations that are micrometers apart which indicates that the grain boundaries do not function as traps and are transparent toward efficient charge migration.

Perovskite thin films are potentially the ideal solar cell materials which might contribute to solving a major energy crisis in the world. But for perovskite thin films, a major challenge is their degradation process. In Chapter 4, we correlate the information from chapters 2 and 3 to understand the perovskite film degradation process on microscopic level, and study the effect of antisolvent on the long-term air stability of mixed cation halide perovskite thin films over one year. To explain the surprisingly long-term stability have used fluorescence microscopy on mixed cation perovskites films of the composition $MA_xFA_{1-x}PbI_3$, with x = 0, 0.3 and 0.5. We have seen that the perovskite films with x = 0.5 and 0.3 prepared in the air using ethyl acetate as an antisolvent in a one-step spin-coating process are compositionally stable in ambient air for more than a year as compared to the films prepared using the antisolvent of chlorobenzene. We have studied the degradation process of the films and proposed slow MA cation migration and local formation of 2D perovskite phases to explain the results.

Finally, as a last part of this thesis in Chapter 5 we attempted to elucidate the stability of the perovskite films in working perovskite-based photovoltaic devices by using externally applied voltage in the microscopic PL studies. PL of a crystalline film of the mixed cation lead iodide perovskite ($MA_xFA_{1-x}PbI_3$) sandwiched between an ITO electrode and an insulating film of poly(methyl methacrylate) (PMMA) is found quenched and flickering significantly with the application of an external electric field. Measurements of electro-photoluminescence spectra revealed that the I^- ion and V_I vacancy migrates and recombine, with a result of a blue shift in the PL spectra.

6.2 Outlook

The fundamental finding of this thesis will pave the way for controlling the morphology of perovskite absorber layer in the fabrication process, and will provide microscopic insights to eliminate the drawbacks of hybrid perovskite thin films. We hope that our work will help enhance the viability of perovskite photovoltaics for successful commercialization in the near future.

List of Publications

Related to the Thesis

1. Nanoscale structural heterogeneity and Efficient intergain charge diffusion in a Series of mixed MA/FA halide perovskite films.
   Agarwal, A.; Omagari, S.; Vacha, M., ACS Energy Lett. **2022**, 7, 2443−2449.

2. Air-stable mixed cation lead halide perovskite films and microscopic study of their degradation process.
   Agarwal A.; Omagari S.; Vacha M., Nanoscale 2023. (Under major revision)

3. Photoluminescence Dynamics unraveling the ion migration in mixed (MA/FA) halide perovskite films under the applied electrical field.
   Agarwal A.; Omagari S.; Vacha M., (in preparation)

Other Publications

1. Enhanced Photovoltaic Efficiency via Control of Self-Assembly in Cyanopyridone-Based Oligothiophene Donors.
   Agarwal[*1]A.; Kaur*1 H. A.; Ali*1 S; et al. ACS publication J. Phys. Chem. Lett., **2021**, 12, 2, 919–924.

2. Impact of self-assembly on the photovoltaic properties of a small molecule oligothiophene donor.
   Kaur[*1] H.A.; **Agarwal[*1] A.;** et al., Solar Energy, Elsevier, **2019**, 195 (2020) 223-229.

3. Improvement of the optoelectronic and photovoltaic properties of a cyanopyrid-2,6 dione-based donor via molecular engineering. **Agarwal[*1]A.**; Kaur[*1] H.A.; et al., Dyes and Pigments, Elsevier, **2019**,170-107661.

4. Direct connection of an amine to oligothiophene to generate push-pull chromophores for organic photovoltaic applications. **Agarwal A.;** et al., Dyes and Pigments, Elsevier, **2019**, 162, 315-323.

5. Generating an efficient, 3D non-fullerene electron acceptor by combining cheaply synthesized spiro[fluorene-9,9'-xanthene] and cyanopyridone,
   Kadam G.; Pree A.; **Agarwal A.;** et al., Materials Chemistry Frontier, **2018**, 2, 1090-1096.

6. Naphthalene diimide-based non-fullerene acceptors flanked by open-ended and aromatizable acceptor functionalities.
   Srivani D.; **Agarwal A.;** et al., Chem. Commun., **2017**, 53, 11157–11160.

7. ZnS nanostructured thin films deposited by successive ionic layer adsorption and reaction.
   Deshmukh G. S.; Jariwala A.; **Agarwal A.;** et al., AIP Conf. Proc., **2016**, 1724, 020033.

Public appearances

1. Microscopic study of mixed cation (MA/FA) lead halide perovskites. (Oral presentation)

   Agarwal A., Annual meeting on Photochemistry **2022**, The Japanese Photochemistry Association, Kyoto (Japan)

2. Microscopic study of mixed cation lead halide perovskites. (Poster presentation)

   Agarwal A., 28th IUPAC Symposium on Photochemistry, July 2022, Amsterdam (Netherland)

3. Study of Perovskite thin films on Fluorescence microscopy. (Oral presentation)

   Agarwal A., International Conference on Emerging Photovoltaic Materials and Technologies (ICEPV-2022), April 2022, Turkey (Online)

4. Optimization and fluorescence characterization of perovskite thin films (poster presentation)

   Agarwal A., Annual Meeting on Photochemistry 2021 organized by The Japanese Photochemistry Association, September 2021 (Online)

Acknowledgments

This thesis becomes a reality with the kind support and encouragement from numerous people. Now, it is my pleasure to express my gratitude to those people for their assistance, support, and inspiration.

First of all, I would like to express my sincere gratitude to my supervisor, Professor **Martin Vacha** in Tokyo Institute of Technology for all. I owe my sincerest gratitude to him for giving me the opportunity to work under his guidance. His fruitful discussion, kind support, constant encouragement, and useful suggestions made the completion of my Ph.D. possible. His vast knowledge and immense passion for science have greatly inspired me and shaped my perception of scientific research. I am thankful for giving me complete freedom in my research work and providing the essential arrangements, laboratory facilities, and moral support throughout my Ph.D. work to achieve the goal. I also would like to truly thank Assistant professor **Shun Omagari** for the discussion and good suggestions.

I would like to express my appreciation to my friends and lab members **Nakamura Ryotaro, Qiwen Tan, Xiayan Wu, Wenhao Zhang, Tomoyuki Kobori, Tetsuhiro Maruyamano, Ryota Kambe, Toranosuke Takagi, Yanfei wang, Saki hishiyama, Takuma Matsumoto** for spending good time. I also appreciate Tokyo Institute of Technology for the financially supported by the Tokyo-Tech pioneering doctoral research program 'Cross the border!' scholarship.

Finally, My deepest thanks to all my family I should not forget to mention a few of them. I am very thankful to my mother **Suman Agarwal** for her love, blessing, and constant encouragement to pursue higher study. I am fortunate to have **Aman Goyal** in my life for support and love through the ups and downs during my Ph.D. journey. I would also like to acknowledge my younger brother **Divy Gupta** who always helps me to understand chemistry and theoretical concepts.

Finally, I wish to express my deep sense of gratitude to my Father for his unconditional love and blessing. He was instrumental in building my character, morality, and personality. I am dedicating this thesis to my father **Late Ravi Gupta.**